Autonomous Agent-Based Systems and their Applications in Fluid Dynamics, Particle Separation, and Co-evolving Networks

自主個體為本系統與在流體力學、分子分離、共同演化網絡上的應用

GRAESER, Oliver

顧皓森

A Thesis Submitted in Partial Fulfillment
of the Requirements for the Degree of
Doctor of Philosophy
in
Physics

The Chinese University of Hong Kong
August 2010

Thesis Assessment Committee

Professor CHU Ming Chung	(Chair)
Professor HUI, Pak Ming	(Thesis Supervisor)
Professor ONG, Hock Chun Daniel	(Committee Member)
Professor JOHNSON, Neil F	(External Examiner)

Abstract of thesis entitled

Autonomous Agent-Based Systems and Their Applications in Fluid Dynamics, Particle Separation, and Co-evolving Networks

Submitted by Oliver Graser

for the degree of Doctor of Philosophy

at The Chinese University of Hong Kong in July 2010

This thesis comprises three parts, reporting research results in Fluid Dynamics (Part I), Particle Separation (Part II) and Co-evolving Networks (Part III)

Part I deals with the simulation of fluid dynamics using the lattice-Boltzmann method Microfluidic devices often feature two-dimensional, repetitive arrays Flows through such devices are pressure-driven and confined by solid walls We have defined new adaptive generalised periodic boundary conditions to represent the effects of outer solid walls, and are thus able to exploit the periodicity of the array by simulating the flow through one unit cell in lieu of the entire device The so-calculated fully developed flow describes the flow through the entire array accurately, but with computational requirements that are reduced according to the dimensions of the array

Part II discusses the problem of separating macromolecules like proteins or DNA coils The reliable separation of such molecules is a crucial task in molecular biology The use of Brownian ratchets as mechanisms for the separation of such particles has been proposed and discussed during the last decade Pressure-driven flows have so far been dismissed as possible driving forces for Brownian ratchets, as they do not generate ratchet asymmetry We propose a microfluidic design that uses pressure-driven flows to create asymmetry and

hence allows particle separation The dependence of the asymmetry on various factors of the microfluidic geometry is discussed We further exemplify the feasibility of our approach using Brownian dynamics simulations of particles of different sizes in such a device The results show that ratchet-based particle separation using flows as the driving force is possible Simulation results and ratchet theory predictions are in excellent agreement

Part III deals with the co-evolution of networks and dynamic models A group of agents occupies the nodes of a network, which defines the relationship between these agents The evolution of the agents is defined by the rules of the dynamic model and depends on the relationship between agents i e , the state of the network In return the evolution of the network depends on the state of the dynamic model The concept is introduced through the adaptive SIS model We show that the previously used criterion determining the critical infected fraction, i c , the number of infected agents required to sustain the epidemic is inappropriate for this model We introduce a different criterion and show that the critical infected fraction so determined is in good agreement with results obtained by numerical simulations

We further discuss the concept of co-evolving dynamics using the Snowdrift Game as a model paradigm Co-evolution occurs through agents cutting dissatisfied links and rewiring to other agents at random The effect of co-evolution on the emergence of cooperation is discussed using a mean-field theory and numerical simulations A transition between a connected and a disconnected, highly cooperative state of the system is observed, and explained using the mean-field model Quantitative deviations regarding the level of cooperation in the disconnected regime can be fully resolved through an improved mean-field theory that includes the effect of random fluctuations into its model

摘要

本論文分成三個部份，分別包括流體動力學（第一部分）分子分離（第二部份）及共同演化網絡 (第三部份）的研究結果。論文的第一部份研究利用晶格波茲曼法模擬流體動力學的若干問題，探討在重複分佈的結構中在壓力推動下，對邊界條件作出適當定義的問題。在水壓梯度驅動下，新定義的適應性週期邊界條件代表系統的牆壁對流動的影響。因此，我們可以簡化針對整個系統的計算步驟，集中處理箇元胞的計算，從而得出能準確描述整個系統流動的計算結果。

論文的第二部份討論分離高分子如蛋白質或 DNA 螺旋的問題。可靠的分離方法對分子生物學的工作十分重要。利用布朗齒輪作為分離這些分子的方法已被提出及討論多年。在布朗齒輪中，壓力梯度因會形成對稱性，而未被視作系統可能的驅動力. 我們提出種微流體的設計之果，利用壓力差形成不對稱性，從而達到分子分離的效果. 我們還會討論不同的因素對於其不對稱性的影響. 我們利用布朗動力學模擬了，分離不同大小的分子的可行性，得出的結果與我們利用齒輪定理所預測的相符。

論文的第三部份研究網絡和動力學模型的共同演化。有一些個體佔據了網點，而網點間的關係定義了個體間的關係。這些個體的演化是根據動力學模型的規則。而這種演化是受到個體間的關係或網絡影響。而網絡的演化亦取決於動力學模型的狀態。我們利用適應 SIS 模型帶出相關概念。我們指出以往對臨界感染比例。即要維持傳染性所需的初始受感染個體比例的判斷準則並不恰當。我們提出了一個新的判斷準則，得出的臨界感染比例的數值跟電算模擬的結果相當吻合。

我們引申到利用雪堆博弈來討論共同演化的概念。共同演化是在一些個體切斷不滿意的聯繫再隨機接駁其他個體的時候發生的。我們會以平均場理論和電算模擬去討論共同演化對產生合作性的影響。利用平均場理論可解釋連接相和不連接相之間的變化。進一步包含了隨機漲落影響的平均場理論，能夠完全解決在不連接相中系統的合作程度和簡單平均場理論的偏差。

Acknowledgements

This thesis could not have been written without the help of many people, for whose help I am very grateful. First and foremost, I would like to thank my parents, who supported the idea of going overseas for PhD studies right from the start, and my supervisor, Prof. HUI Pak-Ming, who was willing to accept me as his graduate student. His advice on how to approach research problems, his guidance on how to turn an understanding of a problem into meaningful results, and his patience were all invaluable to me.

I also would like to thank Prof. XU Chen for his initial suggestion and following discussions of the Dissatisfied-Adaptive Snowdrift Game. The theoretical results of this model were my first actual research results and gave me great motivation for the further course of my studies.

At CUHK's physics department, I'm very grateful to the staff of the General Office, in particular Mrs. WONG Yeuk Lan, who went great lengths to help me whenever I had troubles figuring out the precise procedures and regulations required by the bureaucracy of CUHK's graduate school.

Parts I and II are a result of a cooperation with Andrej Grimm of the National University of Singapore. He suggested the original problem as well as the cooperation, which proved to be interesting, fruitful, and fun. Our discussions over a beer, whether dealing with physics or not, greatly helped me to cope with the rabbit hole[1], that is graduate school.

Going overseas always poses challenges, and I am very happy that I quickly found friends who were willing to share their time with me, and who helped me

[1] A Google search reveals that while graduate schools prefer to describe themselves as *the adventure that is graduate school*, graduate students seem to prefer the terms *research nirvana*, *vast dark tunnel*, *multitasking frenzy*, *whirlwind*, *bureaucratic maze* and – fancy that – *gravity well*.

whenever help was needed. In particular, I would like to thank Yin Haiping, Chan Chun-Him, Chan Wenling, Zhang Yaojun and other students from Room 224, who made working there a very nice experience, and Cathy Tsui, Alfred Wong, Ruby Chan and Thomas Chan for innumerable enjoyable hours.

我嚟香港嗰陣時, 想學屬於呢一個地方嘅語言 - 廣東話。雖然呢種機會對一個研究生嚟講唔係好常有, 但後來中文大學雅禮中國語文研習所俾我參加佢地嘅課程。我希望能夠喺呢度多謝我嘅老師：李兆麟，張冠雄，同埋陳泳因，因為即使我喺學廣東話時經常遇到問題, 佢哋都樂意額外抽出時間幫助我。

而且, 好多朋友都不時會同我練習. 幫手改善我嘅廣東話。我亦希望喺呢度多謝我嘅朋友：唐慧珊，鄭壁妮，劉詠詩，徐秀媚，同埋陳穎芝多謝佢哋唔太過份地取笑我唔正確嘅讀音同埋文法嘅錯誤, 並且多謝佢哋改善我嘅廣東話時帶俾我愉快嘅時光。

The work in Part III of this thesis was supported in part by the Research Grants Council (RGC) of the Hong Kong SAR Government through Grant No. CUHK-401109. I am furthermore grateful for the support of the Department of Physics for research trips to the National University in Singapore, where large parts of the works described in Parts I and II were done.

Contents

List of Figures

Chapter 0

Introduction

Complex phenomena that arise out of very simple scenarios have been a subject of physics research for a long time. A good example is the study of the physics of glasses. Consider a dispersion of hard spheres that interact through elastic collisions. A fluid system can suddenly freeze if its density is only marginally increased [1]. Similarly surprising effects can also occur in a dispersion of hard ellipsoids. Such a dispersion might have a very low shear viscosity if gently stirred, but can nearly solidify almost instantly if a strong shear force is applied [2]. Without going into the details of the statistical physics of glassy systems, we can take the simplest units in these systems as a paradigm of autonomous agent-based systems. Each hard sphere can be seen as an autonomous agent, whose movement depends only on its current state and its local surroundings. If a sphere collides with another, momentum is exchanged according to the laws of elastic collisions. If not, the sphere moves according to its current velocity.

This thesis consists of three parts. For each of the problems studied, it is possible to define a basic unit that acts according to a predefined rule set.

These units are autonomous, i e , they may interact with other units but do not need any instructions from the outside The question of how complex results emerge from the collective interaction of such simple units forms the overall theme of this thesis

Part I deals with the simulation of fluid dynamics using the lattice-Boltzmann method At every lattice node the state of the fluid is described by a small set of populations that have certain predefined velocities Nonetheless the fluid flow described by the collective interaction of these nodes fulfils the Navier-Stokes equation In Part I we discuss issues related to boundary conditions in the simulation of fluid dynamics in repetitive geometries Exploiting periodicity in a system allows us to solve problems that would otherwise vastly exceed our capabilities, e g , the Bloch's theorem in energy band theory in solid state physics allows us to focus on solving the Schrodinger equation in one unit cell instead of dealing with the $> 10^{22}$ atoms that are typically found in a small piece of condensed matter Micro-fabricated sieve devices used in molecular biology research pose a similar problem These devices typically consist of a repetitive array of obstacles The flow through these devices cannot be calculated with meaningful precision if the entire array is simulated Simply using periodic boundary conditions is however not possible In particular, the effects of an external pressure gradient driving the flow and of the solid walls confining the flow would be ignored in this way Hence a boundary condition scheme that exploits periodicity but at the same time incorporates such external forces is needed Such a boundary condition scheme applicable to the simulations of microfluidic devices is proposed in Part I

In Ch 1 an introduction to the problem is given so as to motivate the subsequent work Chapter 2 introduces the lattice-Boltzmann method as such, and provides some background knowledge about fluid dynamics, together with

a discussion on the problem of boundary conditions in the lattice-Boltzmann method. Some recently proposed periodic boundary conditions for pressure-driven flows through repetitive geometries are used to illustrate the problem at hand. In Chapter 3, we introduce a novel class of boundary conditions that provides for the effects of the outer confining walls, and therefore facilitates efficient simulations of the flow through repetitive microfluidic geometries. The methodology is discussed in detail The validity is tested by comparing simulation results of our method with results from simulations of a full array. It is found that the deviations in the resulting fully developed flows are marginal (10^{-8}). while the computation time is much reduced. The results were published in Physical Review E [3].

In Part II, we propose a novel microfluidic design for a pressure driven Brownian ratchet that can be used for particle separation, based on the results in Part I. The task of separating macromolecules, e.g., proteins, polymers or DNA strains, is crucial in the field of molecular biology and yet often highly non-trivial. This is particularly the case for coils of DNA fragments that need to be separated for genome sequencing. However, they elude separation because their net charge and fluid mobility depend on their size in the same manner. Thus. the separation of DNA fragments is still a cumbersome task that involves many manual steps and cannot be automated in a straightforward manner. Brownian ratchets could offer a remedy to this problem as they are able to separate particles according to their diffusion constant. They can be micro-fabricated as an array of identical, simple obstacles on a silicon wafer, and the separated strains can be retrieved at different exit channels of the device.

A recurrent problem in the design of such ratchet-based particle separators

is the choice of the driving force that keeps the ratchet out of thermal equilibrium and thus allows the rectification of Brownian motion. Electrostatic fields, inertial and gravitational forces all proved to have different downsides for realising the separation effect. Pressure-driven flows were previously not considered to be a possible alternative, as a force orthogonal to the ratchet structure could not be induced. In Part II, we introduce a novel design that circumvents this problem, and thus facilitates pressure-driven particle separation in Brownian ratchets. The discussion is split into two chapters. Chapter 4 discusses the underlying mechanism of Brownian ratchets, existing proposed devices and issues that arose in their realisations. Chapter 5 discusses our proposed microscopic structure. The principal advantages of our design and the theoretical abilities to resolve particles of different sizes are discussed in detail. Results of Brownian dynamics simulations, based on flow fields obtained by the methods developed in Part I, are used to test the functionality of the design. The prospects of our proposed design are also discussed. Results in this chapter have been submitted for publication [4]. Experimental realisation of our design is now underway at the National University of Singapore.

Part III discusses the co-evolving processes in complex networks. The structure of complex networks has been a focal point of research in science, and in physics in particular, during the last two decades [5, 6]. Properties such as the degree distributions, clustering coefficients and degree correlations have all been investigated in detail. More recently, networks have been used as an underlying connection matrix for social and biological dynamic models. These networks were typically taken to be static, or they evolved independently. In contrast, human relationships, which these networks are supposed to represent, typically evolve in response to the dynamic model. For example, opinions are spread via connections between people, but people may intend to be connected

to others who share their views The co-evolution of a dynamic model system, represented through autonomous agents, and the underlying network is the focus of Part III, which comprises Chs 6 to 9 of the thesis

Chapter 6 gives an introduction to the essential concepts of complex networks and dynamic models that are used extensively thereafter Chapter 7 introduces the concept of co-evolving or adaptive networks, using the adaptive susceptible-infective-susceptible (SIS) model that originally popularised this topic as the context [7] The adaptive SIS model describes the spread of a non-lethal disease against which no immunity is acquired through a population As a reaction to the infection, healthy individuals try to distance themselves from those infected in order to fend off the disease We review the model, and discuss how it can be described within a mean-field theory (MFT), and how a MFT can be used to provide fundamental insight into the possible states attainable by a system We further discuss the critical initial infected fraction, i e , the initial level of infected individuals in a population required to sustain a disease We show that the critical fraction is dependent on the spatial configuration of the network, and that the fixed point of the MFT, which was used to determine the critical fraction, in general does *not* give a good estimate of the critical fraction We propose a better way to identify the critical fraction and validate it by numerical simulations of the system Our approach is also applicable to other co-evolving systems that are describable by a set of dynamical equations for which the fixed point may also refer to a highly unlikely network configuration The results have been submitted for publication [8]

Chapters 8 and 9 consider the emergence of cooperation in co-evolving networks When humans or agents have to make choices about how to act in a certain situation, they are often faced with what is called a social dilemma

A choice made out of pure self-interest rarely coincides with the choice that is most beneficial for society as a whole. While personal relationships can explain cooperation on a local scale, the question why people act cooperatively on a larger scale towards others whom they do not know remains largely unresolved.

Chapter 8 introduces a co-evolving model of the Snowdrift Game on networks. In game theory, the Snowdrift Game can be seen as a social dilemma as it promises the highest possible payoff to a selfish uncooperative person but at the same time puts that person at risk to end up with the worst outcome. In our model individuals encounter Snowdrift Game situations in pairs. Dissatisfied individuals can react in two ways: by changing their strategy of being cooperative or uncooperative, or by rejecting their counterpart and choosing another individual to associate with. The model exhibits disconnected-connected transitions in the network structure and phase separations in the nodes' strategies driven by the co-evolving dynamics. Cooperative nodes may overcome uncooperative nodes, expel them, and form a closely connected, fixed network consisting exclusively of individuals who are willing to cooperate. If they do not manage to overcome the uncooperative individuals, a permanently evolving network results, with significantly fewer cooperative individuals than in the disconnected state. The emergence of either state depends both on the temptation involved in the Snowdrift Game and the number of initially cooperative individuals. The results are qualitatively explained using a simple mean-field theory. The results were published in EPL [9].

Chapter 9 examines the mathematical aspects of the model. In particular, we discuss how to include the effects of random fluctuations properly into mean-field theories. Each of the assumptions that are required to close a set of mean-field equations is carefully tested. We discuss why previously used

closure methods, such as those proposed for the adaptive SIS model discussed in Ch 7 [10], are unsuitable for the different co-evolving strategies of our model We introduce a new closure method that significantly improves upon the results in Ch 8 We use the method to perform a detailed analysis of our model and discover a surprising situation in which a gradually decreasing temptation to be selfish leads to a decreasing number of cooperators [11] The methods we used in developing a proper mean-field theory can be applied to a wide range of models

A summary of the main results and an outlook on future work and further applications will be found at the end of each part and, where applicable at the end of a chapter

Part I

Novel Boundary Conditions for the Lattice-Boltzmann Method

Chapter 1

Motivation

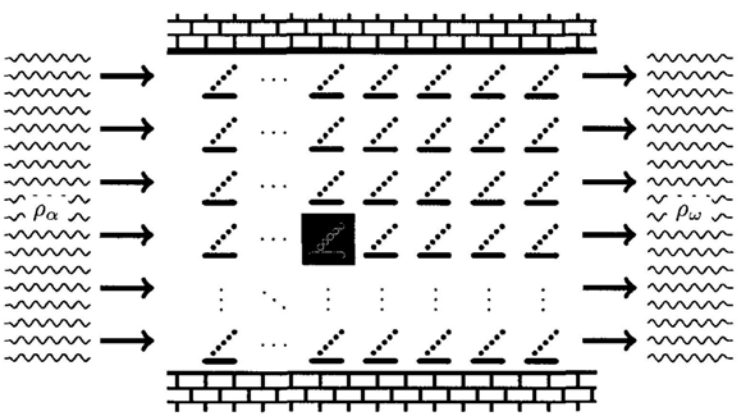

Figure 1.1: An exemplary microfluidic design, consisting of a repetitive array of identical obstacles confined by solid walls. Reservoirs of constant and different pressures ρ_α and ρ_ω result in a pressure driven flow through the array.

This part of the thesis was motivated by a simple which-tool-to-use problem. To understand the microfluidic geometry needed for efficient particle separation (see Part II), we wanted to calculate pressure driven flows through a vast array of obstacles. An example is shown in Fig 1.1. We chose the

lattice-Boltzmann method as a tool for solving the Navier-Stokes equations, since it can be easily adapted to different obstacle geometries. Physical boundary conditions are well defined over the entire system. Solid no-slip walls, i.e., zero-velocity boundary conditions, on the upper and lower boundaries, and constant pressure boundary conditions on the left and right. However, the vast dimensions of the entire system do not allow a direct simulation. A possible remedy is the simulation of one single unit cell of the array, here highlighted in green. Unfortunately, physical boundary conditions on one single unit cell are much more difficult to define, and implementations of such boundary conditions did not exist previously. We therefore extended a method proposed by Kim and Pitsch [12] to obtain boundary conditions that exploit the periodicity of the system, and at the same time incorporate the effects of the outer physical boundary conditions. The presented results have been published in Ref. [3].

The outline of this part is as follows. In Ch. 2, we will give an overview of the lattice-Boltzmann method, with emphasis on boundary condition implementations in general and the Kim/Pitsch (KP) boundary conditions in particular. In Sec. 3.1, we will state the problem definition and discuss our approach in detail. The results of our approach and a quantitative comparison with a reference system will be shown in Sec. 3.2.

Chapter 2

Introduction to the Lattice-Boltzmann Method

This chapter gives an overview on the basic features and concepts of the lattice-Boltzmann method. The goal of this overview is to offer the background information required to understand the results in the following chapters. Details in the derivation of the lattice-Boltzmann equation are omitted to allow for brevity (see Refs. [13, 14, 15, 16]). Further information on the background of the lattice-Boltzmann method can be found, among others, in Refs. [17, 18, 19, 20]. Concepts from fluid dynamics in general will only be discussed as long as they are directly relevant to the lattice-Boltzmann method.

2.1 A Primer on Fluid Dynamics

2.1.1 The Incompressible Navier-Stokes Equation and its Numerical Solutions

While real matter, as well as the idealised fluid in a lattice-Boltzmann simulation, is compressible, it can be advantageous to imagine an idealised, incompressible fluid of constant density

$$\rho(\mathbf{x}, t) = \rho_0 \tag{2 1}$$

The state of such a fluid within some domain is described by its fluid velocity $\mathbf{u}(\mathbf{x}, t)$ and pressure $p(\mathbf{x}, t)$ The motion of such a fluid follows the incompressible Navier-Stokes equation

$$\frac{\partial \mathbf{u}}{\partial t} + (\mathbf{u} \quad \nabla)\mathbf{u} = -\frac{p}{\rho_0} + \nu \nabla^2 \mathbf{u} \ , \tag{2 2}$$

and the incompressible continuity equation

$$\nabla \quad \mathbf{u} = 0 \tag{2 3}$$

The properties of the fluid enter the equation through its density ρ_0 and kinematic viscosity ν To constitute a fully specified physical problem, boundary and initial conditions have to be specified Common physical boundary conditions specify either a velocity or pressure profile on the boundary of the domain Solid walls confining the fluid are turned into velocity boundary conditions through the so-called *no slip condition*, which assumes that molecules in direct contact with the walls have zero velocity In addition pressure and velocity initial conditions have to be specified on the entire domain

2.1.2 Dimensionless Formulation and Dynamic Similarity

Obviously, two fluid dynamics problems for liquids of identical characteristics (i.e., viscosity and density) and identically defined boundary and initial conditions have identical solutions. In addition, even differently specified physical problems can have identical mathematical solutions – a phenomenon referred to as *dynamic similarity*. To understand this concept, one should keep in mind that a physical problem is always specified in dimensional units. The choice of units however is arbitrary, even if standards like the SI-system should be used for clarity. However, using different unit systems does not change the physics of the system.

Looking at a fluid dynamics problem, one can characterise it through length and time scales intrinsic to the system. For example, the diameter of an obstacle can define a length scale l_0, and the time it takes for the fluid to flow such a distance can define a characteristic time scale t_0. We can then express quantities within this problem in units of l_0 and t_0 by transforming

$$\begin{aligned}
\mathbf{r}' &= \frac{\mathbf{r}}{l_0} \\
t' &= \frac{t}{t_0} \\
\nabla' &= l_0 \nabla \\
\frac{\partial}{\partial t'} &= t_0 \frac{\partial}{\partial t} \\
p' &= \frac{t_0^2}{l_0^2 \rho_0} p \\
\mathbf{u}' &= \frac{t_0}{l_0} \mathbf{u}
\end{aligned} \tag{2.4}$$

to dimensionless quantities. By multiplying the resulting equation with t_0^2/l_0,

we find the dimensionless formulation of the Navier-Stokes equation

$$\frac{\partial}{\partial t'}\mathbf{u}' + (\mathbf{u}' \cdot \nabla')\,\mathbf{u}' = -\nabla' p' + \frac{1}{Re}\nabla'^2 \mathbf{u}' \,, \tag{2.5}$$

where the Reynolds number

$$Re = \frac{l_0^2}{\nu t_0} \,. \tag{2.6}$$

was introduced. Accordingly, boundary and initial conditions have to be expressed in terms of the characteristic length and time scales as well. Two physically different fluid dynamics problems might in this way be transformed into an identical mathematical problem. If this is the case, the resulting flows are called *dynamically similar.*

Since the Reynolds number is a combination of all characteristic quantities, it is often used to characterise the resulting flow. Typically, systems with $Re \ll 1$ feature only laminar flow without any turbulence. This regime is also referred to as the *Stokes' limit.* Karman vortex streets start to appear for $Re > 100$. For much faster flows, e.g., with $Re > 3000$, even flows in unobstructed geometries like a straight pipe become turbulent.

The general Reynolds number dependence is illustrated in Fig. 2.1. Both panels show velocity profiles within an identical Karman channel, where a circular obstacle is slightly offset from the middle of the channel. A Poisseuille velocity profile on the left, solid no-slip walls on the upper and lower boundaries and a zero-gradient velocity profile on the right were used as boundary conditions. The Reynolds number was adjusted by changing the kinematic viscosity of the fluid. While the flow is purely laminar and becomes virtually time-independent for $Re = 1$, vortex streets occur for $Re > 100$, leading to a time-dependent flow profile.

Figure 2.1: Flow through a Karman channel in the Stokes regime (laminar flow, $Re = 1$, bottom) and intermediate regime (Karman vortices, $Re = 200$, top). Colours indicate the absolute velocity $|\mathbf{u}|$.

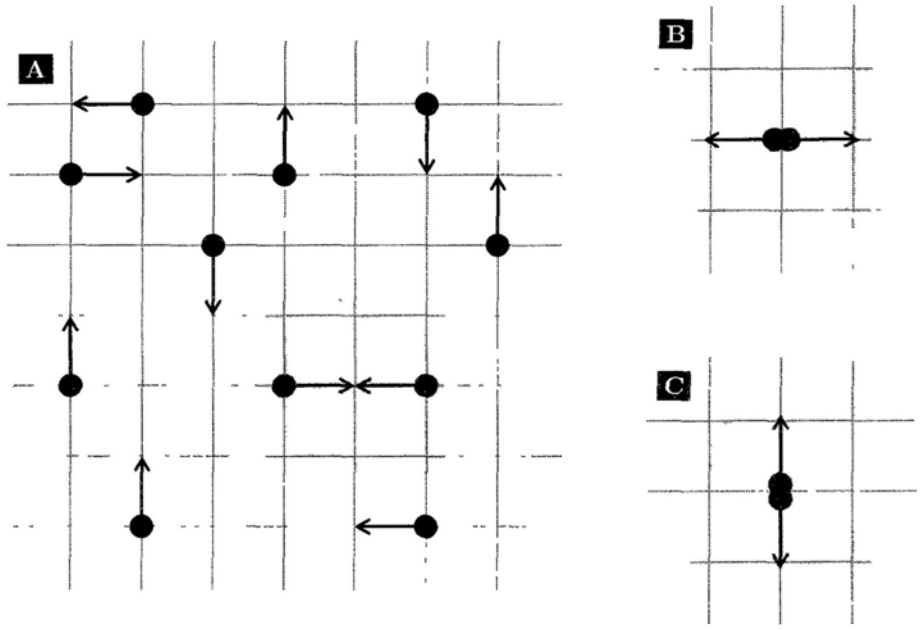

Figure 2.2: Schematic representation of a lattice-gas model. (A) Single pseudo-particles on the lattice grid. In the next time step, the two molecules in the grey area will collide. (B) The two possible resulting states, preserving energy and momentum.

2.2 The Lattice-Boltzmann Method

Like other methods to numerically solve the Navier-Stokes Equation, e.g., through finite difference methods, the lattice-Boltzmann method (LBM) is based on a discretisation of the fluid domain. However, unlike a direct solution of the Navier-Stokes Equation, the state of the fluid is not determined by the overall behaviour of the macroscopic variables, but rather through local interactions of neighbouring volumes.

The lattice-Boltzmann method originates from so-called lattice-gas models [21, 22, 23], which define pseudo-particle kinetics on a discrete lattice with

discrete times. Such a lattice-gas consists of pseudo-particles residing on lattice nodes. Each pseudo-particle itself already consists of a number of real gas molecules, i.e., the lattice-gas itself is already a coarse-grained model compared to real molecular dynamics simulations. Figure 2.2 exemplifies the dynamics of a lattice-gas: during a discrete time step, they move along a lattice vector to a neighbouring node, resulting in a discrete set of possible velocities. If at any time two particles arrive at the same lattice node, they collide and thereby change their velocities while preserving energy and momentum. Since these mappings of possible incoming velocities to resulting outgoing velocities form a discrete rule matrix, the lattice-gas models were also known as lattice-gas cellular automata.

The lattice is defined through a set of q lattice vectors $\mathbf{e}_i$, $i \in \{0, \ldots, q-1\}$ which connect neighbouring nodes. The state of a lattice-gas model is given by a set of binary occupation numbers $n_i(\mathbf{x}, t)$, giving the number of particles – zero or one – that occupy the lattice node with coordinate $\mathbf{x}$ at time t, having the discrete velocity $\mathbf{v}_i = \mathbf{e}_i/\delta t$. However, such a discrete approach carries a number of downsides, in particular large localised fluctuations and possible violations of Galilean invariance.

In order to overcome these downsides, and to better incorporate a statistical physics point of view into the model, the lattice-Boltzmann method was developed. The lattice-Boltzmann method can be seen as a coarse-grained lattice-gas method: Instead of discrete occupation numbers, the state of a small volume of liquid is given through a set of distribution functions $f_i(\mathbf{x}, t)$. These functions correspond to the amount of molecules at lattice node $\mathbf{x}$ at time t having velocity $\mathbf{v}_i$, chosen again from a discrete set. The macroscopic

variables of the fluid, i e , the density and velocity are given by

$$\rho = \sum_{i=0}^{q\ 1} f_i, \qquad \mathbf{u} = \sum_{i-0}^{q-1} \frac{f_i \mathbf{e}_i}{\rho \delta t} \equiv \sum_{i=0}^{q-1} \frac{\mathbf{j}_i}{\rho} , \tag{2 7}$$

where $\mathbf{j}_i$ is the momentum density in direction of $\mathbf{e}_i$

Since the discrete time step δt is commonly used as the reference time for the dimensionless formulation of the Navier-Stokes equation, it is equivalent to unity within the LBM system and therefore normally omitted

The evolution of the system is defined through the lattice-Boltzmann equation

$$f_i \left(\mathbf{x} + \mathbf{e}_i, t + \delta t\right) - f_i \left(\mathbf{x}, t\right) = \Omega_i(\boldsymbol{f}) , \tag{2 8}$$

which is a discretised version of the Boltzmann transport equation The collision operator Ω replaces the set of collision rules in the lattice-gas method Originally, the collision operator was modelled by a translation of the lattice-gas collision rules [24] Nowadays, the collision operator is commonly modelled using the Bhatnagar-Gross-Krook approach [25], i e , as an exponential decay towards an equilibrium function $f_i^{\mathrm{eq}}(\rho, \mathbf{u})$

$$\Omega_i(\boldsymbol{f}) = -\frac{f_i(\mathbf{x}, t) - f^{\mathrm{eq}}\left(\rho(\mathbf{x}, t), \mathbf{u}(\mathbf{x}, t)\right)}{\tau} \tag{2 9}$$

The validity of such an approach depends on various factors Key problems are a suitable choice of lattice vectors $\mathbf{e}_i$, which have to fulfil certain symmetry conditions, and an approximation of a equilibrium functions f_i^{eq} Today lattices with $q = 8 + 1$ vectors are used for $2D-$simulations while lattices with $q = 14+1$ $q = 18+1$ or $q = 26+1$ vectors are chosen for $3D-$simulations The $+1$ indicates that one of these vectors is the null vector $\mathbf{e}_0 = 0$ corresponding to molecules that will stay at the same lattice node The choice of lattice vectors is determined by symmetry conditions that have to be fulfilled for the

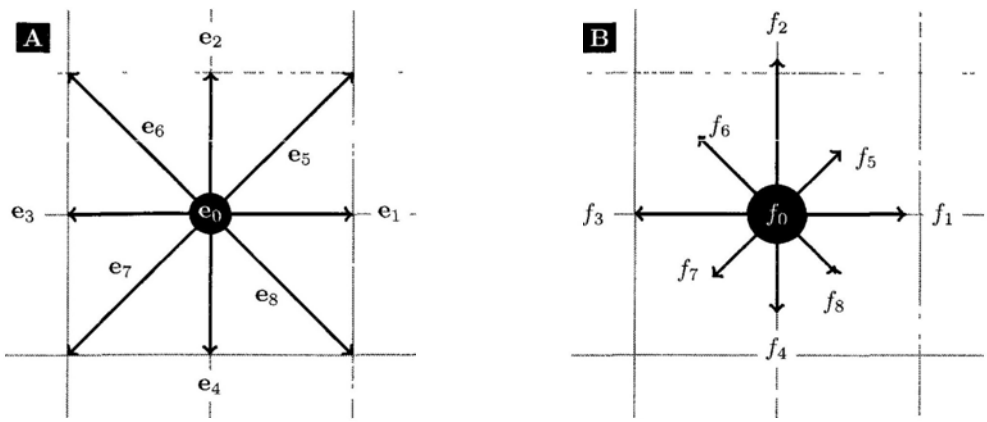

Figure 2.3: Lattice vectors for the D2Q9 lattice (A) and exemplary distribution function for the same system (B). The vector $\mathbf{e}_0$ is equivalent to molecules at rest.

LBM equation Eq. (2.8) to be equivalent to the Navier-Stokes equation. In what follows, we will focus on the D2Q9 lattice of a two-dimensional problem with nine lattice vectors. All our results can be extended to three-dimensional lattices in a straightforward manner. For a detailed discussion on the question of lattice symmetry, the derivation of the lattice-Boltzmann equation from the Navier-Stokes Equation, and the collision operator, see Refs. [22, 26] and the overviews listed at the beginning of Ch. 2.

The BGK collision operator depends on two quantities: the equilibrium distribution function f^{eq} and the relaxation time τ. To be numerically stable, the relaxation time has to fulfil $1/2 < \tau < \infty$. Generally, one distinguishes the regimes $1/2 < \tau < 1$ (or $1 < 1/\tau < 2$) and $1 < \tau < \infty$ (or $0 < 1/\tau < 1$), referred to as the over-relaxation regime and the sub-relaxation regime, respectively. These regimes correspond to an exponential decay ($1 < \tau < \infty$) or a damped oscillatory decay ($1/2 < \tau < 1$) to the equilibrium, with the

special case of $\tau = 1$ resulting in a direct replacement of the distribution function by the corresponding equilibrium distribution function It was shown that values of $\tau \approx 0\,8$ typically yield the most accurate results and we will use such a value of τ in the following calculations [27] However the choice of τ is not arbitrary, but is connected to the kinematic viscosity of the liquid through

$$\nu_{\mathrm{LBM}} = \frac{\tau - \frac{1}{2}}{c_S^2} \,, \tag{2 10}$$

where $c_S = 1/\sqrt{3}$ is the speed of sound in LBM units By choosing $\tau = 0\,8$, we thus effectively fix the value of the kinematic viscosity, as expressed in our simulations units δt and δx Hence, the scale factors between the lattice-Boltzmann units δx and δt and the physical units of the problem cannot be arbitrarily chosen This constraint is probably best illustrated with an example Let us assume a system where the fluid is normal water, which has a kinematic viscosity at room temperature of $\nu_{H_2O} \approx 10^{-6} m^2/s$ Let us further assume that our system is a square of side lengths $1mm$, which we want to discretise using 200×200 lattice nodes, thereby defining $\delta x = 5\mu m$ The viscosity, however, has to transform into our predefined LBM viscosity

$$\begin{aligned} 0\,1 = \frac{\tau - \frac{1}{2}}{c_S^2} = \nu_{\mathrm{LBM}} &= \frac{\nu_{\mathrm{phys}} \delta t}{\delta x^2} = \frac{10^{-6} m^2/s \times \delta t}{2\,5 \times 10^{-11} m^2} \\ \Rightarrow \delta t &= 2\,5 \mu s \end{aligned}$$

The equilibrium distributions f_i^{eq} are functions of the density and flow velocity at one lattice node It can be derived using a second order expansion of the Boltzmann equation which is valid in the case of small mach numbers, i e , as long as the flow velocities are much smaller than the speed of sound in the simulation [28] The exact form of the coefficients for the quadratic expansion can be found through symmetry conditions of the momentum flux tensor, which depends on the equilibrium distribution Although some ambiguity

exists in the choice of the coefficients, it has become convention to set the speed of sound in the D2Q9 model to

$$c_s = \frac{1}{\sqrt{3}} \frac{\delta x}{\delta t} \tag{2.11}$$

As a result, the remaining coefficients of the expansion are fixed, and the LBM equilibrium distribution becomes

$$f_i^{eq}(\rho, \mathbf{u}) = w_i \rho \left(1 + \frac{\mathbf{e}_i \cdot \mathbf{u}}{c_s^2} + \frac{1}{2} \frac{(\mathbf{u} \cdot \mathbf{e}_i)^2}{c_s^4} - \frac{1}{2} \frac{u^2}{c_s^2} \right) , \tag{2.12}$$

For the D2Q9 lattice, the weight factors are $w_0 = 4/9$, $w_j = 1/9$ for $j \in \{1, 2, 3, 4\}$ and $w_k = 1/36$ for $k \in \{5, 6, 7, 8\}$

During a computer simulation, the described evolution is typically split into three steps At first the macroscopic variables $\mathbf{u}$ and ρ, and thereafter the equilibrium distributions $\boldsymbol{f}^{\mathbf{eq}}$ are calculated from the distribution functions During the second, so-called *collision step* new values are calculated for the distribution functions

$$f_i^{new} = \left(1 - \frac{1}{\tau} \right) f_i^{old} + \frac{1}{\tau} f_i^{eq} \tag{2.13}$$

Finally the new distribution functions are propagated or *streamed* to the corresponding node

$$f_i(\mathbf{x} + \mathbf{e}_i, t + \delta t) = f_i^{new}(\mathbf{x}, t) \tag{2.14}$$

Hence, this step is often referred to as the streaming step

2.3 Boundary Conditions

Physically, the specification of a hydrodynamic problem is not complete until the state of the fluid on the boundary is given Such boundary conditions

specify the velocity or the pressure of the fluid on the boundary or define a relationship between the state of the fluid at two different points For example, in the case of periodic boundary conditions, the values of pressure and flow velocity at opposite ends of a unit cell have to be identical

$$\begin{aligned} \mathbf{u}(0,y,t) &= \mathbf{u}(L_x,y,t) \\ p(0,y,t) &= p(L_x,y,t) \end{aligned} \tag{2 15}$$

Physically and mathematically the problem is well defined if appropriate initial and boundary conditions are specified For the lattice-Boltzmann method, this is unfortunately insufficient The physical quantities which are defined on the boundary, are functions of the local distribution functions and not vice versa Defining the macroscopic variables hence does not unambiguously define the distribution functions Figure 2 4 illustrates this problem It shows a straight boundary in a D2Q9 system Six of the nine distribution functions are well defined after the streaming step while the three remaining functions are undefined Periodic boundary conditions are an exceptional case where the physical periodicity conditions Eq (2 15) can just be applied to the distribution functions f_i itself In general, additional assumptions have to be made to turn physical boundary conditions into specifications for LBM boundary distribution functions The creation of novel LBM boundary conditions has therefore been a continuous focal point of research since the emergence of the lattice-Boltzmann method itself In the following, we will discuss some of the more commonly employed LBM boundary conditions, and in particular focus on the generalised periodic boundary conditions that allow to exploit periodicity in pressure-driven flows

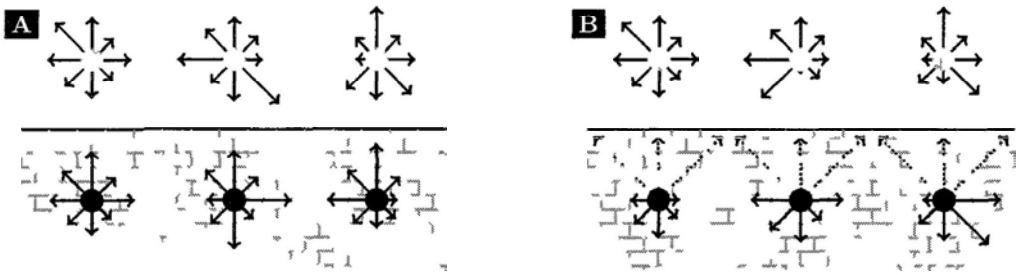

Figure 2.4 A horizontal boundary of a lattice-Boltzmann simulation. Before streaming, both BGK-nodes (light grey) and boundary nodes (black) have a full set of distribution functions (A). After the streaming step, the boundary nodes have an incomplete set of boundary conditions, since no nodes below exist (B). The missing distribution functions (dotted arrows) have to be calculated from macroscopic conditions or by other methods (see text).

2.3.1 Simple Periodic Boundary Conditions

Periodic boundary conditions are commonly employed in various problems in physics. For a fluid dynamics problem, they would be defined on both the pressure and velocity of the fluid [29]:

$$\begin{aligned} \mathbf{u}(\mathbf{x},t) &= \mathbf{u}(\mathbf{x}+\mathbf{l},t) \\ p(\mathbf{x},t) &= p(\mathbf{x}+\mathbf{l},t) \end{aligned} \tag{2.16}$$

These definitions can be directly mapped on a LBM lattice. Let us assume that such simple periodic boundary conditions (SPBC) are used in x-direction, and that boundary nodes are located at $x = 0$ and $x = L_x + \delta x$. In such a setup, SPBC are defined as

$$\begin{aligned} i \in \{1,5,8\} \quad f_i(0,y) &= f_i(L_x,y) \\ i \in \{3,6,7\} \quad f_i(L_x+\delta x,y) &= f_i(\delta x,y) \end{aligned} \tag{2.17}$$

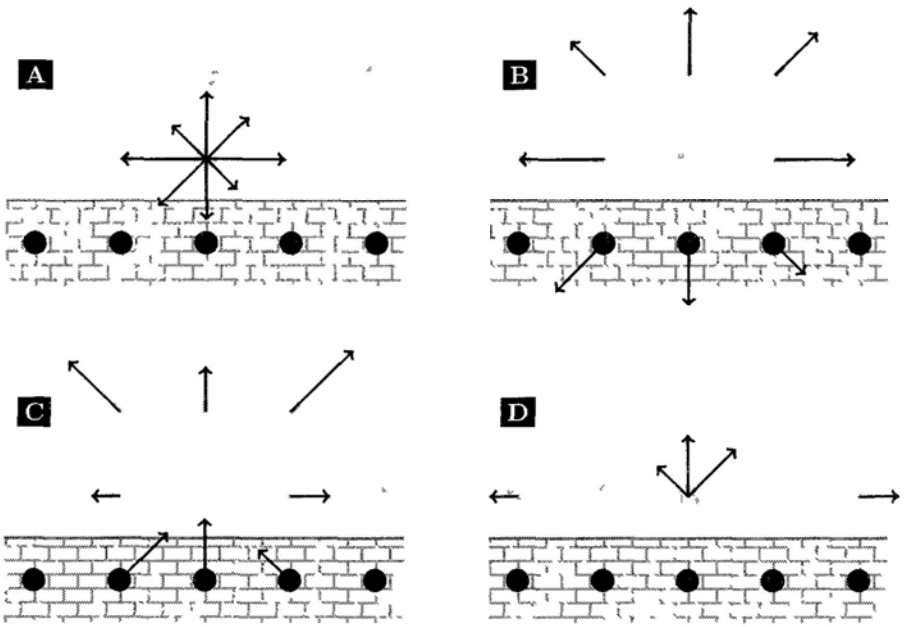

Figure 2.5. Illustration of the difference between bounce-back and BGK dynamics. (A) Original pre-streaming configuration. (B) Post-streaming (C) Collision versus bounce-back. (D) Post-streaming.

2.3.2 Bounce-Back Boundary Conditions

No-slip, mid-plane bounce-back boundary conditions are among the most commonly used boundary condition schemes for lattice-Boltzmann boundary conditions [30]. Lattice nodes with bounce-back dynamics replace the BGK collision step with an inverting of momentum of molecules at that node. This mechanism is illustrated in Fig. 2.5. All panels show an interface between a liquid with BGK dynamics and a solid no-slip wall using bounce-back dynamics. The distribution functions of one node are shown before the streaming step (Fig. 2.5(A)). After streaming, these distributions have moved to adjacent lattice nodes. Three of these nodes follow bounce-back dynamics (Fig. 2.5(B)).

During the following collision step, the distribution functions on BGK nodes are changed, depending on the overall distribution at the respective node. In contrast, distribution functions on bounce-back nodes are simply mapped on the function of the opposite direction (Fig. 2.5(C)). After the next streaming steps, these mirrored functions have again reached the original node (Fig. 2.5(D)).

While bounce-back dynamics are numerically accurate in $\mathcal{O}(\delta x)$, they can be easily implemented even for the most convoluted boundaries, making them very popular in LBM simulations [31]. They are particularly helpful in the study of liquid flows through porous media, where boundary conditions can be created directly from electronic images of the porous matter.

2.3.3 Velocity Boundary Conditions

A velocity boundary condition specifies a velocity profile $\mathbf{u}(\mathbf{x}, t)$ on the boundary of the domain. The problem is then physically and mathematically well defined, but the LBM boundary conditions are not. For a straight boundary on a D2Q9 lattice, we have 6 specified and 3 unspecified distributions on a boundary node. In addition, the velocity boundary conditions define two further constraints:

$$\begin{aligned} \rho u_x &= f_1 + f_5 + f_8 - f_3 - f_6 - f_7 \\ \rho u_y &= f_2 + f_5 + f_6 - f_4 - f_7 - f_8 \end{aligned}$$

This leads to an underdetermined system of equations. To determine a single solution, additional constraints have to be defined. In the most commonly taken approach, developed by Zou and He[32], it is assumed that the non-equilibrium contribution orthogonal to the boundary is bounced back, e.g., at a horizontal boundary.

$$f_2 - f_2^{eq} = f_4 - f_4^{eq} \tag{2 18}$$

Alternative methods include approaches that alter all boundary populations in order to allow for greater numerical stability in the turbulent regime New populations are calculated from the density, the pre-defined velocity, and the stress tensor [33] However for low Reynolds number regimes, the differences in these methods are marginal

2.3.4 Pressure Boundary Conditions

The situation is similar if a pressure profile rather than a density profile is defined However, the definition of the pressure only offers a single constraint

$$\sum_{i=0}^{Q-1} f_i = \rho \tag{2 19}$$

Hence, two additional assumptions are made for one the aforementioned assumption that bounce-back mechanics apply to the non-equilibrium contribution of the orthogonal component for another that the velocity component orthogonal to the boundary vanishes, e g , again for a horizontal boundary

$$\begin{aligned} f_2 - f_2^{eq} &= f_4 - f_4^{eq} \\ f_1 + f_5 + f_8 - f_3 - f_6 - f_7 &= 0 \end{aligned} \tag{2 20}$$

2.4 Pressure-Driven Flows in Repetitive Geometries

Fluid flows through confined geometries, e g , a simple duct or pipe, are often driven by a pressure gradient Such a pressure gradient can be caused by gravity, or simply by connecting the ends of the duct to reservoirs of different pressure As discussed before, boundary conditions for a specified boundary pressure have been defined If the pressure profile on the boundary is known, such pressure-driven flows can be readily simulated

A common problem, encountered for example in the simulation of microfluidic devices, is that the liquid flows through a repetitive geometry of identical unit cells Each single unit cell could be simulated using the lattice-Boltzmann method but the solution of the entire flow exceeds the dimensions that can be tackled with modern computer systems It appears sensible that the periodicity of the geometry should be exploited Simple periodic boundary conditions, however, can not be used, since this would eliminate the force driving the flow

As an preliminary remedy, the pressure gradient was replaced by a so-called body force driving the flow Body forces alter the equilibrium distribution in such a way that the equilibrium distribution of density ρ and velocity $\mathbf{u}$ does not add up to the same velocity

$$\frac{\sum_{i=0}^{Q-1} f_i^{\mathrm{eq}}(\rho, \mathbf{u})\mathbf{e}_i}{\rho} \neq \mathbf{u} \tag{2 21}$$

Body force approaches were initially developed to incorporate inertial and gravitational forces into lattice-Boltzmann simulations [34, 35] By replacing the pressure gradient with a body force as the force driving the flow, exploiting periodicity becomes simple since simple periodic boundary conditions can be

used. However, it has been argued that the body force approach is not equivalent to a pressure gradient if the flow geometry does not possess a uniform cross section [36]. Hence, more advanced generalised periodic boundary conditions (GPBC) are needed that incorporate the density gradient as a driving force

2.5 Generalised Periodic Boundary Conditions with Pressure Gradients

2.5.1 Existing Models

The general problem is shown in Fig. 2.6. A fluid is driven through a repetitive geometry by the pressure difference between the outer reservoirs $\Delta\rho = \rho_A - \rho_B$. The entire array can be divided into M_x unit cells, each of which has dimensions $L_x \times L_y = N_x \times N_y \times \delta x^2$ Instead of simulating the entire system at a great expense of computation power and thereby sacrificing accuracy, simulating only a single unit cell is highly advantageous. If a single unit cell is simulated, the distribution functions on the outer boundary nodes f_i', i.e., the nodes directly outside the unit cell, are undefined To define these populations, relations between the distribution function flowing out of the unit cell at one end f_i and those flowing in from outer boundary nodes f_i' at the other end have to be derived

Two different approaches have been proposed to combine pressure differences with periodic boundary conditions [37, 12]. They differ mainly in the quantity that is assumed to be periodic. The first proposed method by Zhang

and Kwok [37] assumed periodicity in the flow velocity combined with a pressure gradient

$$\begin{aligned} \mathbf{u}(x,y) &= \mathbf{u}(x+L_x,y) \\ p(x,y) &= p(x+L_x,y)+\delta p \\ \rho(x,y) &= \rho(x+L_x,y)+\delta\varrho_x \end{aligned} \tag{2 22}$$

This approach was realised by simply rescaling the particle distribution functions If $f' \equiv \alpha f$, the density is simply rescaled by the factor α, but the velocity remains unchanged

As a physical boundary condition, these equation have a caveat the underlying assumption of this approach is that of an incompressible flow, for which the periodicity of the velocity is reasonable However, since the equation of state of the lattice-Boltzmann method directly relates pressure and density,

$$p = \frac{1}{c_S^2}\rho \ ,$$

this method leads to erroneous results Consequently, Kim and Pitsch proposed another boundary condition [12] that requires periodicity in the momentum density $\mathbf{j}$ instead

$$\begin{aligned} \rho\mathbf{u}(x,y) &= \mathbf{j}(x,y) = \mathbf{j}(x+L_x) \\ \rho(x,y) &= \rho(x+L_x,y)+\Delta\varrho_x \end{aligned} \tag{2 23}$$

While this approach is more accurate it is more complicated to implement If the momentum density has to remain constant while a density gradient is applied, the flow velocity at the inflow has to be smaller than at the outflow To implement this requirement, Kim and Pitsch splitted the distribution functions into an equilibrium and a non-equilibrium distribution

$$f_i^{\mathrm{neq}}(\mathbf{x},t) = f_i(\mathbf{x},t) - f_i^{\mathrm{eq}}(\rho(\mathbf{x},t),\mathbf{u}(\mathbf{x},t)) \tag{2 24}$$

The equilibrium part is simply given by the equilibrium distribution calculated according to Eq (2 12) The non-equilibrium distribution can hence be negative Its contribution to both fluid velocity and density is neutral

$$\begin{aligned} \sum_{i=0}^{q-1} f_i^{\mathrm{neq}} &= 0 \\ \sum_{i=0}^{q-1} f_i^{\mathrm{neq}} \mathbf{e}_i &= 0 \end{aligned} \tag{2 25}$$

Kim and Pitsch's central assumption is that while the equilibrium distribution between a position in different unit cells will differ in order to fulfil conditions (2 23), the non-equilibrium distributions will be fully periodic Hence, the full set of periodicity rules becomes

$$\begin{aligned} \rho(x + L_x, y) &= \rho(x, y) - \delta\varrho_x \\ \mathbf{u}(x + L_x, y) &= \mathbf{u}(x, y)\frac{\rho(x, y)}{\rho(x, y) - \delta\varrho_x} \\ f_i^{\mathrm{eq}}(x, y) &= f^{\mathrm{eq}}(\rho(x, y), \mathbf{u}(x, y)) \\ f_i^{\mathrm{eq}}(x + L_x, y) &= f^{\mathrm{eq}}\left(\rho(x, y) - \delta\varrho_x, \mathbf{u}(x, y)\frac{\rho(x, y)}{\rho(x, y) - \delta\varrho_x}\right) \\ f_i^{\mathrm{neq}}(x, y) &= f_i(x, y) - f_i^{\mathrm{eq}}(\rho(x, y), \mathbf{u}(x, y)) \\ f_i(x + L_x, y) &= f^{\mathrm{eq}}(x + L_x, y) + f_i^{\mathrm{neq}}(x, y) \end{aligned} \tag{2 26}$$

The differences between the two approaches are illustrated in Fig 2 7 Figure 2 7(A) shows an exemplary distribution function assumed to be somewhere at the outflow of the unit cell, corresponding to the right purple node in Fig 2 6 It is assumed that the density difference over this unit cell is $\delta\rho = \rho_0/2$ with ρ_0 being the average density $\overline{\rho}(x = L_x)$ of the unit cell Figure 2 7(B) shows the resulting distribution using the Kim/Pitsch method at the purple inflow node The non-equilibrium parts are unchanged while the equilibrium parts are changed according to a slower moving but denser flow

Figure 2.7(C) shows the results of the Zhang/Kwok method. Both equilibrium and non-equilibrium are simply rescaled, resulting in an increased mass flow.

As the Zhang/Kwok method does not preserve the momentum density, and was furthermore shown to yield less accurate results [12], we will in the following use the Kim/Pitsch periodic boundary conditions with pressure gradients.

It should be noted, though, that only the long-time limit of the simulation is a solution for the fully developed flow. This means that the solution has to become stationary before it is applicable. Initial effects, such as the behaviour of the fluid once the pressure gradient is activated, do not occur in all unit cells at the same time or in the same way. This effectively invalidates the periodic relationships in Eq. (2.22) and Eq. (2.23) while the flow is not yet fully developed. If the time evolution of the flow through a such a geometry is of interest, then indeed the entire system has to be simulated. Consequently, we also focus on the Stokes limit, i.e., the case of very small Reynolds numbers. For high Reynolds numbers, turbulences cause a permanent time-dependence of the flow, and thus no steady final state exists.

2.5.2 Implementation of the Kim & Pitsch Boundary Conditions

The common use of the Kim/Pitsch (KP) method differs slightly from the theoretical derivation. In theory, only the density gradient over exactly one period, i.e., $\Delta\varrho_x = \rho(x,y) - \rho(x+L_x,y)$, is defined. This gradient can already be used to specify the densities on the inflow and outflow columns $x = 0$ and $x = L_x + \delta x$. However, since initially the density over the unit cell is constant, this creates an initial gradient between $x = 0$ and $x = L_x + \delta x$ of nearly $2\Delta\varrho_x$ and thereby causes a prolonged initialisation period. Hence, typically

two average densities $\rho_L = \overline{\rho}(x = 0)$ and $\rho_R = \overline{\rho}(x = L_x + 1)$ are externally defined. The densities at single points on the inlet and outlet columns are then defined through

$$\begin{aligned} \rho(0, y) &= \rho_L + \rho(L_x, y) - \overline{\rho}(L_y) \\ \rho(L_x + \delta x, y) &= \rho_R + \rho(\delta x, y) - \overline{\rho}(\delta x) \ . \end{aligned} \tag{2.27}$$

The quantities $\overline{\rho}(\delta x)$ and $\overline{\rho}(L_x)$ are measured directly inside the simulation. The flow velocities on the boundary are set to

$$\begin{aligned} \mathbf{u}(0, y) &= \frac{\rho(L_x, y)\mathbf{u}(L_x, y)}{\rho(0, y)} \\ \mathbf{u}(L_x + \delta x, y) &= \frac{\rho(\delta x, y)\mathbf{u}(\delta x, y)}{\rho(L_x + \delta x, y)} \ . \end{aligned} \tag{2.28}$$

With these definitions, the inflowing distributions are calculated as

$$\begin{aligned} f_i^{'}(0, y) &= f_i^{\mathrm{eq}}(\rho(0, y), \mathbf{u}(0, y)) \\ &+ f_i(L_x, y) - f_i^{\mathrm{eq}}(L_x, y) \\ f_i^{'}(L_x + \delta x, y) &= f_i^{\mathrm{eq}}(\rho(L_x + \delta x, y), \mathbf{u}(L_x + \delta x, y)) \\ &+ f_i(\delta x, y) - f_i^{\mathrm{eq}}(\delta x, y) \ . \end{aligned} \tag{2.29}$$

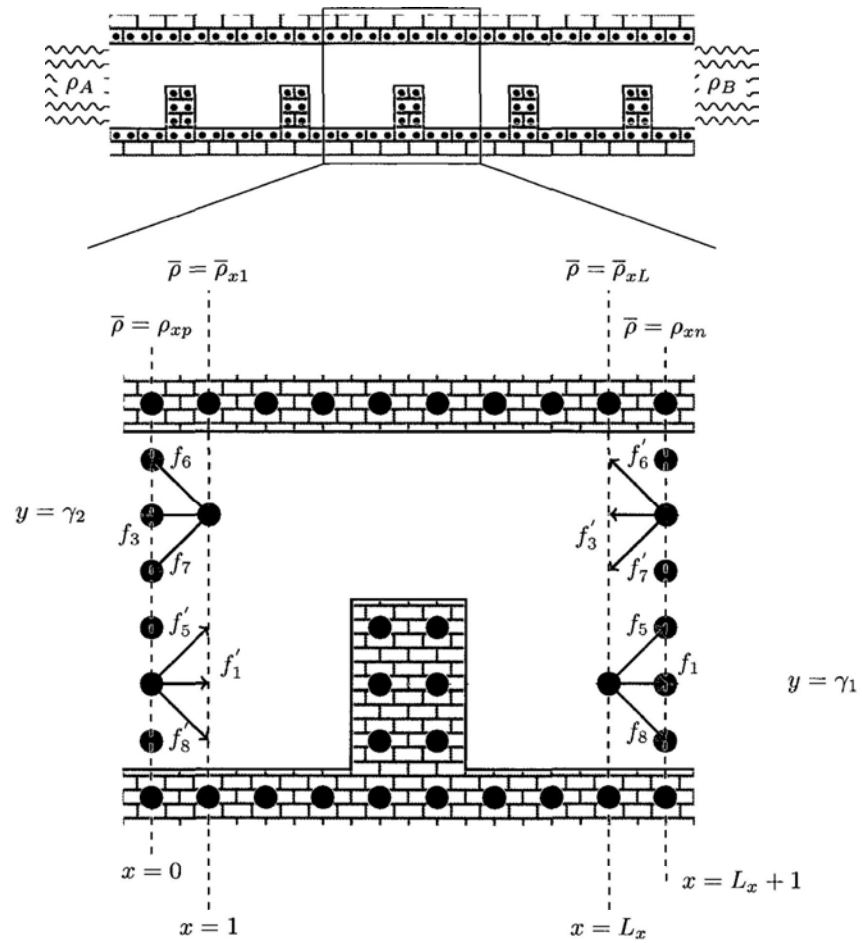

Figure 2.6: Schematic description of pressure-driven flows in 1D-periodic geometries. A geometry with a repetitive pattern connects two reservoirs of different pressure. To simulate a single unit cell, rules have to be defined relating outflows f and inflows f' on nodes with a periodic relationship, here shown in identical colours. The density relations of the Kim-Pitsch boundary conditions are explicitly listed. The different grey-levels indicate different dynamics, i.e., light grey for BGK dynamics, dark grey for outer boundary nodes, and black for bounce-back dynamics.

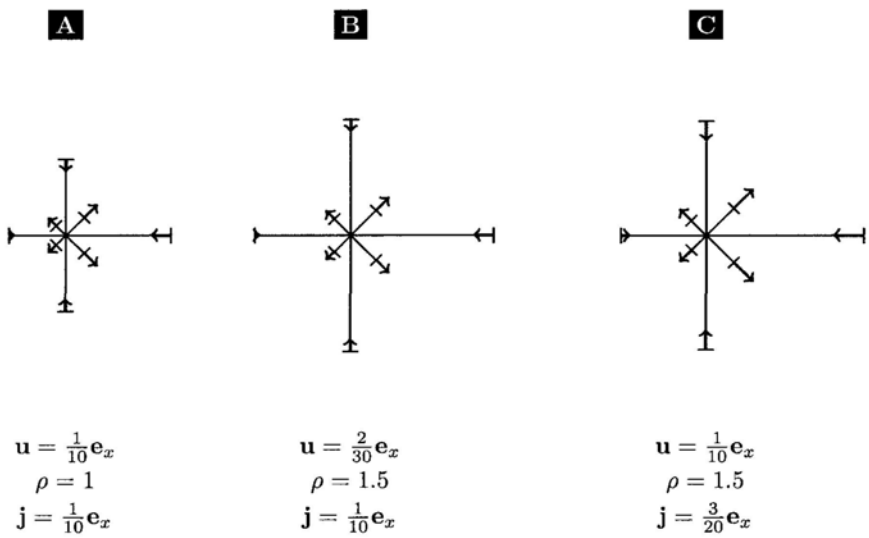

Figure 2.7: Different periodicity rules for Zhang/Kwok and Kim/Pitsch generalised periodic boundary conditions. Each distribution function is split into its equilibrium (until the flat end) and non-equilibrium distribution (from the flat end to the arrow tip). (A): particle distribution function at some node at $x = L_x$. (B): resulting distributions at $x = 0$ for the Kim/Pitsch model. (C): resulting distribution at $x = 0$ for the Zhang/Kwok model. Both cases correspond to a pressure difference of $\delta\rho_x = 1/2\rho(L_x)$.

Chapter 3

Adaptive Generalised Periodic Boundary Conditions

3.1 Methodology

The problem discussed in Sec. 2.5.1 can further be complicated if the geometry is repetitive in more than one dimension. Such a case is typically found among microfluidic devices, where a 2D-array of $M_x \times M_y$ unit cells is confined by solid walls, such as shown in Fig. 3.1. With the previous methods, a *columnar unit cell* that extends over an entire column, shown in red in this figure, could be simulated. However, this would come at a great computational expense, as such structures can easily extend over many hundred cells. Finding ways to simulate a *single unit cell* (highlighted in green) is therefore highly desirable. However, it is not always possible to just use simple periodic boundary conditions on the upper and lower boundary of the green unit cell. If the cell's obstacle geometry is asymmetric, a net momentum in $y-$direction will be transferred between the fluid and the obstacle, leading to a net mass

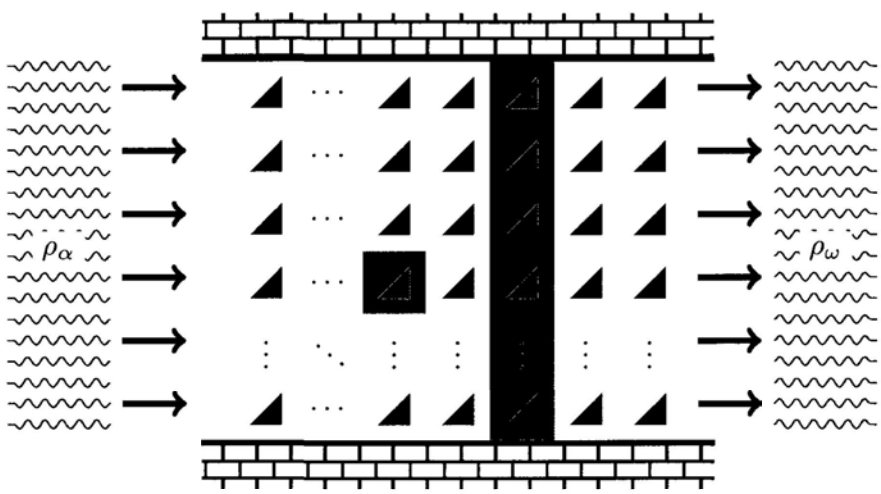

Figure 3.1: Schematic layout of a microfluidic array device. A 2D-array of identical obstacles is placed inside a duct and confined by solid walls. A pressure difference between the reservoirs $\Delta\rho = \rho_\alpha - \rho_\omega$ drives a flow through this geometry. The column-like unit cell that can be simulated with KP-boundary conditions is highlighted in red, while a single geometrical unit cell is highlighted in green.

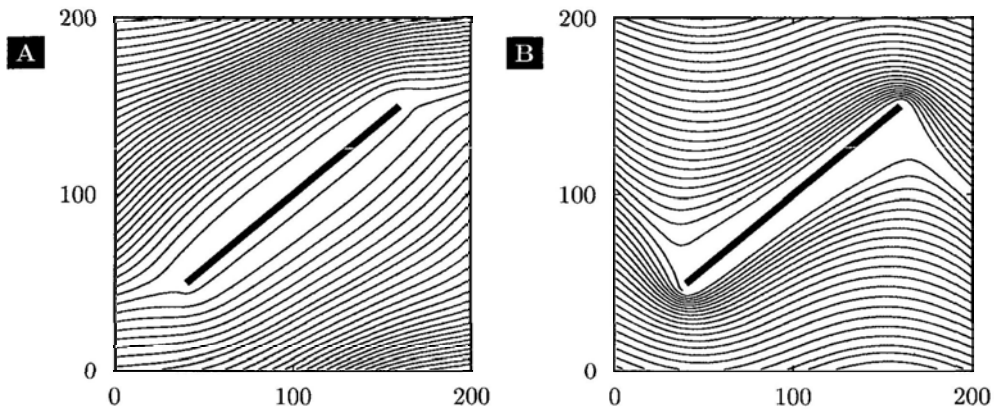

Figure 3.2: Comparison of the flow lines of a unit cell of $N_x = N_y = 200$ excluding (A) or including (B) the effects of outer solid walls. (B) Flow lines enter and exit at the same $y-$value. (A) Flow lines are shifted upwards significantly.

flow in $y-$direction

$$j_\perp(y) = \int_x^{x+L_x} j_y(x,y)\mathrm{d}x \ . \tag{3.1}$$

Through the effects of the solid wall boundaries at the bottom and top of the array, such a flow cannot exist forever. Instead, it leads to a density gradient in $y-$direction, which itself acts as a force:

$$\rho(x,y) - \rho(x,y+L_y) = \Delta\varrho_y \ . \tag{3.2}$$

In the final steady state, the resulting force caused by the density gradient and the force from the asymmetric obstacle balance, and the momentum flow in y-direction vanishes.

An illustration why this density gradient cannot be ignored is shown in Fig. 3.2. The obstacle design of a single unit cell is a thin, inclined rectangle, deflecting the flow upwards. Both panels show the resulting flow lines. Fig. 3.2(A) is a simulation of a single unit cell, using KP boundary conditions with a pressure gradient in x-direction to drive the flow. Simple periodic

boundary conditions are used in y-direction The results show that the flow lines leave the unit cell at a higher point than they enter it, indicating a net upward momentum is induced In contrast, Fig 3 2(B) shows no such upward momentum, with each flow line leaving the unit cell at the same level as it entered it Data for Fig 3 2(B) was obtained by simulating a columnar unit cell consisting in this example of only $M_y = 3$ rows The outer walls were explicitly included in the simulation Afterwards the data of the central unit cell in this columnar array was used to create Fig 3 2(B)

In order to be able to simulate only one single unit cell, we need to use generalised periodic boundary conditions that incorporate the pressure gradient in y-direction To do so, we use the KP boundary conditions and define two average densities over the cell's top and bottom outer boundaries

$$\begin{aligned} \rho_{\mathrm{B}} &= \overline{\rho}(y = 0) \\ \rho_{\mathrm{T}} &= \overline{\rho}(y = L_y + \delta x) \\ \rho_{\mathrm{B}} - \rho_{\mathrm{T}} &= \delta\rho_y \end{aligned} \tag{3 3}$$

The density difference in y-direction has to be chosen in such a way that the flow in y-direction $j_\perp(y)$ vanishes

$$\forall y \in [1, L_y] \quad j_\perp(y) \stackrel{!}{=} 0 \tag{3 4}$$

The flow through any single line can fluctuate significantly, particularly in the early stage when sound waves are traveling through the cell We can replace condition Eq (3 4) as follows Instead of suppressing the flow through any single line, we require that the total y-momentum of the fluid within the unit cell vanishes

$$j_y^{\mathrm{tot}} = \int_V j_y \mathrm{d}x\mathrm{d}y = \sum_{k=1}^{N_x} \sum_{l=1}^{N_y} \sum_{i=0}^{8} \mathbf{e}_y \ \ \mathbf{e}_i f_i(k\delta x, l\delta x) \stackrel{!}{=} 0 \tag{3 5}$$

Here, the numbered vectors $\mathbf{e}_i$ refer to the lattice vectors of the LBM simulation, while $\mathbf{e}_y$ is the basis vector in y-direction of the coordinate systems (and hence identical to $\mathbf{e}_2$)

This condition is not yet equivalent to Eq (3 4) Eq (3 5) is still fulfilled if each line itself has a positive or negative y-flow as long as these flows cancel when summed up over the entire unit cell A possible scenario is an inflow from the left boundary that partially leaks out If the leakage through the upper and lower boundary is equal then the condition $j_y^{\mathrm{tot}} = 0$ might be fulfilled However, it is impossible for such a state to occur periodically, as the outflow of one unit cell has to be the inflow of another Therefore, we require as a second condition that the leakage through the upper and lower cell boundaries,

$$\begin{aligned} \Phi_y &= \oint_{\partial V} j_y \mathbf{e}_y \mathrm{d}\mathbf{o} = \sum_{k=1}^{N_x} \left(\sum_{i=2\,5\,6} f_i(k\delta x, L_y) - f_i(k\delta x, 0) \right. \\ &+ \left. \sum_{i=4\,7\,8} f_i(k\delta x, \delta x) - f_i(k\delta x, L_y + \delta x) \right) , \end{aligned} \tag{3 6}$$

vanishes separately In terminology of systems engineering, j_y^{tot} and Φ_y are referred to as *control variables* We can control j_y^{tot} through adjusting $\delta\rho_y$ and Φ_y through ρ_{B} (see Eq (3 3)), respectively The quantities $\delta\rho_y$ and ρ_{B} are in systems engineering referred to as the *actuating variables* of their respective control variable Both actuating variables are adjusted using a standard proportional-differential (PD) controller algorithm [38], such that

$$\begin{aligned} -\frac{\mathrm{d}}{\mathrm{d}t}\Delta\rho_y &= K_{1d}\frac{\mathrm{d}}{\mathrm{d}t} j_y^{\mathrm{tot}} + K_{1p} j_y^{\mathrm{tot}} \\ -\frac{\mathrm{d}}{\mathrm{d}t}\rho_{\mathrm{B}} &= K_{2\mathrm{d}}\frac{\mathrm{d}}{\mathrm{d}t}\Phi_y + K_{2p}\Phi_y \end{aligned} \tag{3 7}$$

The mechanisms of such an algorithm are simple Let us assume an asymmetric obstacle design that generates positive y-momentum, e g , the triangular obstacles used in all our example figures Through the so-called linear term K_p,

a positive y-momentum leads to an increase in the countering adaptive density gradient, and vice versa The resulting oscillatory decay is damped through the inclusion of a so-called differential term K_d, which increases the adaptive density gradient if j_y^{tot} is increasing even if it is still negative Suitable choices can be found with elementary methods of control system theory [38] We will in the following refer to this setup as adaptive generalised periodic boundary conditions (AGPBC)

The full relationship between boundary nodes using AGPBC is shown in Fig 3 3 Distribution functions on the outer boundary nodes have to be derived according to Eqs (2 27)-(2 29) Additional problems arise since the distribution functions on the outer boundary nodes at the corners can not be defined in this manner The average densities (ρ_B etc) are defined as averages over one line of boundary nodes of a directly adjacent unit cell In contrast the corner nodes belong to a unit cell shifted in both dimensions, e g , above and shifted to the right We cannot directly define the density at these nodes, and hence have to resort to the original boundary conditions

$$\begin{aligned} \rho(0,0) &= \rho(L_x, L_y) + \Delta\varrho_x + \Delta\varrho_y \\ \rho(L_x + \delta x, 0) &= \rho(\delta x, L_y) - \Delta\varrho_x + \Delta\varrho_y \\ \rho(0, L_y + \delta x) &= \rho(L_x, \delta x) + \Delta\varrho_x - \Delta\varrho_y \\ \rho(L_x + \delta x, L_y + \delta x) &= \rho(\delta x, \delta x) - \Delta\varrho_x - \Delta\varrho_y \end{aligned} \tag{3 8}$$

However, since we define the density gradients between the outer boundaries $\delta\rho_{x/y}$ the differences over exactly one period $\delta\varrho_{x/y}$ are not a-priori known We have to measure them in simulation as

$$\begin{aligned} \Delta\varrho_x &= \overline{\rho}(x = 0) - \overline{\rho}(x = N_x\delta x) \\ \Delta\varrho_y &= \overline{\rho}(y = 0) - \overline{\rho}(y = N_y\delta x) \end{aligned} \tag{3 9}$$

3.2 Simulation Results

To validate our method, we first need to define a control system. Generally, the use of a single unit cell, taken from a full $M_x \times M_y$ array with extensive dimensions M_x and M_y, as the control system would be appropriate. However, computational constraints do not allow the simulation of such an array unless very small unit cells are used. We hence use the KP boundary conditions, whose accuracy was already demonstrated for systems with one-dimensional periodicity [12], to reduce the system to an $1 \times M_y$ array. Such an array of unit cells of dimension $N_x = N_y = 200$ can still be simulated for a column of $M_y = 7$ unit cells. Each cell contains one triangular obstacle of height $h = 1/2L_y$. We use regularised zero-velocity boundary conditions to simulate the solid walls at $y = 0$ and $y = 1401\delta x$ [33, 15]. For this design, the introductory length is less than two unit cells, i.e., the inner cells behave virtually identical We will use the innermost of these cells as our control system. When referring to the entire seven-cell system, we will use the term control array.

Following current literature, we set the LBM relaxation time to $\tau = 0.8\delta t$ for optimal numerical accuracy. Setting the time constant implicitly also fixes the inter-simulation kinematic viscosity to $\nu^{\mathrm{LBM}} = \delta x^2/10\delta t$. Since our method is valid for the fully-developed state of time-independent and hence turbulence-free flows only, the flow has to be restricted to the Stokes regime. We therefore choose a density difference in x-direction of $\Delta\rho/\overline{\rho} \approx 10^{-5}$ by setting $\rho_{\mathrm{L}} = 1.00001$ and $\rho_{\mathrm{R}} = 1$ for both the AGPBC system and the control array. The Reynolds number calculated from the resulting flow velocity of

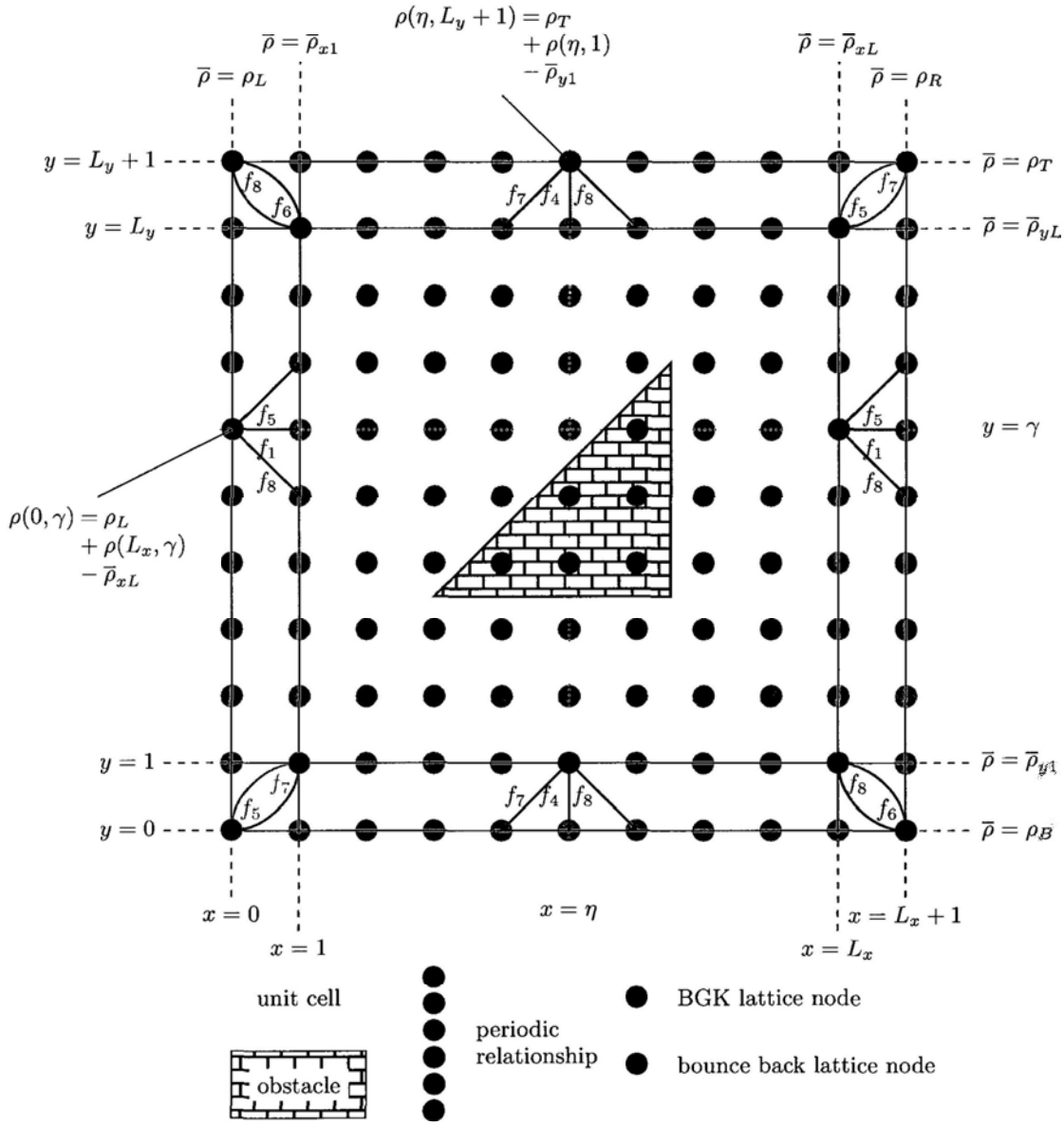

Figure 3.3: Periodic relationships in the 2D AGPBC model. Nodes of identical color have the same location in different unit cells. The highlighted distribution functions hence have to be transformed in accordance with Eqs. (2.27)-(2.29).

$u \approx 10^{-}4\delta x/\delta t$, the horizontal length of the triangle $l = 100\delta x$ and the kinematic viscosity is $Re \approx 10^{-1}$. This can be seen as an upper boundary for the validity of our method. For faster flow velocities, small time-dependent fluctuations occur. The method can still be used at $Re \approx 10$, but the magnitude of these fluctuations will significantly exceed the accuracy that our method can offer, and quantitative comparisons hence become meaningless. However, typical microfluidic devices operate significantly below this regime. For example, even the highest velocities used for deterministic lateral displacement result in a Reynolds number of $Re \approx 10^{-4}$ [39, 40].

The fluid in the system is initially inert. After the density gradient in x-direction becomes active, no adaptive gradient is used in the AGPBC system for an initialisation period of $t^{\text{init}} = 10,000\,\delta t$ in order to avoid initial effects affecting the controller algorithm. Afterwards, the adaptive gradient $\Delta\rho_y$ is adjusted using[1] $K_{1d} = 0.8 \times 10^{-5}, K_{1p} = 0.8 \times 10^{-6}$. The parameters for the lower boundary density ρ_B are $K_{2d} = 0.5 \times 10^{-5}$, $K_{2p} = 0.5 \times 10^{-4}$.

The system was simulated for a total of $t = 400,000\,\delta t$ steps, at which time the evolution of all quantities was limited by machine precision. In the following, long-time limits or final values are always meant to imply the state of the system after machine precision was reached.

Figure 3.4 shows the initial evolution of the adaptive pressure gradient in comparison with the emergence of the density differences over different unit cells inside the control array. After the initialisation period, a very short transient period with strong oscillations follows. The first oscillation's amplitude actually exceeds the final value of the adaptive pressure gradient by a factor

[1] It might be surprising that the gain coefficient K_p of the gradient is two orders of magnitude smaller than that of the lower density. This is caused by the control quantity $\jmath_y^{\text{tot}}$ is summed over N_y times as many nodes compared to Φ_y, which the coefficients need to compensate for.

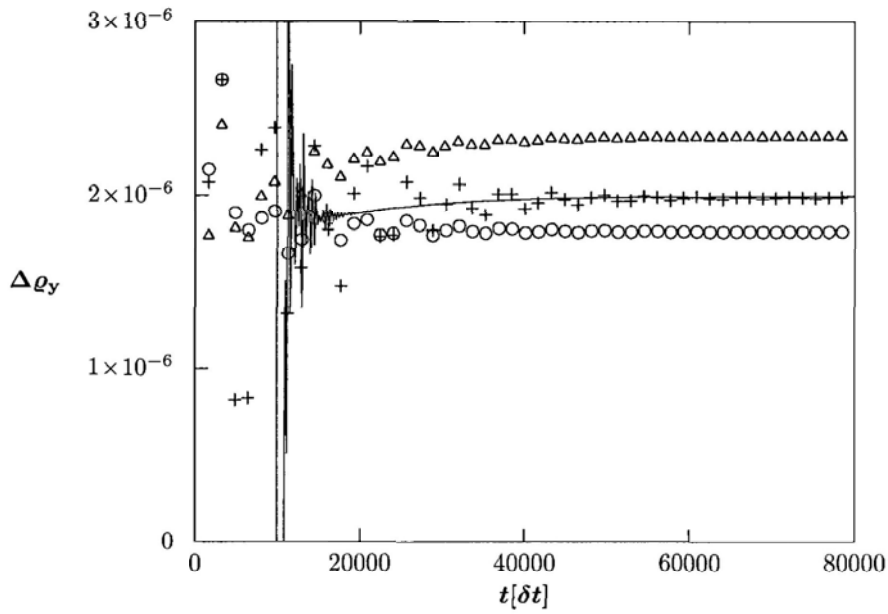

Figure 3.4: Evolution of the adaptive density gradient (solid line), compared to the density difference over the topmost (green circles), central (blue crosses) and bottommost (red triangles) unit cells of the control array.

of four. However, these oscillations are quickly suppressed through the differential term in the controller loop. After $t > 20,000\,\delta t$, oscillations have nearly subsided. The adaptive density gradient now approaches its long-time value even faster and with less fluctuations than the gradient over the control system.

Notably, the density gradients over the two outermost cells differ significantly from those over the AGPBC system or over the control cell. This is caused by the decelerating effects of the adjacent zero-velocity outer walls, which nearly suppress the flow between the walls and the obstacle. For the general validity of our model, this effect can be neglected since it occurs only at

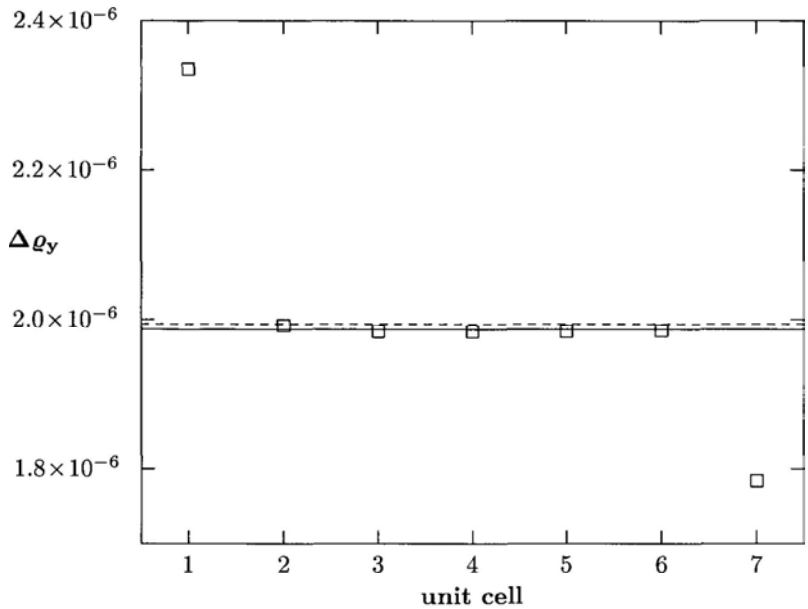

Figure 3.5: Long-time limit values of the density difference over different unit cells of the control array (red squares), with the applied adaptive difference $\Delta\rho_y$ (dashed blue line, between nodes 0 and 201) and the resulting periodic difference $\Delta\varrho_y$ (solid black line, between nodes 1 and 201) shown as horizontal lines.

the two outermost cells. This is demonstrated in Fig. 3.5, where the final density differences over all unit cells in the control array are shown. Except for the outermost cells, the density difference over all cells was within a 1%-interval of the adaptive density gradient.

However, these deviations over the outermost cells do not only occur in y-direction. In fact, the average density gradient in y-direction $\overline{\rho}(x = 0) - \overline{\rho}(x = 201)$, when averaged over the topmost ($1200 < y \leq 1400$) or bottommost ($0 < y \leq 200$) cells, is lower than the applied mean gradient $\rho_{\mathrm{L}} - \rho_{\mathrm{R}}$. This leads to a small numeric issue. Because the mean density difference is defined

over the entire array of unit cells the mean gradient over the inner cells in return is slightly larger than the overall mean gradient However, this overall mean gradient is identical to the gradient over the AGPBC system The x-density gradients of the AGPBC system and the control system hence differ slightly

$$\frac{\Delta\rho_x^{\mathrm{AGPBC}} - \Delta\rho_x^{\mathrm{ctrl}}}{\Delta\rho_x^{\mathrm{AGPBC}}} \approx 10^{-4} \tag{3 10}$$

To see the importance of this difference, let us look at the final state results of the AGPBC system and a system that uses GPBC in x-direction but only SPBC in y-direction Figure 3 6 shows velocity isolines $|\mathbf{v}|$ for AGPBC (panel A) and GPBC/SPBC (panel B), both in comparison with the control system While the AGPBC system agrees with the control system to a degree that distinguishing the contours becomes impossible deviations are clearly visible for the GPBC/SPBC system, where they are of an order of magnitude comparable to that of the flow

To quantify these differences, we define the relative error in the flow as

$$\epsilon = \sqrt{\frac{(\mathbf{v}_{\mathrm{ctrl}} - \mathbf{v})^2}{\overline{\mathbf{v}_{\mathrm{ctrl}}}^2}} \,, \tag{3 11}$$

where $|\overline{\mathbf{v}_{\mathrm{ctrl}}}|$ is the mean absolute velocity in the control system Fig 3 7 shows the such defined errors for the AGPBC system[2] Fig 3 7(A) shows the errors as computed directly from the AGPBC system The errors observed are of order $\epsilon \approx 10^{-4}$ However, a comparison between the errors observed and the velocity profile (Fig 3 6(A)) indicates that they are directly proportional Given our definitions, a proportionality in the velocities i e , $\mathbf{v}_{\mathrm{AGPBC}} = c \times \mathbf{v}_{\mathrm{ctrl}}$, would result in an error proportional to the current velocity $\epsilon = |(1 -$

[2]The errors for the SPBC/GPBC system is of order 10^{-1} clearly exceeding those of the AGPBC system and therefore irrelevant to the discussion here

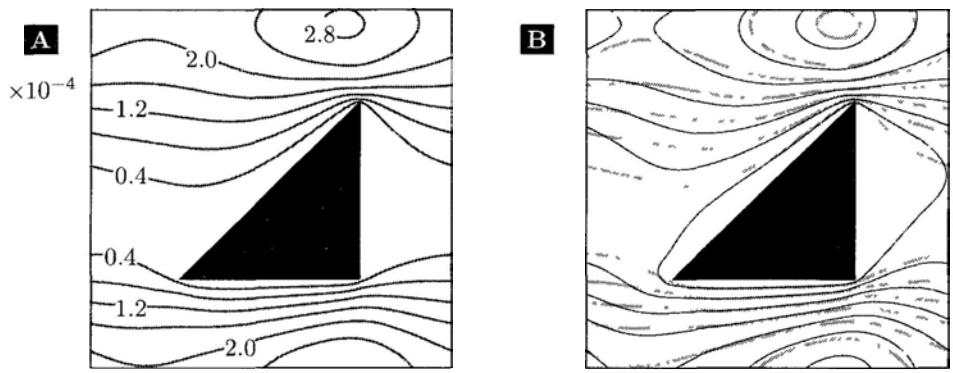

Figure 3.6: Flow isolines ($|\mathbf{v}|$) of the control system (thick gray lines) and the single cells (thin black lines) for AGPBC (A) and simple GPBC (B). Velocity isolines are spaced $4 \times 10^{-5} \delta x / \delta t$

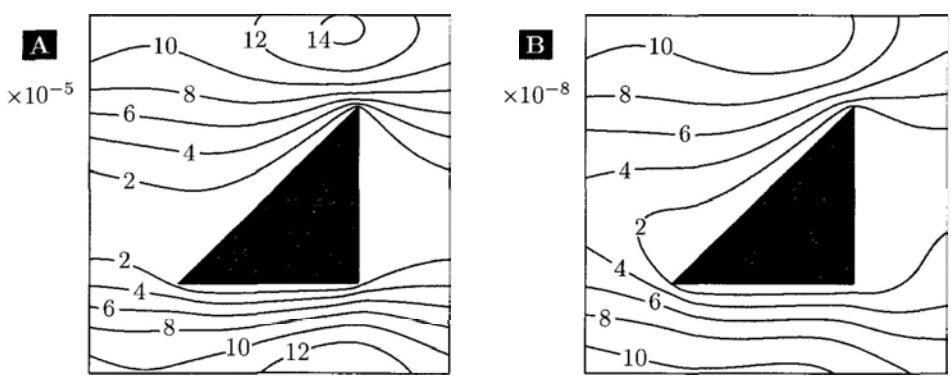

Figure 3.7: Relative deviations ϵ between the control system and the adaptive system with original $\Delta\rho_x$ (A) and with the control system's effective $\Delta\rho_x$ (B).

$c)\mathbf{v}_{\text{ctrl}}|/|\overline{\mathbf{v}_{\text{ctrl}}}|$. Furthermore, the observed error is also of the same magnitude as the measured deviation in the effective density gradient. This makes it plausible that the error observed actually is caused by the difference in the effective density gradient (see Eq. (3.10)).

To test this hypothesis, we simulate an AGPBC system, using the measured effective density gradient in x-direction. The resulting errors are shown in figure 3.7(B). The observed error has dropped by four orders of magnitude, showing clearly that the initially observed error was caused by the mismatch in the applied density gradient. However, since the simulated system is within the Stokes regime, this error affects only the flow velocity, but not the flow pattern. In fact, the error could have been reduced in the same extent by simply rescaling the flow field by the ratio of the applied density gradients. Finally, it should be stressed that the observed mismatch in the effective density gradients is a finite size effect intrinsic to our control system, which for computational purposes had to be of limited size. For systems with larger numbers of rows of obstacles as our method intends to help simulate, this mismatch would gradually diminish.

Figure 3.8 shows the long term evolution of the control and actuating variables. Figure 3.8(A) shows the net flow through the lower boundary of the control system, as well as the convergence of the vertical density difference over the control system against its long time value. Both quantities show an oscillatory exponential decay of the form $\exp(-\lambda t)\sin(\omega t + \phi)$ with a time constant of approximately $\lambda \approx 1/(12,000\delta t)$. Figure 3.8(B) shows the absolute y-momentum $|j_y^{\text{tot}}|$ and its asymptotic absolute actuating variable $\Delta\rho_y^{\text{asymp}} = |\Delta\rho_y(t) - \Delta\rho_y(\infty)|$. Figure 3.8(C) shows the absolute leakage $|\Phi_y|$ through the cell boundaries and the absolute asymptotic actuating variable $\rho_{\text{B}}^{\text{asymp}} = |\rho_{\text{B}}(t) - \rho_{\text{B}}(\infty)|$. Apart from a very short time directly after the

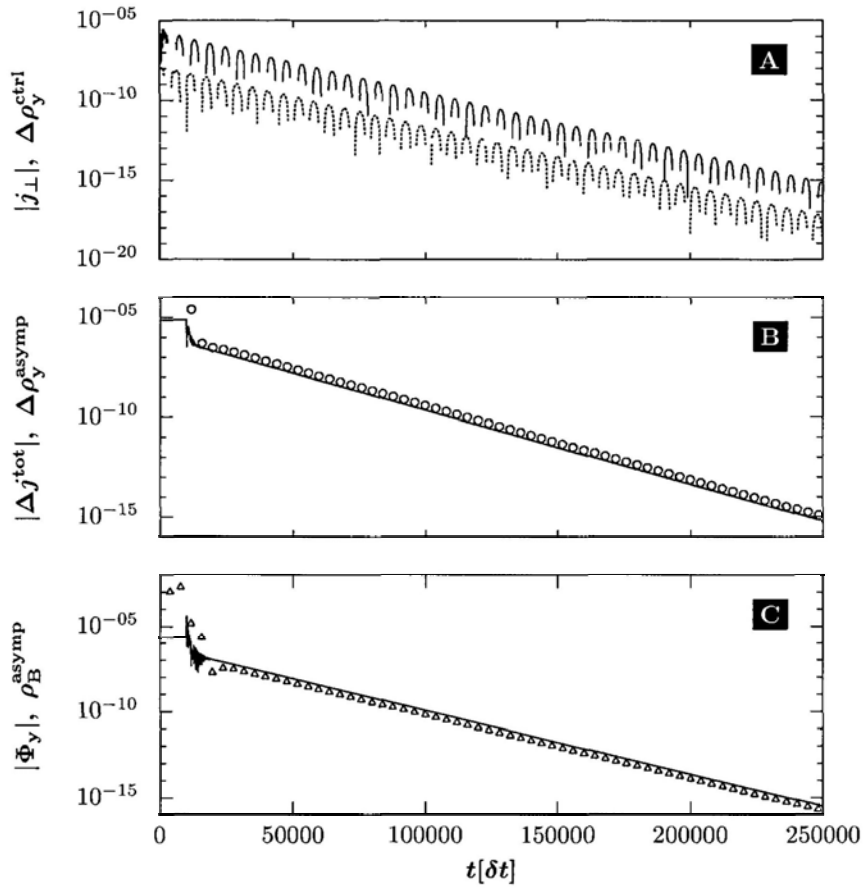

Figure 3.8: (A): Decay of the net flow $j_\perp^{\mathrm{ctrl}}(y = 600\delta x)$ through a horizontal boundary (red line) and of the corresponding asymptotic density difference $\Delta\rho_y^{\mathrm{ctrl}} = \Delta\rho_y^{\mathrm{ctrl}}(t) - \Delta\rho_y^{\mathrm{ctrl}}(\infty)$ measured over the control cell, i.e., between lines $y = 600$ and $y = 800$ of the array (blue dotted line). Since the quantities decay oscillatorily, the absolute value was taken and hence only the positive parts are displayed. (B): Relaxation of absolute total y-momentum $|j_y^{\mathrm{tot}}|$ (red circles) and controlling density difference $\Delta\rho_y^{\mathrm{asymp}} = |\Delta\rho_y(t) - \Delta\rho_y(\infty)|$ (blue line) in the AGPBC system. (C): Relaxation of absolute leakage $|\Phi_y|$ (red triangles) and the controlling average bottom density $\rho_{\mathrm{B}}^{\mathrm{asymp}} = |\rho_{\mathrm{B}}(t) - \rho_{\mathrm{B}}(\infty)|$ (blue line) in the AGPBC system.

initialisation period t^{init}, all quantities decay exponentially though not oscillatory The decay constant is virtually identical to that of the control system, showing that with a proper choice of control coefficients, a fully developed flow can be simulated within the same number of simulation steps

For implementation purposes an important point should be noted In the presented case the horizontal momentum j_x is monotonously increasing during the long time evolution of the flow Just as well the required gradient in y-direction increases until it has reached its long-time limit If the control coefficients are not suitably chosen, particularly if the initialisation period is too long, the flow might adapt itself into a direction where the obstacle offers less resistance Once the adaptive gradient is applied the flow is forced into a less favourable direction and will decrease by passing momentum to the solid obstacle Since the reaction of a flow to a density gradient is much faster than the reaction to an obstacle this type of long time decay will occur with a much smaller decay constant ($\lambda \approx 1/(60,000\delta t)$ was observed for the system discussed here) However a suitable choice of controlling quantities as well as a possible gradual onset of the driving density gradient can avoid such effects [38]

3.3 Summary and Conclusion

We introduced a new boundary condition algorithm for the treatment of solid outer walls in a repetitive geometry The method allows to reduce a two-dimensional repetitive array to a single unit cell and therefore significantly reduces the computational expense required for the simulation of such a system For the Stokes regime of laminar flows, our method offers excellent accuracy, without requiring more simulation time steps than a simulation of

the entire setup Hence, microfluidic devices, which use various forms of unit cell layouts, can be efficiently simulated using the lattice-Boltzmann method In particular, the calculation of flows in microfluidic devices with large numbers of unit cells benefits from our proposed boundary condition A good example for such a device is the deterministic lateral displacement array for continuous particle separation [39]

Part II

Pressure-Driven Vector Chromatography

Chapter 4

An Introduction to Brownian Ratchets

4.1 Motivation

The separation of large macromolecules is a crucial task in molecular biology, in particular with respect to proteins and DNA fragments. Such macromolecules can differ in size, drag, electrostatic charge, electrophoretic mobility, and other properties. However, existing separation techniques like gel electrophoresis are often slow and cumbersome, sometimes taking more than ten hours to separate large DNA coils [41].

Brownian ratchets, in form of microfluidic sieve devices, have received increasing attention as a particle separation mechanism based on a particle's diffusivity. Such ratchets require a driving force (see Sec. 4.2) to keep them outside thermal equilibrium. However, these driving forces each proved to have different downsides (see Sec. 4.4.2) Electric fields are influenced by the microscopic sieve barriers, inertia forces require a rotating mechanism and hence

make the realisation of a whole device 'on a chip' impossible, and gravitation cannot be tuned, which is unfortunate also for entirely different reasons. In what follows, we will discuss the general ratchet mechanism, as well as why and how it can be used for particle separation. In Ch. 5, we will propose a mechanism that uses pressure-driven flows as a driving mechanism for particle separation. This mechanism circumvents the aforementioned problems and could facilitate the realisation of chip-sized microfluidic particle separators.

4.2 The On-Off Ratchet

Being able to turn thermal noise into useful work is an idea so desirable that many people have tried to come up with thought-experiments that would make a realisation possible. Unfortunately, generating work from a closed system in thermal equilibrium is impossible according to the second law of thermodynamics. One of the most famous such experiments is the ratchet-pawl mechanism, first discussed by Smoluchowski [42] and popularised by Richard Feynman [43, 44]. Both showed that, if both pawl and heat paddle have the same temperature, the system is in thermal equilibrium and thermal energy alone will not do any work. If, however, the temperature of the paddle exceeds that of the ratchet, then the ratchet can move forward, but at the system's free energy's expense [45].

Another approach is to apply a force that permanently keeps a system outside equilibrium. This method was widely discussed with respect to molecular transport in cells [46, 47, 48]. Ajdari and Prost [49] proposed a simple method, using an oscillatory potential to keep the system out of equilibrium and rectify its Brownian motion, the so-called on-off ratchet. This method was experimentally realised by Rousselet *et al.* [50].

Consider a small particle of radius r suspended in a liquid of temperature T and viscosity η. The motion of the particle is described by the Langevin equation

$$m\mathbf{x} = \mathbf{F}(\mathbf{x}, t) + \tilde{\mathbf{f}}(t) - \beta\mathbf{x} \tag{4.1}$$

The forces acting on the particle are comprised of an external force $\mathbf{F}$ caused by some potential Φ, a drag term $-\beta\mathbf{x}$, and a thermal noise term $\tilde{\mathbf{f}}$. The thermal fluctuations are supposed to be white noise, i.e., they have zero mean and are uncorrelated in time

$$\langle\tilde{\mathbf{f}}(t)\tilde{\mathbf{f}}(t')\rangle = 2k_BT\beta\delta(t - t') , \tag{4.2}$$

where the drag coefficient

$$\beta = 6\pi\eta r \tag{4.3}$$

is determined through the viscosity of the fluid and the size of the (spherical) particle.

The probability density of a particle undergoing such Brownian motion is described by the Fokker-Planck equation

$$\begin{aligned} \frac{\partial\mathcal{P}}{\partial t} &= -\nabla\ \mathbf{J}(\mathbf{x}, t) \\ \mathbf{J}(\mathbf{x}, t) &= \frac{D}{k_BT}\mathcal{P}(\mathbf{x}, t)\mathbf{F}(\mathbf{x}, t) - D\nabla\mathcal{P}(\mathbf{x}, t) \end{aligned} \tag{4.4}$$

with

$$D = \frac{k_BT}{6\pi\eta r} = \frac{k_BT}{\beta} \tag{4.5}$$

being the diffusion constant according to the Stokes-Einstein relation.

In the following, we will consider a one-dimensional problem, i.e., we assume the potential to be independent of two coordinates $\partial_y\Phi = \partial_z\Phi = 0$. Consider the following potential

$$\Phi(x,t) \;=\; \begin{cases} \Phi^{\text{on}}(x) & : \; 0 \le t \le \tau_1 \\ \Phi^{\text{off}}(x) = 0 & : \; \tau_1 \le t \le \tau_1 + \tau_2 \end{cases} , \tag{4.6}$$

which is cyclic with period $T = \tau_1 + \tau_2$.

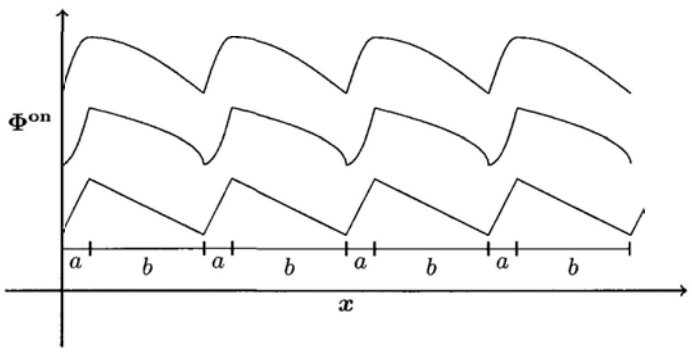

Figure 4.1: Possible choices of sawtooth-style potentials with identical asymmetry parameter.

The potential $\Phi^{\text{on}}(x)$ is a sawtooth-style potential with spatial period $L_x = a + b$. Examples of such potentials are depicted in Fig. 4.1. The exact shape of the sawtooth potential is not important for the time being. What does matter, however, is that the potential has an asymmetry, i.e., the distances a and b between the potential minimum and the adjacent maxima are different. We can quantify the asymmetry by defining an asymmetry parameter

$$\epsilon = \frac{a}{a+b} \; . \tag{4.7}$$

As a convention, we will label the length of the shorter edge as a. The asymmetry parameter is $\epsilon = 0.5$ for a symmetric potential, and $\epsilon = 0$ for a sawtooth potential with an orthogonal edge.[1]

[1]Unfortunately, this means that the asymmetry parameter is decreasing when the potential is more asymmetric. Attention should therefore be paid to the exact formulation

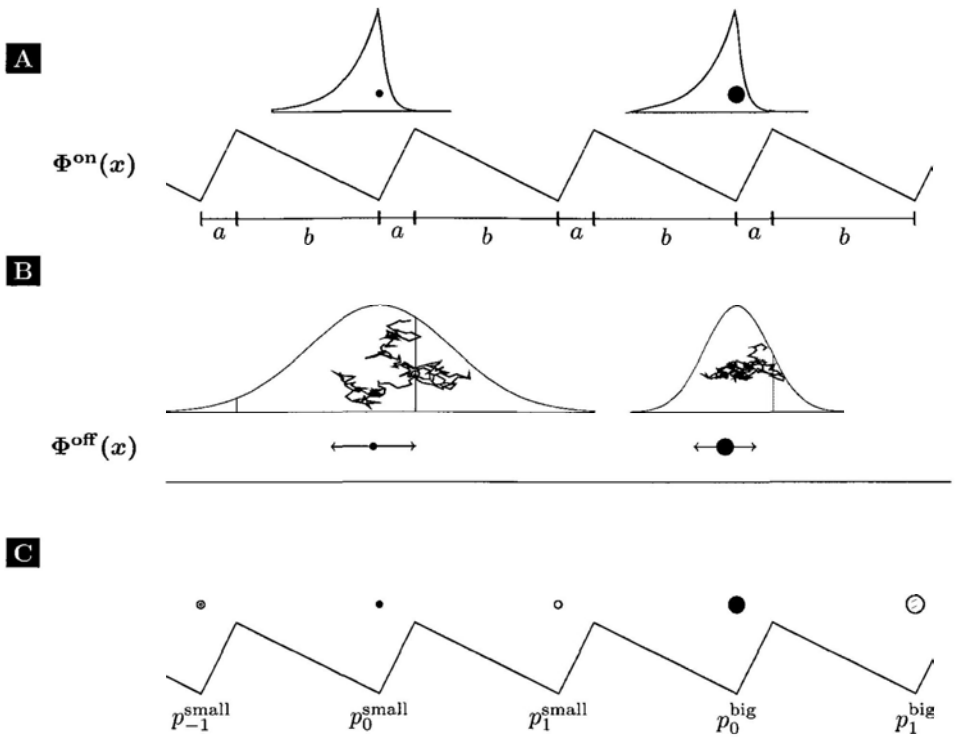

Figure 4.2: Particles in an on-off ratchet. (A) Particles are localised near the potential minimum at $t = \tau_1$. (B) While the sawtooth potential is switched off $\tau_1 < t < \tau_2$, the particles can diffuse freely. Their probability density function is a Gaussian bell curve whose width is determined by their diffusivity. (C) When the sawtooth potential is active again, the step probabilities p_n can be expressed in terms of the corresponding error functions.

Let us consider the effects of such a potential on the suspended particle. Figure 4.2(A) shows two particles of different sizes under the influence of such a potential, right before the potential is switched off. The interval τ_1 has been chosen such that the particles are now in their equilibrium state and are

used.

distributed according to the Boltzmann distribution

$$\mathcal{P}(x) = c \times \exp\left(-\frac{\Phi^{\mathrm{on}}(x)}{k_B T}\right) \tag{4 8}$$

Even for different particles like the ones shown here, the equilibrium distribution is identical as long as the potential does not depend on the particle's size or mass The resulting distribution has been drawn very broadly for illustrative purposes However, the potential can be chosen to be large against the thermal energy $\Phi^{\mathrm{on}} \gg k_B T$, such that the distribution becomes very narrow and the particle is effectively localised at the minimum x_0 We will in the following choose both the potential and the on-time interval τ_1 such that the particle is localised at a potential minimum when the potential is switched off

For $t > \tau_1$, the potential is switched off and the particles diffuse freely (see Fig 4 2(B)) If the particles were previously localised at $x = x_0$, their probability density is now given by a Gaussian distribution

$$\mathcal{P}(x,t) = \frac{1}{\sqrt{4\pi D(t-\tau_1)}} \exp\left(\frac{(x-x_0)^2}{4D(t-\tau_1)}\right) \tag{4 9}$$

The diffusion process does depend on the properties of the particles, as its diffusion constant is related to its radius through Eq (4 5) At time $t = \tau_1 + \tau_2$, the potential is switched on again, and the particles will drift to the local potential minimum If a particle has diffused to the right by more than a, or to the left by more than b, it will move to a different local minimum than the one occupied before More formally, we are interested in the probabilities that a particle will move n periods to the right[2] p_n We can express these probabilities in terms of the error function

$$\mathrm{erf}(x) = \frac{2}{\sqrt{\pi}} \int_0^x \exp(-x'^2)\mathrm{d}x' \tag{4 10}$$

[2]Movements to the left are characterised by negative n

The integral of an arbitrary Gaussian distribution is expressed in terms of the error function as

$$\int_u^w \frac{1}{\sigma\sqrt{\pi}} \exp\left(-\frac{(x-x_0)}{\sigma^2}\right) \mathrm{d}x = \frac{1}{2}\left(\mathrm{erf}\left(\frac{w-x_0}{\sigma}\right) - \mathrm{erf}\left(\frac{u-x_0}{\sigma}\right)\right) \tag{4.11}$$

Consequently, the step probabilities p_n to move by $n = 0, \pm 1$ minima are given as (see also Fig. 4.2(C))

$$\begin{aligned} p_{-1} &= \frac{1}{2}\left(\mathrm{erf}\left(\frac{-b}{\sqrt{4D\tau_2}}\right) - \mathrm{erf}\left(\frac{-2b-a}{\sqrt{4D\tau_2}}\right)\right) \\ p_0 &= \frac{1}{2}\left(\mathrm{erf}\left(\frac{a}{\sqrt{4D\tau_2}}\right) - \mathrm{erf}\left(\frac{-b}{\sqrt{4D\tau_2}}\right)\right) \\ p_{+1} &= \frac{1}{2}\left(\mathrm{erf}\left(\frac{2a+b}{\sqrt{4D\tau_2}}\right) - \mathrm{erf}\left(\frac{a}{\sqrt{4D\tau_2}}\right)\right) , \end{aligned} \tag{4.12}$$

and arbitrarily by n potential minima

$$\begin{aligned} p_n &= \frac{1}{2}\left(\mathrm{erf}\left(\frac{(n+1)a+nb}{\sqrt{4D\tau_2}}\right) - \mathrm{erf}\left(\frac{na+(n-1)b}{\sqrt{4D\tau_2}}\right)\right) \\ &= \frac{1}{2}\left(\mathrm{erf}\left(\frac{L_x(n+\epsilon)}{\sqrt{4D\tau_2}}\right) - \mathrm{erf}\left(\frac{L_x(n-1+\epsilon)}{\sqrt{4D\tau_2}}\right)\right) \end{aligned} \tag{4.13}$$

We can combine all system parameters into one dimensionless variable called the particle's relative diffusivity

$$\mathcal{D} = \frac{D\tau_2}{L_x^2} , \tag{4.14}$$

which expresses the diffusion constant in terms of the system's characteristic length and time. By doing so, we can express the step probabilities as a function of $\mathcal{D}$ and ϵ

$$p_n = \frac{1}{2}\left(\mathrm{erf}\left(\frac{n+\epsilon}{\sqrt{4\mathcal{D}}}\right) - \mathrm{erf}\left(\frac{n-1+\epsilon}{\sqrt{4\mathcal{D}}}\right)\right)$$

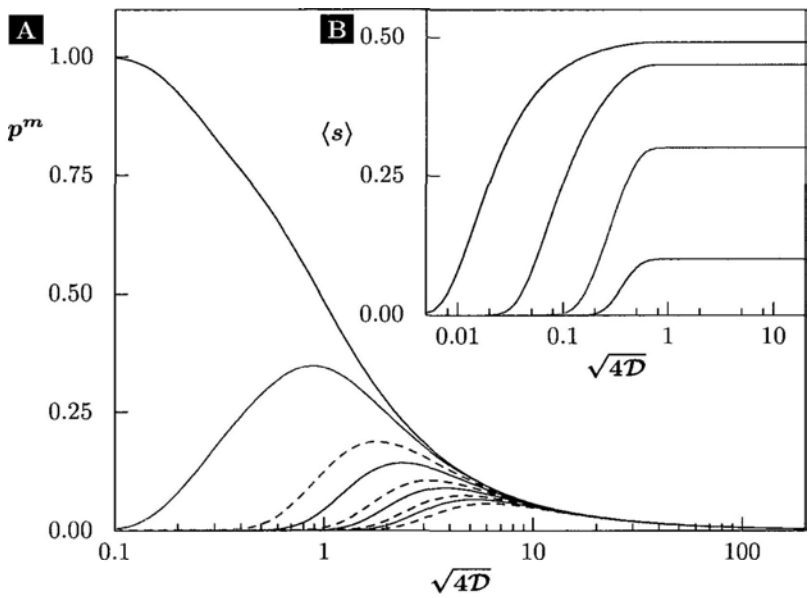

Figure 4.3: (A) Step probabilities p_n for a system with $\epsilon = 0.2$ as a function of the standard deviation of the diffusion process $\sigma_D = \sqrt{4\mathcal{D}}$. The probabilities are drawn for a displacement by $n = 0$ (green), $n = \pm 1$ (orange), $n = \pm 2$ (blue), $n = \pm 3$ (red) and $n = \pm 4$ (purple) steps. Solid lines refer to positive, dashed lines to negative movement. The inset shows the mean number of steps $\langle s \rangle = \langle x \rangle / L_x$ for systems with asymmetries $\epsilon = 0.01$(red), $\epsilon = 0.05$(blue), $\epsilon = 0.2$ (orange) and $\epsilon = 0.4$ (green). Both figures are drawn on a logarithmic scale for $\sqrt{\mathcal{D}}$

The step probabilities are shown in Fig. 4.3(A). For very small values of $\mathcal{D}$, particles remain in their original potential minimum. For larger values of $\mathcal{D}$, particles start to diffuse over the nearest barrier and hence experience a net displacement to the right. For even larger values of $\mathcal{D}$, backwards step probabilities and higher probabilities also become relevant. The mean number of steps of a particle during one cycle is shown in the inset Fig. 4.3(B). For very small diffusivities, no displacement occurs, and the maximum displacement is reached for values of $\sqrt{4\mathcal{D}} \leq 1$. The slope of $\langle s \rangle(\sqrt{4\mathcal{D}})$ represents the resolving ability of the setup. Systems with larger asymmetry have larger $\partial\langle s \rangle/\partial\mathcal{D}$, and offer therefore better resolution. If the system is used for spatial separation, i.e., separating particles by size rather than just into two categories *larger than* r_0 and *smaller than* r_0, $\sqrt{4\mathcal{D}} \ll 1$ is required, and hence all step probabilities other than p_1 and p_0 can be neglected.

For a given ϵ, the mean displacement $\langle s \rangle$ converges against a constant values $\langle s \rangle_{\max} = \frac{1}{2} - \epsilon$. This behaviour can be understood as follows [51]. For one cycle, the mean displacement is given as

$$\begin{aligned} \langle s \rangle &= \sum_{n=-\infty}^{\infty} n p_n = \sum_{n=-\infty}^{\infty} n \frac{1}{2} \left(\operatorname{erf}\left(\frac{n+\epsilon}{\sqrt{4\mathcal{D}}} \right) - \operatorname{erf}\left(\frac{n-1+\epsilon}{\sqrt{4\mathcal{D}}} \right) \right) \\ &= -\frac{1}{2} \sum_{n=-\infty}^{\infty} \operatorname{erf}\left(\frac{n+\epsilon}{\sqrt{4\mathcal{D}}} \right) . \end{aligned} \tag{4.15}$$

The derivative of the mean number of steps with respect to the asymmetry is

$$\frac{\partial\langle s \rangle}{\partial\epsilon} = -\frac{1}{\sqrt{4\pi\mathcal{D}}} \sum_{n=-\infty}^{\infty} \exp\left(\frac{(n+\epsilon)^2}{4\mathcal{D}} \right) . \tag{4.16}$$

In the limit of $\mathcal{D} \to \infty$, the right side becomes the Riemann integral of the Gauss curve,

$$\begin{aligned}
\lim_{\mathcal{D}\to\infty} \frac{\partial\langle s\rangle}{\partial\epsilon} &= -\lim_{\mathcal{D}\to\infty} \frac{1}{\sqrt{4\pi\mathcal{D}}} \sum_{n=-\infty}^{\infty} \exp\left(\frac{(n+\epsilon)^2}{4\mathcal{D}}\right) \\
&= -\frac{1}{\sqrt{\pi}} \int_{-\infty}^{\infty} \exp\left(-x^2\right) \mathrm{d}x - -1 \\
\Rightarrow \lim_{\mathcal{D}\to\infty} \langle s\rangle(\epsilon) &= c - \epsilon \qquad (4.17)
\end{aligned}$$

Since we know that no displacement occurs for symmetric ratchets, i.e., $\langle s\rangle(\epsilon = 1/2) = 0$ we can conclude that $\langle s\rangle_{\max} = 1/2 - \epsilon$

According to the central limit theorem, the distribution after m repetitions of the cycles follows a Gaussian distribution with mean and variance given by[3]

$$\begin{aligned}
\langle s\rangle_m &= m\langle s\rangle \\
\langle (s - \langle s\rangle)^2\rangle_m &= m\langle (s - \langle s\rangle)^2\rangle \qquad (4.18)
\end{aligned}$$

4.3 Existing Methods for DNA Fragment Separation

Separation of large biomolecules such as DNA coils and proteins is a crucial task required in a plethora of biochemical investigation methods. Unfortunately, working methods of DNA strain separation by length are rather cumbersome as they cannot be automated and involve many manual steps. When freely dispersed in a fluid and subjected to an electric field, a particle experiences an electrostatic force $\mathbf{F}_E = q\mathbf{E}$. While moving through the fluid, it will also experience a drag force $\mathbf{F}_d$. For spherical particles of radius r, this force can be written as $\mathbf{F}_d = -6\pi r\eta\mathbf{v}$ where η is the fluid's dynamic

[3] For a finite number m of repetitions, the distribution is given by a binomial distribution with mean mp. However, for large m the binomial distribution becomes simply an integer version of the Gaussian distribution.

viscosity At velocity $\mathbf{v}_0$ these forces balance and we can define the particle's electrophoretic mobility as

$$\mu_0 = \frac{v_0}{E} = \frac{q}{6\pi\eta r} \tag{4 19}$$

However, the charge q of a DNA coil is typically also proportional or nearly proportional to its radius of gyration [52] DNA fragments of different length thus tend to travel at the same speed In order to separate DNA fragments of different size the coils are dispersed in a gel matrix that functions as a microscopic sieve Depending on the pore size of the gel, the mobility's dependence on r changes, and shorter DNA strains travel faster After a certain time of electrophoresis, DNA strains of different size have travelled different distances and are located at distinct positions in the matrix However, retrieving the DNA fragments from the matrix is a cumbersome task, and the method is therefore only of limited use if the DNA is to be processed further

4.4 Particle Separation Using Brownian Ratchets

4.4.1 Proposed Ratchet-Based Particle Separation Devices

The use of ratchet-based particle separation devices could provide a remedy to most of the aforementioned problems Microfluidic systems that are able to fully automate chemical or biological tasks have become known as *lab-on-a chip* devices Exploiting the ratchet effect for particle separation was first proposed by Ertaş and, independently by Duke and Austin The proposed designs were published in the same issue of Physical Review Letters [53, 54]

and differ mainly in the exact design of the microscopic sieve. Figure 4.4 shows such an microfluidic sieve design. It features all essential mechanisms proposed in Refs. [53, 54]. Some changes in the exact geometry were made for the purpose of easier comparison with the designs used in Ch. 5. The basic mechanism is as follows. Particles are electrophoretically driven through an array of obstacles. They are able to diffuse freely between two rows of obstacles, corresponding to the ratchet potential being switched off. The obstacles then serve to localise the particles inside the gap between two obstacles, corresponding to the ratchet potential being switched on. For a suitable asymmetric obstacle design, this will induce a net drift of the particles orthogonal to the direction of the electrophoretic force. The average perpendicular displacement will be dependant on the diffusivity of the particle, and particles of different diffusivity will therefore travel at different angles.

The effects of such a unit cell can be discussed quantitatively. One unit cell has the dimensions $L_x \times L_y$. Particles of different sizes are dispersed in a fluid and driven by an electrophoretic force $\mathbf{F}_E$, and hence travel horizontally at uniform velocity v_x. The fluid itself is macroscopically inert. After passing through a line of obstacles $x = 0$, the particles are localised at the obstacle gap. In the ratchet model, this corresponds to a ratchet potential that has been active for some time and is just about to be switched off, i.e., $t = \tau_1$. Hereafter, the particles drift towards the next row of obstacles, but are free to diffuse in y-direction. Without diffusion, the particles would drift straight through the gap in the next row of obstacles. Through diffusion, a particle may have moved above the line y_+, in which case it will be moved towards the upper gap, and hence be displaced by L_y. Particles that diffused below y_- will be displaced by $-L_y$. Speaking in terms of the ratchet model, this corresponds

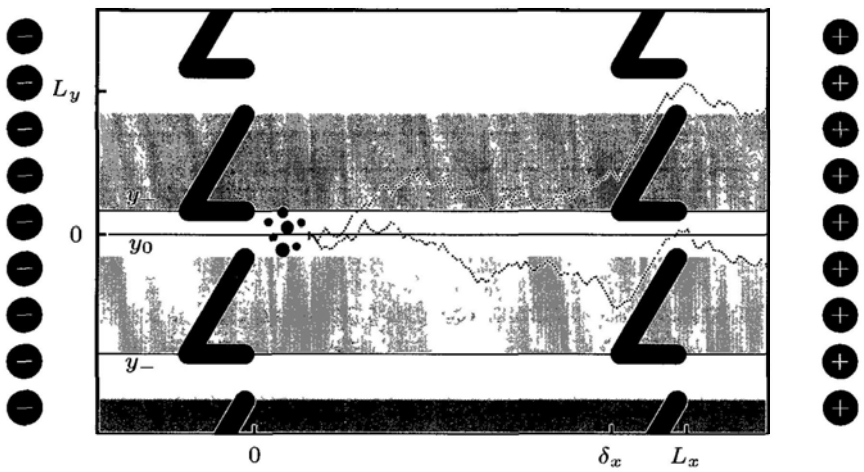

Figure 4.4: Design of a particle separator based on the ratchet effect. Particles are driven by a electrophoretic force. At each gap $x = n \times L_x$, particles are localised at y_0. In the range $0 < x < \delta x$, the particles can diffuse freely in y-direction. At $x = \delta x$, the gap through which the particle will pass is decided: the particles that diffused above y_+ will be displaced by L_y, while those that diffused below y_- will be displaced by $-L_y$.

to a diffusion time $\tau_2 = \delta_x / v_x$, and a potential with asymmetry

$$\epsilon = \frac{y_+}{L_y} \,. \tag{4.20}$$

If $y_+ - y_0 < y_0 - y_-$, then the system is asymmetric with $\epsilon < 1/2$, and particles will experience an upward displacement. Since the separation occurs orthogonally to the direction of the electric field, this process is also referred to as *vector chromatography.*

4.4.2 Realisations of Ratchet-Based Separation Devices

Realisations of ratchet-based particle separation devices were attempted shortly after the mechanisms were proposed. Chou *et al.* reported a successful separation of DNA coils that differed by less than 6% in diameter, using a 10cm micro-fabricated sieve device [55]. The observed diffusion paths, in particular the angular deflection, differed significantly from theory's predictions. In particular, the step probability p_1 was found to exceed theoretical expectations significantly, and finite hopping probabilities $p_{n=1} > 0$ were observed even for very high drift velocities v_x that minimised the free diffusion time τ_2.

Several factors can contribute to such deviations. For one, the obstacles act on the particles slightly differently than a ratchet potential would. This problem is illustrated in Fig. 4.5(A). The vertical gap between two obstacles has to be wide enough to allow the largest particles to pass. These particles will then be located perfectly in the middle of the gap. Smaller particles, however, do not feel a potential over the entire range of the gap, but instead can diffuse freely in some range centred around the midpoint of the gap. This means that the particle distribution will be localised in the middle of the gap only for large particles. Smaller particles will have a tilted distribution. When

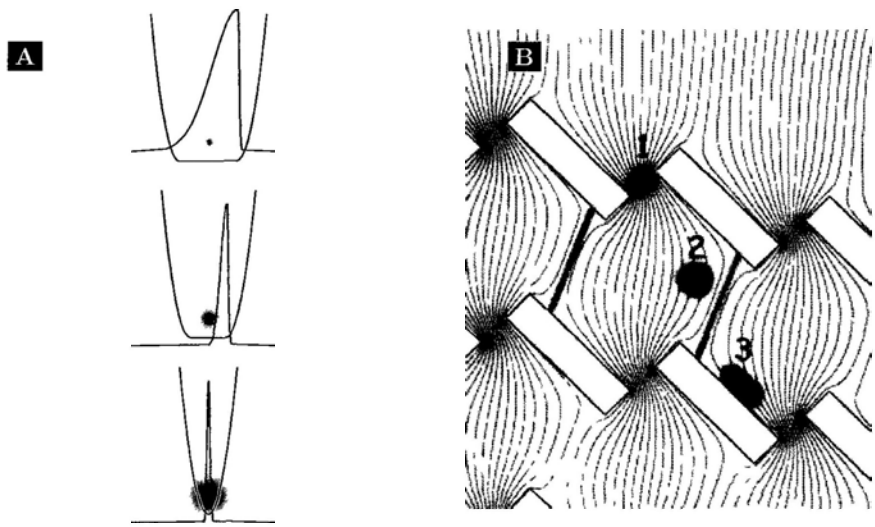

Figure 4.5: Issues in the realisation of particle separation devices. (A) Dislocation due to a particle-size dependent effective potential. Black lines illustrate the effective potential for different sized particles at the gap. Red lines illustrate the resulting distribution inside the gap. (B) Electric field lines in a different separation device, reproduced from [56] (with permission from Springer Science & Business Media).

they approach the obstacle from anywhere but directly above the gap, they will be guided along the obstacle's inclined flank and hence in this example, reach the gap at its right end

Another problem is that the electrostatic force inside the obstacle array is distorted by the obstacles Fig 4 5(B) shows the movement of one particle inside a different type of obstacle array, together with the calculated electric field [56] Indeed, a large part of the horizontal movement here is caused by the field lines fanning out behind the gaps, rather than the particle diffusing This process obfuscates the ratchet effect since small particles following the field lines will be guided around the obstacles and will hence not experience a ratchet potential at all

The latter problem was discussed by Li and Drazer [57], who performed a quantitative analysis of the diffusion of particles through an array of obstacles akin to the one proposed by Duke and Austin [54] They argued that the electric field cannot penetrate the electric double layer that forms around such obstacles, and showed that such non-permeating fields cannot be used for ratchet-based vector chromatography Instead, they proposed the use of permeating force fields such as inertial or gravitational forces, and calculated the migration angle as a function of the particle's diffusivity They furthermore stated that laminar flow fields can not be used for vector chromatography, since the dispersed particles would again be guided around the obstacles and not experience a ratchet potential

4.5 Conclusion

We discussed the mechanisms of a Brownian on-off ratchet and analysed how a particle is displaced inside such a ratchet, depending on the ratchet's dimensions. its asymmetry, its diffusion time interval, and the particle's diffusion constant. We showed how this displacement can be expressed in terms of the dimensionless diffusivity and the ratchet's asymmetry only, and finally introduced and discussed a design that exploits the ratchet effect to separate particles depending on their diffusion constant. In the following chapter, we will show how this design can be modified to use a pressure-driven flow, rather than electrostatic forces, as the driving force of a Brownian ratchet.

Chapter 5

Creating Asymmetry in Brownian Ratchets Using Pressure-Driven Flows

5.1 Motivation

Pressure-driven flows were originally not considered as driving forces for ratchet-based particle separators. This is because the flow fields circumvent all obstacles and interactions between obstacles and particles are hence limited to finite-size effects, which are for example used in deterministic lateral displacement methods [39, 58]. Nonetheless, pressure driven flows offer interesting properties that make them particularly well suited as driving forces of a ratchet-based particle separator. If diffusion is neglected, the movement of the dispersed particle is the same as the movement of the fluid, at least for flows as slow as those that we consider ($v \approx 1\mu m/s$). Hence, neither fluctuations in the electrophoretic force, e.g., due to fluctuations in the double layer, or

fluctuations in the drag force, e g , due to varying shapes of the particles, can alter the result Furthermore, flow fields can easily and reliably be calculated once the kinematic viscosity of the fluid and the geometry of the system is known Electric fields, meanwhile, depend on a variety of parameters that involve the material that the obstacles are made of, the ion density in the fluid and the electrostatic properties of the particle Practically, the only problem is that particles dispersed in a laminar flow do not feel any force orthogonal to any obstacle's surface in this flow Under the no-slip assumption, the fluid molecules in direct contact with the obstacle's surface are inert, and the flow in the next layer is tangential to the obstacle s surface In this chapter, we will show that by using perforated obstacles ratchet-based particle separation can be achieved using pressure-driven flows as the driving force

5.2 Geometry Design

Figure 5 1 illustrates the problem generally experienced with non-permeating fields A pressure difference in x-direction drives a flow through an array of unit cells of dimension $L_x \times L_y$ At its upper and lower ends, the array is enclosed by solid walls, such that the entire device resembles Fig 1 1 in Ch 1 The flow field was calculated using a lattice-Boltzmann simulation, with adaptive generalised periodic boundary conditions as discussed in Sec 3 1

Lets us consider a particle of diameter δ_y, which exactly fits into the gap between the obstacles It hence passes exactly in the middle of the gap and, without diffusing, will follow the flow line marked as y_0 In order to move through the upper or lower gap it has to diffuse beyond the lines y_+ or y_- into the streams S_+ or S_-, respectively Even though the obstacle itself is asymmetric, the resulting flow itself is not both y_- and y_+ are, one average,

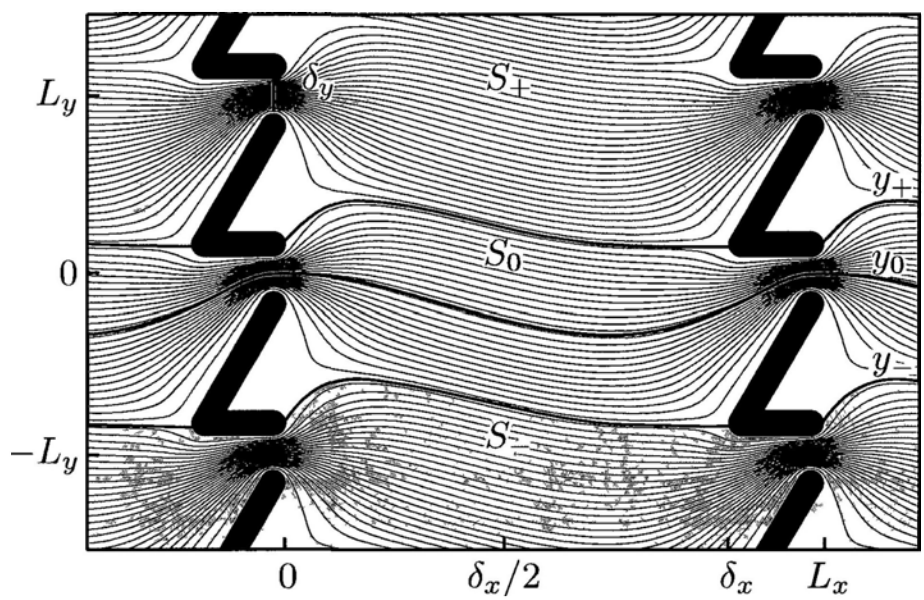

Figure 5.1: Pressure-driven flow field using a solid obstacle design. Flows passing through different gaps are shown in different colour. Figure design courtesy of A. Grimm.

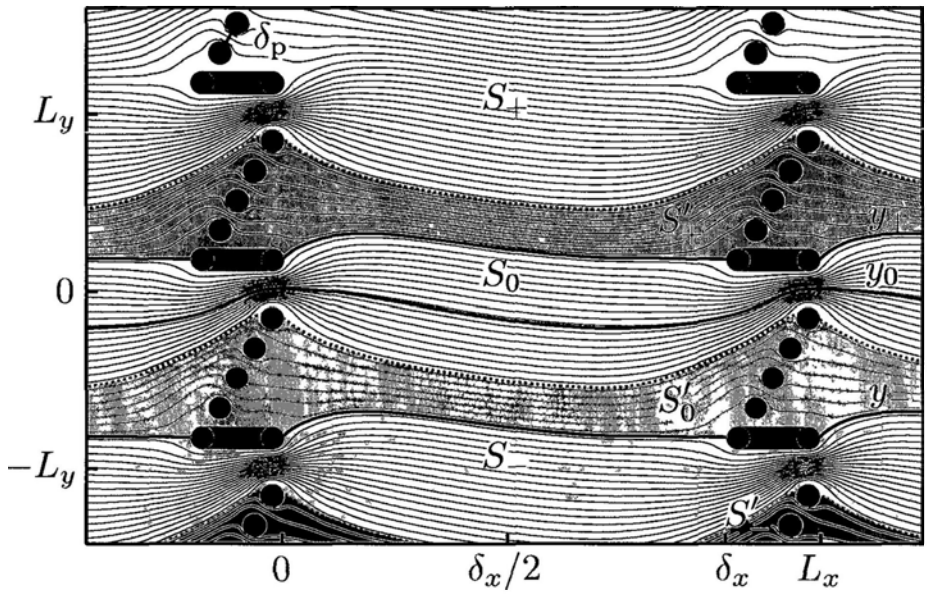

Figure 5.2: Flow field for an obstacle design with permeable upper flank. Flows passing through different gaps are shown in different colour. The parts of the flow in which particles are deflected are highlighted in the same colour. Figure design courtesy of A. Grimm.

the same distance apart from its original position at[1] y_0. In terms of the ratchet model, this means $a = b$,

$$\epsilon = \frac{y_+ - y_0}{L_y} = \frac{1}{2} \,, \tag{5.1}$$

and hence[2] $p_1 = p_{-1}$. Without creating an asymmetric flow profile, particle separation is impossible.

[1]This argument is more for illustrative purposes, since layouts can be created where this is quite clearly not fulfilled anymore. However, the probability to diffuse from y_0 to y_+ in one cycle is equal to the probability to diffuse from y_+ to y_0 in the next cycle. This is not the case in a ratchet, where diffusing the distance a causes a much larger displacement of $a + b$.

[2]The distance between the flow lines was measured at $x = \delta x/2$

Figure 5.2 shows the flow field for an obstacle design with a permeable upper flank. The upper flank is made up of circular pillars, with a pillar gap spacing of δ_p. Particles with a diameter larger than δ_p are sterically excluded from passing through these gaps. If such a particle enters one of the highlighted flows S', it will be deflected upwards. As a certain part of the flow passes through the upper flank of the obstacle, the resulting flow pattern is asymmetric: $y_+ - y_0 < y_0 - y_-$. Ratchet-based particle separation is now possible for particles with diameter $\delta_p < 2r < \delta_y$. The task of creating a design that is suitable for a wide range of particle sizes, i.e., $\delta_p \ll \delta_y$, and at the same time offers sufficient asymmetry is difficult. In fact, every decrease of δ_p or increase of δ_y reduces the portion of the flow through the upper flank of the obstacle, and hence decreases the asymmetry.

Figure 5.3 shows flow fields for different gap-width-to-inter-pillar-width ratios (Fig.5.3 (A)), and the dependence of the resulting asymmetry on this ratio (Fig.5.3 (B)). For wide gap widths and thus large values of $\delta y/\delta p$, such as shown in the topmost example of Fig. 5.3(A), hardly any flow penetrates the obstacle and the asymmetry therefore is close to $\epsilon = 1/2$. For smaller ratios, this flow increases, and hence ϵ decreases. However, this decrease is very slow, and small values of ϵ are achieved only for ratios $\delta y/\delta p \approx 1$. The corresponding flow field is shown in the bottommost panel of Fig. 5.3(A). Here, the main gap has basically become another inter-pillar gap. Now, all particles that fit through the obstacle gap will also fit through the gap between two pillars, and the resulting situation is identical to having solid obstacles.

Interestingly, the asymmetry of the flow does not need to correspond directly to an asymmetry in the obstacle design. For example, if the lower flank of our obstacle design was permeable as well, the obstacle would still appear

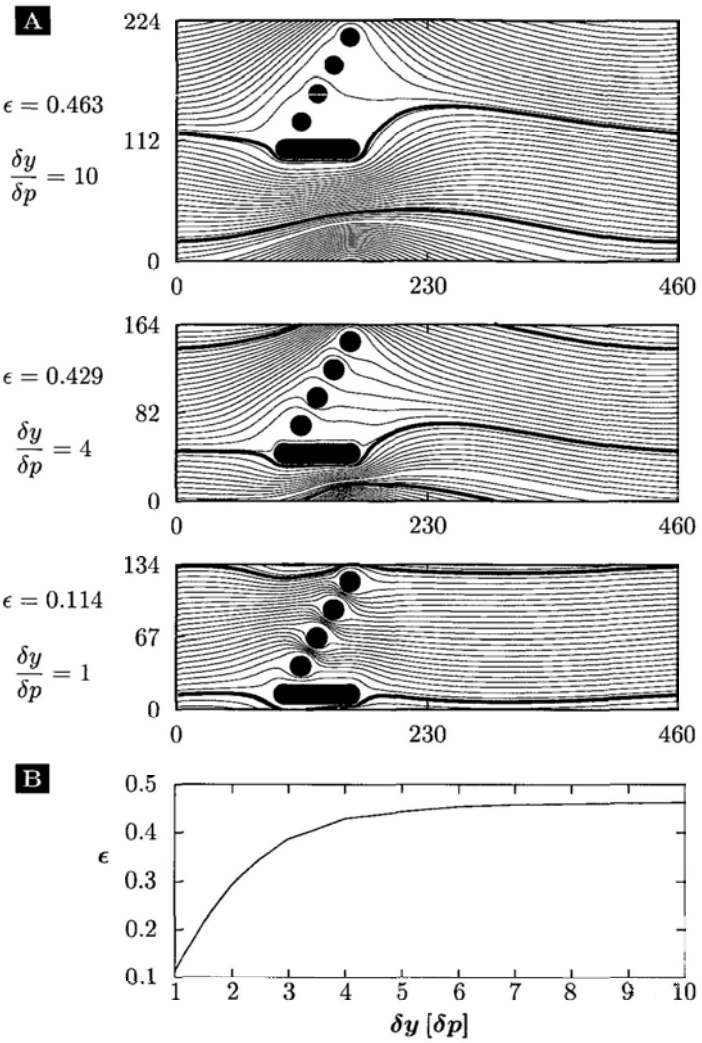

Figure 5.3: Asymmetry dependence on the gap width/inter-pillar width ratio. (A) Flow patterns for different ratios. Bold green and red lines indicate y_0 and y_+, respectively. The width of the red stream, as a fraction of L_y, is equivalent to ϵ. (B) Asymmetry ϵ as a function of the gap size between two adjacent obstacles δ_y, expressed in multiples of δ_p.

asymmetric, but the flow would become nearly perfectly symmetric. In return, we can extend the obstacle horizontally by extending the impermeable lower flank and adding a permeable horizontal extension to the upper flank, as shown in Fig. 5.4(A). This method turns out to be very effective, since the horizontally extended gap both causes additional flow through the upper flank as well as reduced flow through the obstacle gap, in the same manner as a Poisseuille flow is slowed down if the pipe through which it flows is extended.

Figure 5.4(B) shows the asymmetry as a function of the number of pillars in the elongated upper flank. For an obstacle gap width of $\delta_y = 3\delta_p$, the asymmetry coefficient is reduced by more than a factor four. A larger number of pillars can be used to a create large asymmetry for even larger obstacle gaps. A vertical extension of the upper flank by a small number of pillars can further increase asymmetry. However, many other parameters like the minimal structure size have an equally large influence in the realisation of such a device. We hence postpone a discussion of the optimal design for experimental realisation, and conclude here that permeable horizontal walls can tremendously increase the asymmetry of the flow.

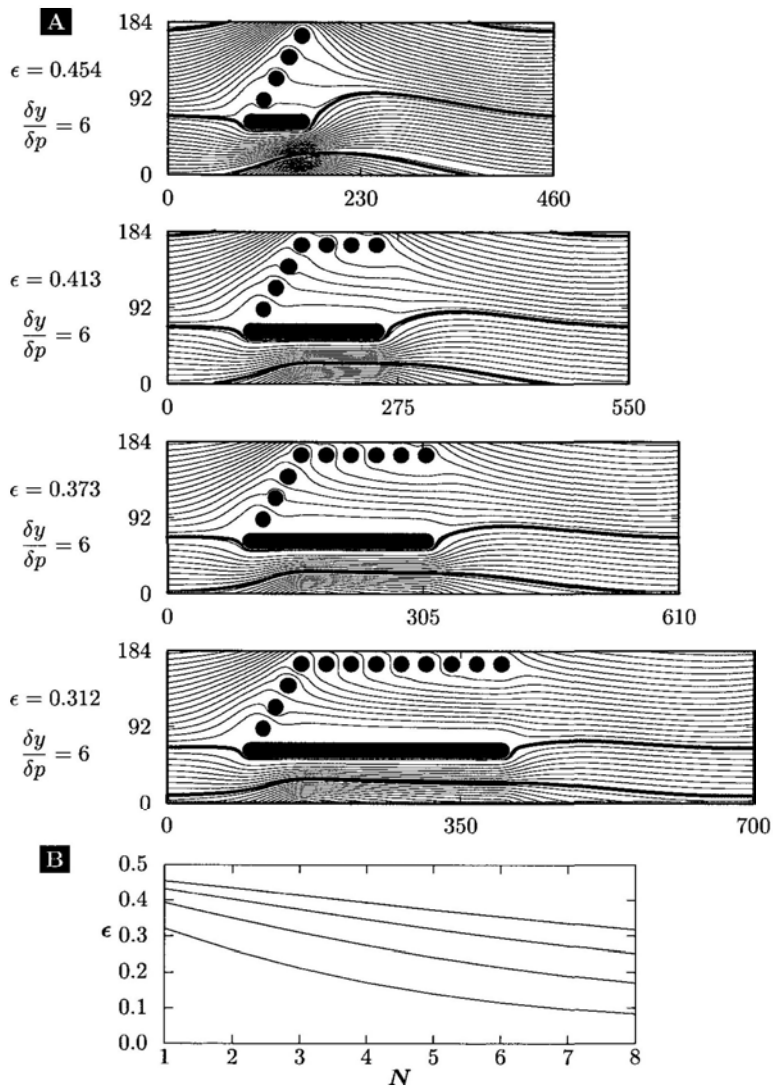

Figure 5.4: Asymmetry dependence on the number of pillars in the horizontally extended upper flank. (A) Flow fields for horizontal flanks with (top to bottom) zero, three, five and eight pillars. Bold green and red lines indicate y_0 and y_+, respectively. Again, the width of the red stream is equivalent to ϵ. (B) Flow asymmetry as a function of the number of pillars in the horizontal row, for obstacle gaps of $\delta_y = 3\delta_p$ (purple), $\delta_y = 4\delta_p$ (blue), $\delta_y = 5\delta_p$ (green) and $\delta_y = 6\delta_p$ (red).

5.3 Brownian Dynamics and Ratchet Theory

According to our previous analysis, our proposed device should function as a Brownian ratchet for particles with a diameter of $\delta_y \geq 2r \geq \delta_p$. In terms of ratchet theory, the time interval for diffusion is given by the time required to pass the distance between two rows of obstacles, i.e., $\tau_2 = \delta x / \overline{v_x}$. Flow velocity in this area is nearly uniform, since nothing obstructs the flow. Once the particle has moved to the range $\delta x \leq x \leq L_x$, the gap through which it will pass is determined. Hence, we ignore diffusion in this range.

We use a design as shown in Fig. 5.4 (A), but with a horizontal extension of $N = 8$ pillars and an obstacle gap size $\delta_y = 4\delta_p$, corresponding to an asymmetry of $\epsilon = 0.179$. We can adapt the dimensionless diffusivity to this layout and define

$$\mathcal{D} = \frac{\delta x D}{v_x L_y^2} \tag{5.2}$$

For a particle of given radius and hence diffusion constant, we can adjust its diffusivity over a wide range by adjusting the flow velocity accordingly. Particles in the range $\delta_p \leq 2r \leq \delta_y$ are expected to show a mean movement in y-direction akin to the displacement shown in Fig. 4.3(B). Larger particles will not pass through the obstacles, and particles with $2r < \delta_p$ are assumed to be not deflected at all [57].

To test these predictions, we performed Brownian dynamics simulations for spherical, pseudo hard-core particles dispersed in the discussed flow fields. The simulation of a finite-size particle in shear flow and in the presence of non-trivial boundary conditions is a complex problem, because the involved effects occur on a wide range of time-scales [59]. Since we are interested in particle trajectories through a large number of obstacles, it is impossible to fully resolve hydrodynamic effects, which happen on much shorter time scales

We therefore assume that the presence of a suspended particle does not alter the flow field In other words, the particles interact with the flow as if they were point-sized, but they possess the potential of a finite-sized particle for interaction with the obstacles

Under these assumptions, the two-dimensional trajectories $\mathbf{r}(t) = (x(t), y(t))$ of suspended particles are governed by the Langevin equation

$$\mathbf{r} = \mu\,[\mathbf{f}_{\rm obs}(\mathbf{r}) + \tilde{\mathbf{f}}(t)] + \mathbf{v}(\mathbf{r})\ , \tag{5 3}$$

where $\mu = v/F = 1/\beta$ is the mobility coefficient of the particle, akin to Eq (4 19) The components of the random force $\tilde{\mathbf{f}}(t)$ are unbiased, so that $\langle \mathbf{f}(t) \rangle = 0$ and obey the fluctuation-dissipation theorem

$$\langle \tilde{\mathbf{f}}(t)\tilde{\mathbf{f}}(t') \rangle = 2k_B T \beta \delta(t - t') \tag{5 4}$$

The interaction force between the obstacle and the particle is modelled as a pseudo-hard core repulsive potential

$$\mathbf{f}_{\rm obs} = -\nabla V_{\rm obs} \tag{5 5}$$

$$V_{\rm obs} = c \times d^{-12}\ , \tag{5 6}$$

where d is the closest distance between the particle's surface and the obstacle The proportionality factor is chosen such that the minimal distance during the simulations is approximately $d \approx 0\,01\,\delta_p$ The displacement of the particle during one time step as caused by the flow, is equal to the velocity $\mathbf{v}(\mathbf{r})$ of the fluid at the centre of the particle The Langevin equation was integrated using a standard Euler approach

With the radius of the pillars set to $r_{\rm p} = \delta_p = 0\,5\,\mu$m, the system has $\delta_y = 2\,\mu$m, $\delta_x = 20\,\mu$m, $L_x = 32\,\mu$m and $L_y = 7\,7\,\mu$m Flow velocities in the range from $\overline{v_x} = 0\,25\,\mu{\rm ms}^{-1}$ to $25\,\mu{\rm ms}^{-1}$ have been simulated The

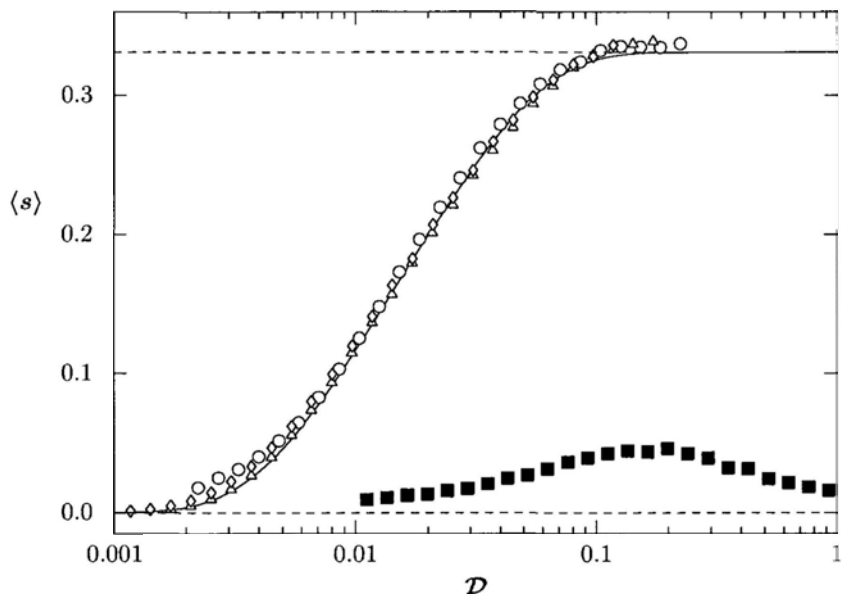

Figure 5.5: Mean step displacement for different particles as a function of the diffusivity $\mathcal{D}$, for particles of diameter $d = 1.0\mu m$ (blue circles), $d = 1.4\mu m$ (green triangles) and $d = 1.8\mu m$ (red diamonds), compared with theory predictions (solid black line). Black squares give the displacement of small particles of diameter $d = 0.2\mu m = 2r < \delta_p$. The dashed line shows the predicted maximal displacement $\langle s \rangle_{\max} = 1/2 - \epsilon = 0.321$.

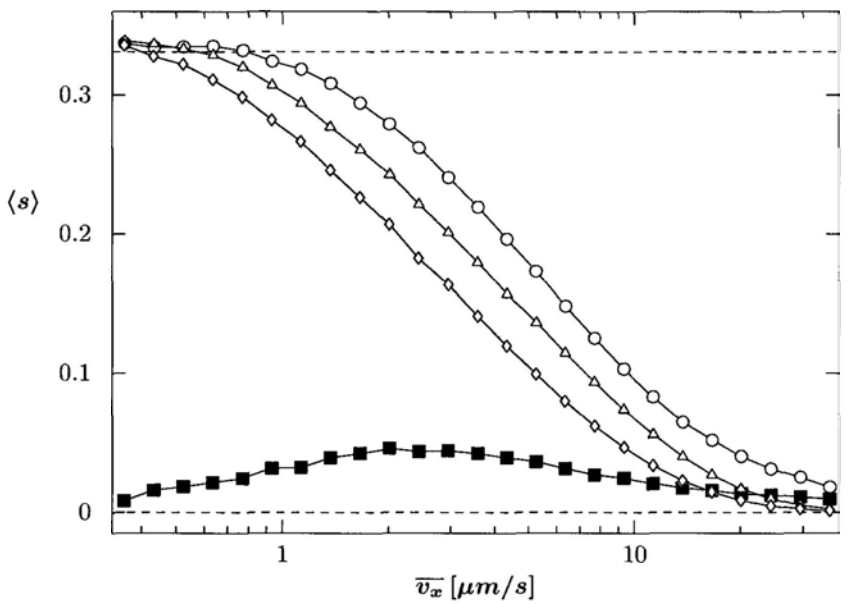

Figure 5.6: Mean step displacement for different particles as a function of the flow velocity v_x, for particles of diameter $d = 1.0\mu m$ (blue circles), d=$1.4\mu m$ (green triangles) and $d = 1.8\mu m$ (red diamonds). Black squares give the displacement of small particles of diameter $d = 0.2\mu m = 2r < \delta_p$.

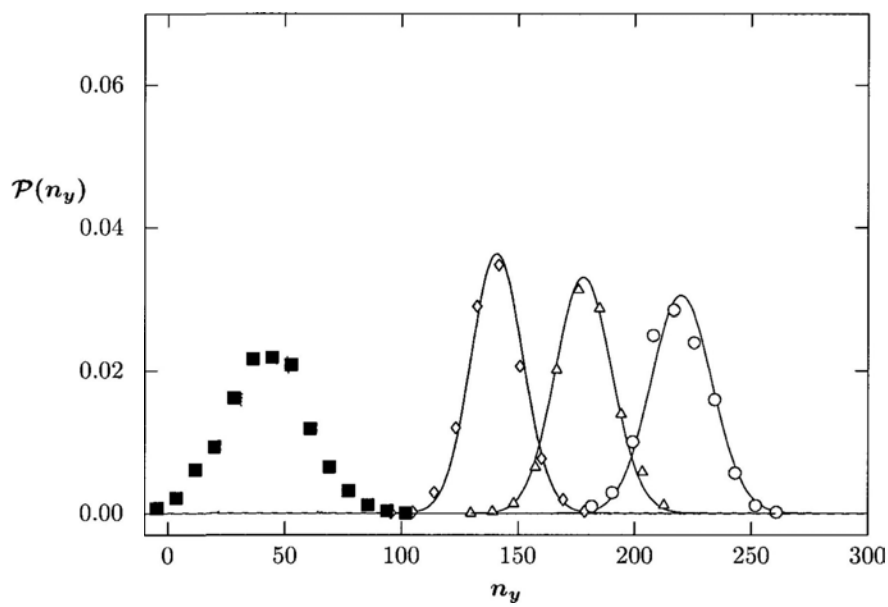

Figure 5.7: Particle distribution after passing $n_x 1,000$ rows, equivalent to 1000 ratchet cycles. Results for $d = 1.0\mu m$ (blue circles), $d = 1.4\mu m$ (green triangles) and $d = 1.8\mu m$ (red diamonds) are shown together with their theoretically predicted binomial distribution. The displacement of the small particles of diameter $d = 0.2\mu m = 2r < \delta_p$ (black squares) is a finite size effect and hence does not follow a binomial distribution (shown as dotted line).

corresponding Reynolds numbers $\mathrm{Re} = \overline{v_x} L_y/\eta$ are in the range between 10^{-10} and 10^{-8} and hence completely in the Stokes regime. In this hydrodynamic regime, the flow pattern is independent on the pressure gradient Δp_x, and it is thus sufficient to scale the velocity field $\mathbf{v}(\mathbf{r})$, in order to achieve the desired average velocity $\overline{v_x}$. The resulting rescaled mean displacement $\langle s \rangle = \langle \Delta y \rangle / L_y$ is depicted in Fig. 5.5 as a function of the dimensionless diffusivity $\mathcal{D}$ for four particle radii r. The diffusion constant D was calculated using the Stokes-Einstein relation, assuming water at $300K$ as the used liquid. The data reveals two operational regimes, depending on the particle size. In the first regime, with particle sizes larger than the inter-pillar distance $2r > \delta_\mathrm{p}$, the results agree qualitatively with the prediction of ratchet theory (Eq. (4.15)). In particular, the mean displacement converges closely to the maximum value $\langle \Delta y \rangle_\mathrm{max}/L_y = 0.33$ for large values of $\mathcal{D}$ as predicted in Eq. (4.17). This behaviour indicates that the symmetry of the flow field is indeed broken as predicted and that the ratchet effect occurs. Figure 5.6 shows the same data as a function of the average flow velocity $\overline{v_x}$. For a certain value of $\overline{v_x}$, the mean displacement decreases for larger particle sizes. This particle size dependence of the mean displacement facilitates vector chromatography, since the trajectories of particles with different radii point towards different directions.

In the second regime, with particle sizes smaller than the inter-pillar distance, $2r < \delta_\mathrm{p}$, the particle trajectories are not significantly inclined. Particles of these sizes can pass between the pillars. As a consequence, they perceive each pillar as an individual impermeable obstacle. Since individual pillars are not able to break the symmetry of the flow pattern, the mean trajectories are not expected to be inclined. The small inclinations that we observe in this regime may rise from finite-size effects [60].

Assuming that all probabilities but p_{+1} and p_0 are negligible, the rescaled

mean displacement $\langle \Delta y \rangle / L_y$ is equal to p_{+1}. The probability to find the particle displaced by n_y gaps in y-direction after having passed n_x rows in x-direction should hence be given by a binomial distribution. In Fig. 5.7 the numerical results of $\mathcal{P}(\langle s \rangle)$ for $\overline{v_x} = 2.5\ \mu\mathrm{ms}^{-1}$ are compared with the corresponding binomial distributions for $n_x = 1000$. For $2r > \delta_p$, the numerical data is well described by binomial distributions. For $2r < \delta_p$ however, the numerical results clearly deviate from the binomial distribution. This further indicates that the behaviour of small particles in this regime is not described by the discussed ratchet effect. The results in this figure demonstrate that vector chromatography can be effectively realised in such a device, since the distributions for the three particle sizes that operate in the first regime are clearly distinguishable and completely separated from the distribution for the particle size that operate in the second regime.

5.4 Summary and Outlook

In this chapter we have demonstrated that it is in principle possible to create ratchet-based particle separation devices using pressure-driven flows as the driving force. The key feature of our design is the use of obstacles permeable to the flow but impermeable to macromolecules. As a result, particles driven by the fluid flow actually interact with the obstacles, rather than being guided around them as it would be the case for solid obstacles. Consequently, the symmetry of the experienced ratchet potential is broken, and vector chromatography based on the particle's diffusivity becomes possible.

The general feasibility of the design was shown using Brownian dynamics simulations. A discussion of the overall capabilities of the proposed design, however, depends on various parameters of the experimental realisation,

which is currently underway at the National University of Singapore. For the discussed design, we used large circular pillars, since such obstacles can be included directly in simulations and can readily be fabricated with today's lithographic methods. However, the choice of such a simple design also causes some problems. For one, the relationship between the asymmetry ϵ and the obstacle gap width δ_y restricts the range of particle sizes that can be separated. For another, particles that are only slightly larger than the inter-pillar gap $2r \approx \delta_p$ get sucked into and consequently stuck in the gaps. Plenty of remedies to both of these problems are available, for example by replacing the circular pillars with rectangular or triangular pillars in such a way that the inlet is not cone-shaped. Given that the feasibility of such measures strongly depends on the realisation techniques, we will postpone their discussion until details of the experimental realisation are available.

Part III

Dynamic Models on Adaptive Co-Evolving Networks

Chapter 6

Networks and Dynamic Models: A Review

In this chapter, we will briefly discuss two concepts essential for the understanding of the discussions in Chs 7-9 *Networks* and *Dynamic Models* Both topics have been extensively studied for over a decade, and accordingly we will not be able to provide an actual overview over either of these fields Comprehensive reviews on the physics of networks can be found in Refs [5, 61 62, 63] For a more general but less detailed discussion see Ref [6] A thorough review of various dynamic models, including the opinion formation model discussed below (Sec 6 5), can be found in Ref [64]

6.1 What Are Networks?

A graph is defined by a set of vertices and a set of edges that each connect two vertices For our purposes, networks and graphs differ mainly with regard to terminology For networks, we will commonly refer to the vertices as *nodes*

and to the edges as *links* Links define relationships between nodes, and nodes that are connected via a link are referred to as *neighbours* In the same manner, the set of nodes connected to a node A is called A's *neighbourhood*

Networks can be used to represent many real-life systems In rail networks, nodes represent stations and depots, while links represent tracks [65] In computer science networks are used on many different levels [66] On the so-called PHY-layer, active components that send and receive signals are represented as nodes, while cables (or even radio frequencies) are the links connecting them On higher levels, nodes represent application servers and clients such as web servers and internet browsers The entire infrastructure, cables, hubs, routers etc , serve as links in such a model Also social or professional relationships between humans can be represented by networks Links then represent the relationships between individuals, who themselves are mapped onto nodes [61, 62, 64]

Because they are used as models for such a plethora of systems, networks can possess more elaborate features than those just described Links can be directed, for example to represent causality They can be weighted, to represent the intensity of a relationship Also, they can be time-dependent, for example to distinguish transient from long-term relationships The widely investigated network of cooperation among scientists can serve as an example to illustrate the different types of networks [67, 68, 69] A simple network representation of scientific cooperation would use nodes to represent researchers Researchers who have co-authored at least one research paper are considered cooperators and connected through links Figure 6 1(A) illustrates this relationship using the authors of research articles related to this thesis as an example The used graph is bidirectional and unweighted and therefore does not contain information about the frequency or importance of the cooperation This is

addressed in Fig 6 1(B) Here, the line width corresponds to a link weight, which itself is a representation of, for example, the number of coauthored papers Finally, Fig 6 1(C) represents a related citation matrix as a directed network Research articles are the nodes in this network, and a link from one paper to another represent citations of the former by the latter Since a paper can only cite previous articles, this graph does not contain any closed loops A comprehensive graph of such data, representing the citation relationships among the majority of published scientific articles is published by Thomson as the so-called *Web of Knowledge*

6.2 Properties of Networks

In this thesis, we will deal only with the simplest kind of networks that feature bidirectional links without an associated weight Still, such networks possess a number of remarkable features In what follows, we will introduce properties commonly used to describe such networks, and discuss these properties for two exemplary types of networks

6.2.1 Connectivity

The connectivity or degree of a node is the number of links connected to the node, or, equivalently, its number of neighbours For the whole network, we often define or measure a mean degree We denote the degree of a single node as κ, and the mean degree of the entire network as k Apart from the mean degree of a network, the distribution of κ – its *degree distribution* – is a significant property of complex networks It was found that real-world networks often

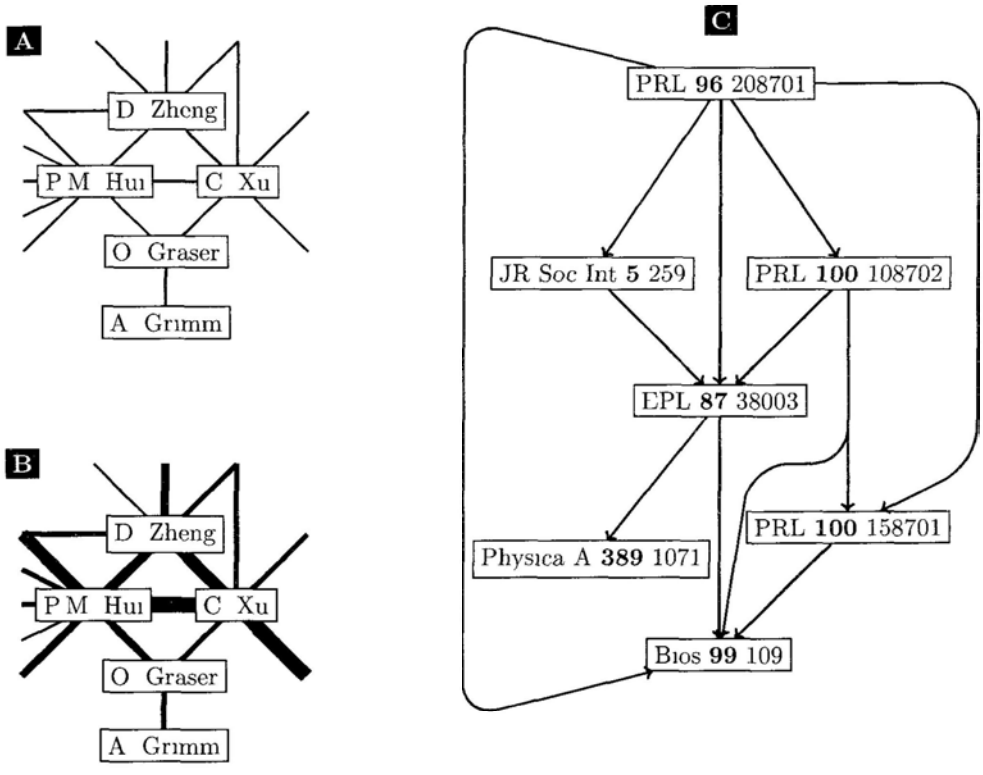

Figure 6.1 Different kinds of networks illustrating scientific cooperation (A) Bidirectional unweighted graphs with links representing cooperation between two authors (B) Weighted graph The weight of a link is illustrated in the line width and corresponds to the number of coauthored papers (C) Directional network illustrating the citation relationships among different papers

feature a power law degree distribution, and consequently various models were developed that aimed to explain how such structures emerge.

6.2.2 Clustering Coefficient

In many networks, the neighbourhoods of two neighbouring nodes overlap significantly. The clustering coefficient is a quantitative measure of this overlap. In an extreme case, the nodes comprising the neighbourhood of a node are all connected to each other. If this neighbourhood consists of κ nodes, then there exist $E^{(\max)} = \kappa(\kappa - 1)/2$ links among them. However, in many cases, only a smaller number E of such links exists. The clustering coefficient of node A's neighbourhood is then defined as the ratio between existing and possible links

$$C_{\mathrm{A}} = \frac{2E_{\mathrm{A}}}{\kappa_{\mathrm{A}}^2 - \kappa_{\mathrm{A}}} \,. \tag{6.1}$$

This value can be averaged over the entire network consisting of N nodes to give the mean clustering coefficient

$$C = \frac{1}{N} \sum_{i=0}^{N} C_{\mathrm{i}} \,. \tag{6.2}$$

It should be noted that the clustering coefficient only relates to local neighbourhoods. A well-mixed network, where all nodes are connected to each other, and a set of mutually disconnected triplet loops, for example, would both feature a mean clustering coefficient of $C = 1$.

6.2.3 Mean Degree of Neighbours

The average degree of the neighbours $\langle \kappa_{\mathrm{nn}} \rangle$ of a node A is defined as the mean degree of all nodes connected to A:

$$\langle \kappa_{\mathrm{nn}} \rangle = \sum_{i \in \mathcal{N}(A)} \frac{\kappa_{\mathrm{i}}}{\kappa_{\mathrm{A}}} , \tag{6.3}$$

where $\mathcal{N}(A)$ is the set of neighbours of node A. It is commonly averaged over all nodes A_j of the same degree $\kappa_j = q$ and then studied as a function of the node degree q,

$$\langle \kappa_{\mathrm{nn}} \rangle (\kappa = q) = \sum_{\kappa_{\mathrm{j}}=q} \sum_{A_i \in \mathcal{N}(A_j)} \frac{\kappa_{\mathrm{i}}}{q N_{\mathrm{q}}} , \tag{6.4}$$

where N_{q} is the number of nodes with degree q. The mean neighbour degree can be used to find assortative behaviour of networks, e.g., whether or not nodes of a certain degree prefer to associate with identical or similar nodes [70].

6.3 Examples of Complex Networks

In order to illustrate the types of networks and their properties, we will briefly discuss two popular network models and their features.

6.3.1 Random Graphs

The theory of random graphs was first discussed by Paul Erdös [71]. Consider a set of N nodes, for which exists a maximum of $L^{(\mathrm{poss})} = N(N-1)/2$ possible links that can connect these nodes. A random graph with mean degree $k = 2L/N$ can be generated by randomly selecting L links from this set of possible links. Alternatively, an identical random graph can be generated

by creating every link out of the set of possible links with probability p The two methods are equivalent if the parameters are chosen such that they create the same mean degree

$$2pL^{(\mathrm{poss})} = kN \tag{6 5}$$

In both cases, a network with binomial degree distribution is generated The probability $\mathcal{P}(\kappa = q)$ to randomly pick a node with degree q is

$$\mathcal{P}^{(\mathrm{bin})}(\kappa = q) = \binom{N-1}{q} p^{\mathrm{q}}(1-p)^{\mathrm{N-q-1}} \tag{6 6}$$

Generating a very large network for simulation purposes in such manner is a rather expensive process, since either memory or CPU consumption scales as $\mathcal{O}(N^2)$ Mathematically, it is known that the binomial distribution converges against the Poisson distribution for large values of N

$$\lim_{N\to\infty} \mathcal{P}^{(\mathrm{bino})}(\kappa = q) = \mathcal{P}^{(\mathrm{psn})}(\kappa = q) = \exp(-k)\frac{k^{\mathrm{q}}}{q!} \tag{6 7}$$

Accordingly, we can also generate a random network using a Poissonian method by randomly selecting two nodes, linking them, and repeating the process $L = kN/2$ times In this case care has to be taken to avoid self-linking or multiple links between two nodes This reduces both memory and CPU consumptions to order $\mathcal{O}(N)$

Figure 6 2 shows the properties of a random graph Figure 6 2(A) displays the degree distributions of three random graphs with different mean degree, shown as symbols All graphs have $N = 10,000$ nodes in total The actual degree distribution thus differs slightly from the Poissonian distribution, which is the limiting distribution for networks of infinite size Such Poissonian distributions are shown as lines of the same colour

Figure 6 2(B) displays the average neighbour degree $\langle \kappa_{nn} \rangle$ as a function of a node's own degree κ Since there exists no assortative mechanism, the

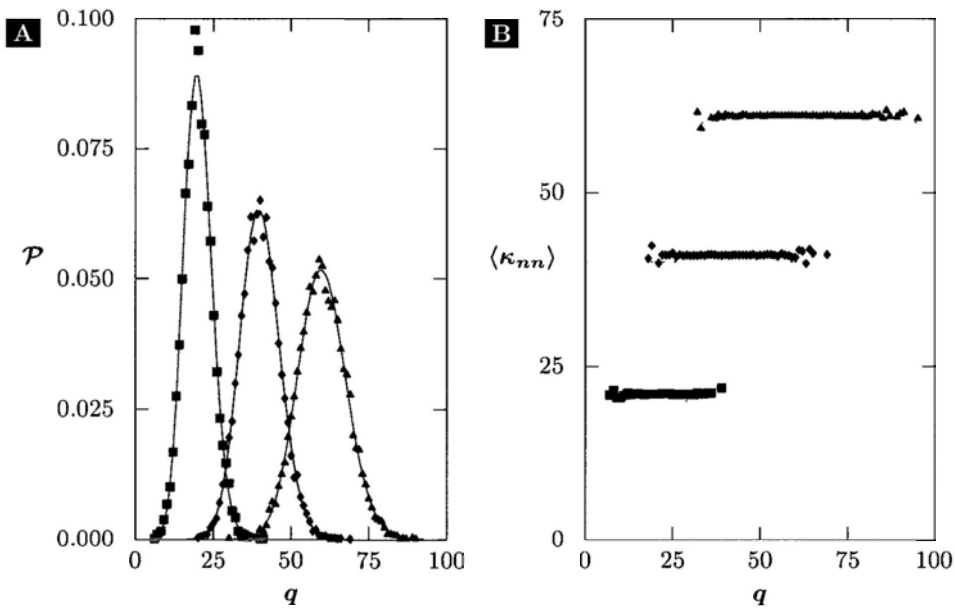

Figure 6.2: Properties of random graphs. (A) Degree distributions with mean degree $k = 20$ (orange squares), $k = 40$ (green diamonds) and $k = 60$ (purple triangles), all for a network with $N = 10,000$ nodes. Lines show Poisson distributions with identical mean, corresponding to the theoretical limit for $N \to \infty$. (B) Nearest-neighbour mean degree distributions of the same systems. Dotted lines show the mean degree of these networks.

expected distribution is flat. At the boundary of the displayed interval, the mean neighbour degree is averaged over very few nodes only, which leads to larger fluctuations. The overall average of the mean neighbour degree is slightly higher than the system's mean degree k, since high-degree nodes are included in more neighbourhoods than low degree nodes.

6.3.2 Preferential Attachment – the Barabási-Albert Model

Many real-life networks were found to have a power-law degree distribution, i.e., $\mathcal{P}(\kappa = q) \propto q^{-\gamma}$, with some exponent $\gamma > 1$ [72]. Examples include the topology of internet protocol devices (OSI level 3) [66], scientific citation networks [69], and even the metabolic networks of eukaryotic organisms [73]. Such networks are also sometimes referred to as scale-free networks, since their degree distribution can mapped on itself using a proper rescaling of both axes [1].

Barabási and Albert proposed a mechanism that explains why many human-generated networks follow such a degree distribution [74]. Their underlying assumption is that new individuals who enter a system prefer to associate themselves with individuals who are already popular. Turning this into a mathematical model, they assumed that a system is started by a group of m_0 individuals, who form a network with homogenous degree $m < m_0$. Individuals joining the network will also establish m connections to existing individuals. The probability for a new individual A to pick an existing node B as one of its neighbours is assumed to be proportional to the degree of B:

$$\mathcal{P}(A \to B) = m\frac{\kappa_B}{2L_{\text{tot}}} , \tag{6.8}$$

[1] For a power-law degree distribution $y = f(x) = c \times x^\gamma$, we have $f(\alpha x) = c \times \alpha^\gamma x^\gamma = \alpha^\gamma f(x)$, i.e., if the x-axis is rescaled with a factor α, the graph is mapped onto itself if the y-axis is scaled by α^γ. This feature is unique to power-law distributions.

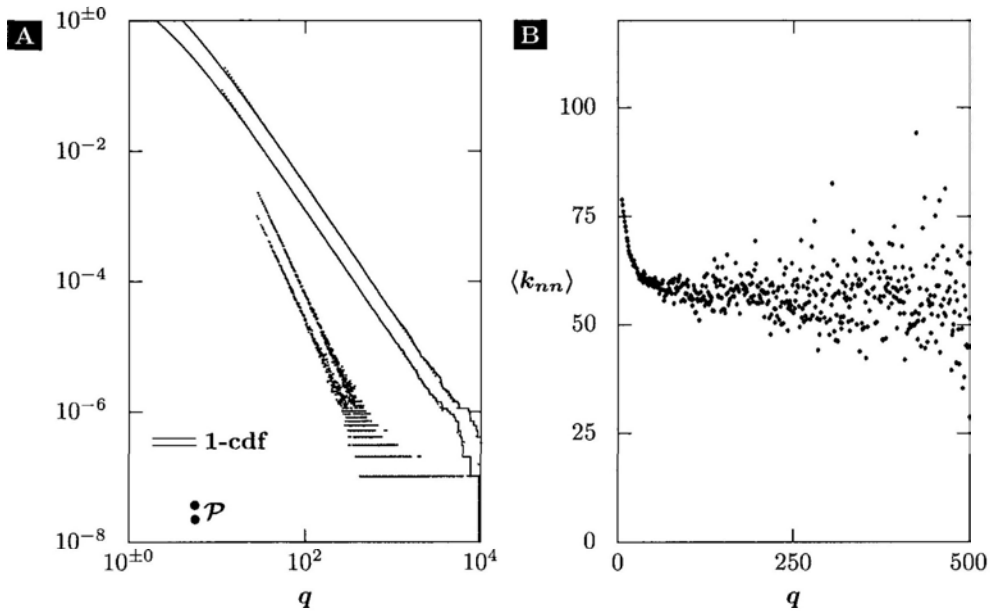

Figure 6.3: Properties of Barabási-Albert networks. (A): degree distribution $\mathcal{P}(\kappa = q)$ (symbols) and cumulative degree distribution 1−cdf, for $m_0/m = 6/5$ (red) and $m_0/m = 4/3$ (blue). Dotted lines show fitted power-laws for the range with exponents $\gamma_1 + 1 = -1.9782$ (red) and $\gamma_2 + 1 = -1.9619$ (blue). (B): Average neighbour degree distribution, shown for low degree nodes with $q < 500$

where L_{tot} is the total number of links in the network. It was shown in several ways that such a mechanism leads to a scale-free degree distribution [75, 76]·

$$\mathcal{P}(\kappa = q) = \begin{cases} 0 & : \quad q < m \\ 2m^2 q^{-3} & : \quad q \geq m \end{cases} . \tag{6.9}$$

Figure 6.3 shows the properties of a Barabási-Albert (BA) network with $N = 10^7$ nodes. Figure 6.3(A) shows the degree distribution for two different setups $m_0 = 6$, $m = 5$ and $m_0 = 4$, $m = 3$. This means that the initial configuration was a fully connected network in both cases, in one case

with four and in another with six nodes in total. Inevitable fluctuations in the degree distribution for high q make it difficult to see the power-law behaviour clearly. To even out these fluctuations, we can instead look at the cumulative distribution function

$$\mathrm{cdf}(\kappa = q) = \int_m^q \mathcal{P}(\kappa = q')\mathrm{d}q' = 1 - m^{\gamma-1}q^{-\gamma+1} \ . \tag{6.10}$$

Any power law behaviour in the degree distribution can be found again in the cumulative degree distribution, with the exponent being increased by 1.

The dotted lines are power law distributions of type $a \times q^{-\gamma+1}$, with $\gamma_1 = 2.9782$ for $m = 5$ and $\gamma_2 = 2.9619$ for $m = 3$. To obtain these values, a linear function $y = \log(a) - \gamma x$ was fitted against the log-log curve of the recorded degree distributions, i.e., the fitting algorithm minimised the sum over squares of deviations on the log-log scale. Both values are very close to the theoretically predicted exponent $\gamma = 3$.

Figure 6.3(B) shows the average neighbour degree $\langle \kappa_{nn} \rangle$ for a limited range of $q \leq 500$. Unlike the case of the random graph, associativity patterns can be observed here. Young individuals with very few connections are predominantly connected to high-degree nodes, while the neighbourhood of older nodes with higher degree contains more low degree nodes. For higher degrees, averages are taken over very few (100 out of 10^7) nodes, resulting in a highly fluctuating distribution.

6.4 Dynamic Models

We can define a dynamic model as a set of individuals, or agents, together with a set of properties these individuals have, and a set of rules that define the evolution of the individuals and their properties. Commonly, dynamic

models are used to describe some aspects of human society – the evolution of opinions [77], of diseases [78], or of social relations [79] For the use in physics, these situations are often reduced to their most fundamental aspects e g is a person infected or not, does she agree with a certain opinion or not, does he cooperate with others or not, and the like If there are only two possible states for the properties of an individual the dynamic model is sometimes referred to as *binary* or *spin like*

The relationship between individuals in a dynamic model can be that of a well-mixed network, i e , every individual is connected to every other individual in the group, or specific to each individual In the latter case networks are commonly used to describe the relationships between individuals Individuals occupy a node on the network, and the relationships between individuals are described by simple, directional, or weighted links In the discussion of such models the terms *individuals*, *agents* and *nodes* are often used interchangeably

The status of the individuals can also be used to classify the links into different categories Consider the Susceptible-Infected-Removed (SIR) model a non-binary epidemics model [80, 81, 82] In this model individuals go through a sequence of three possible states susceptible i e healthy and able to contract a disease, infected and removed Susceptible individuals contract the disease from infected agents, whereafter they are themselves contagious and can infect other susceptible individuals After a while they may either recover and acquire immunisation against the disease or succumb to the disease and die In either outcome, they will not participate in the epidemic spreading anymore i e , neither will they contract the same disease again, nor will they spread it to other individuals With every agent taking on one of these three states each link can be classified into one of six categories, depending on the state of the individuals they are connecting susceptible-susceptible susceptible-infected,

susceptible-removed, infected-infected, infect-removed, and removed-removed

The evolution of the status of individuals is governed by a set of rules that represent the underlying situation Generally speaking, these rules describe how the properties of individuals change, depending on their current properties their neighbourhood, and possibly random events For the aforementioned SIR model, the evolution of the disease is commonly described in rates With a certain rate τ, an infected individual will pass the infection to each of its susceptible neighbours With another rate r, the same individual will either overcome or succumb to the disease and remove itself from the system [80] The usage of rates reflects the uncertainties that exist in the spreading of real-world epidemics The rules of the model also imply that diseases are only spread through the links connecting susceptible and infected individuals Hence, the number of such classified links is a key observable of this model

6.5 The Dynamics of the Majority Voter Model on a 2D Lattice

As an example of a dynamic model on a network we will briefly discuss some results of a study on the majority voter model on a 2D-lattice, originally published by Chen and Redner [83]

Voter models are a popular class of opinion formation models The model represents a voter's opinion on a referendum that offers two choices — a runoff presidential election or a proposition, for example The model fully disregards the actual issue, i e it does not distinguish between the legalisation of Marijuana and a referendum on joining the European Union Instead, it focusses on the way opinions are spread between individuals Different classes of the

voter model have been suggested, e g , the direct voter model, where a node asks one of his neighbours for and adopts his opinion, and the reverse voter model, where a node will talk one of his neighbours into adopting his opinion [84]

In contrast, the majority voter model depends much stronger on the overall topology of the system During one time step, a single individual is picked at random This individual and all his neighbours form one opinion group The entire group then adopts its internally predominant opinion In the following, we will use a two-dimensional square lattice with periodic boundary conditions as the underlying network Opinion groups thus always comprise five individuals and a majority opinion always exists

Figure 6 4 shows the evolution of such a system A lattice with $N = 50 \times 50 = 2500$ nodes forms the underlying network The initial opinion of every node is randomly chosen with equal probability Already after very short time $t = N$, domains of homogenous opinion have formed As a result the evolution of the system is slowed down, since the majority voter model rules do not create any changes when applied inside a homogenous domain As the evolution proceeds, enclosed areas of one opinion shrink until the opinion becomes extinct At around $t = 10N$, stripe-like structures form as these have the lowest density of cross-opinion links Finally (at around $t = 83N$), all nodes have adopted the same opinion

A more quantitative illustration of this process is shown in Fig 6 5 By associating the binary voter model with a magnetic spin system, we can define a pseudo-magnetisation of the system as $m = (N(Op\ A) - N(Op\ B))/N_{\text{tot}}$ Similarly, we can count the links between two nodes of opinion A L_{AA}, two nodes with opinion B L_{BB}, and between nodes of opposite opinion L_{AB} Figure 6 5(A) and (B) show the behaviour of the such defined magnetisation m and

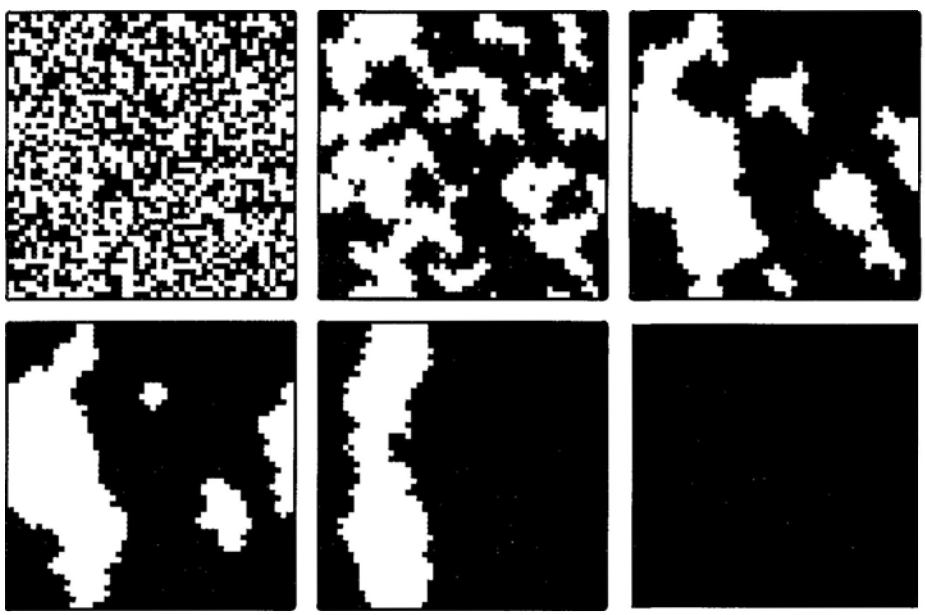

Figure 6.4: Evolution of a majority game opinion formation model on a square lattice of $N = 50 \times 50$ nodes. From left to right and top to bottom: the state of an exemplary system after zero, N, $5N$, $10N$, $50N$ and $100N$ iterations. Consensus was reached at $t \approx 83N$.

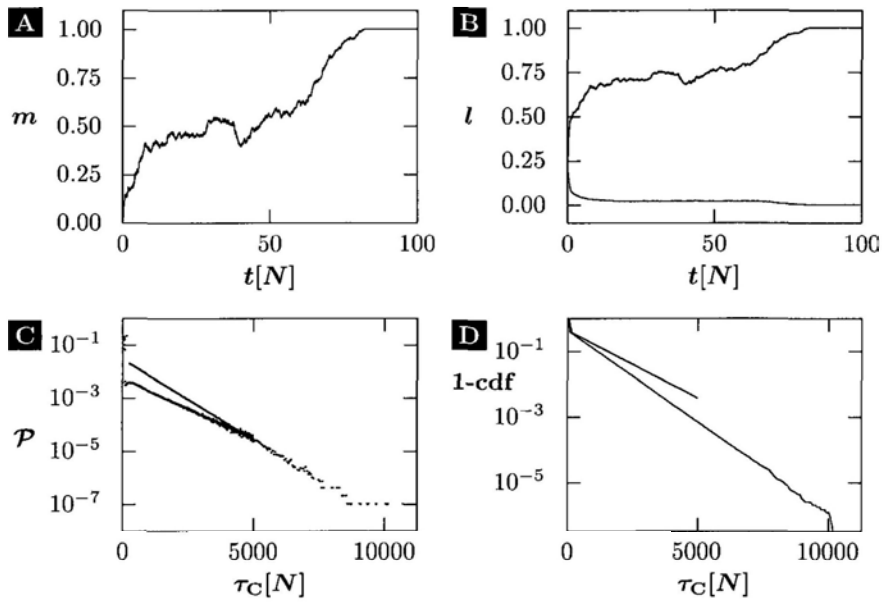

Figure 6.5: Evolution of the majority voter model. (A) Evolution of magnetisation and (B) link density (green: l_{AA}, yellow: l_{AB}) for the single system of Fig. 6.4. (C) Consensus time distribution. (D) Cumulative distribution function. (C)&(D): Data taken for an ensemble of 10,000,000 $N = 50 \times 50$-systems (red) or $1,000,000$ $N = 100 \times 100$-systems (blue).

link densities $l_{\mathrm{AB}} = L_{\mathrm{AB}}/L_{\mathrm{tot}}$ over time. The number of links between nodes of opposite type, initially half the number of total links, drops rapidly, This corresponds to the formation of homogenous domains observed before. The evolution continues then rather slowly until $t \approx 60N$. At this time, the last domain of the minority opinion has been fully surrounded. Consensus, i.e., a uniform opinion of either type, is reached at roughly $t \approx 83N$.

The consensus time τ_C is an important quantity in the research of opinion formation [85, 86, 87]. Figure 6.5(C) shows the consensus time distribution for two ensembles, one comprising ten million systems with 2500 nodes each, one

comprising one million systems with ten thousands nodes each. Because the distribution again shows large fluctuations for large τ_C, we show the cumulative distribution functions in Fig. 6.5(D). Both figures show that the consensus time distribution decays exponentially $\mathcal{P}(\tau_C = \tau) \propto \exp(-\lambda\tau)$, with a decay constant depending on the system size.

Chapter 7

Introduction to Complex Adaptive Networks: Epidemics

In the following, we will discuss the properties of an adaptive Susceptile-Infected-Susceptible (SIS) model system. This model system combines the mechanisms of the SIS epidemics dynamic model [78, 82] with an adaptive reaction mechanism in which healthy agents try to minimise their exposure to infected agents.

7.1 The SIS Epidemic Model

7.1.1 Model Introduction

The SIS epidemics model defines two possible states of an agent: one infected (I) state during which an agent suffers from the disease and can infect other agents, and one healthy state during which an agent is susceptible (S) and can contract the disease from infected agents with whom it is in contact.

The state sequence is $S \xrightarrow{\tau} I \xrightarrow{r} S$. This means that a recovered node neither acquires immunity nor dies from the disease. Instead, it might be instantly infected again, possibly even by a neighbour whom it infected itself. In biological terms, such a model can be valid for certain sexually transmittable or gastrointestinal diseases. Also, diseases caused by quickly mutating viruses (with the mutation time shorter than the average spreading time) might follow the SIS cycle. In more common infectious diseases, the host usually either withers or acquires immunity due to the presence of antibodies in his system. Such diseases are better described by a Susceptible-Infected-Removed model. However, the SIS model offers very interesting insights into the dynamics of epidemics.

Consider a random static network of N nodes, with $L_{\text{tot}} = kN/2$ links in total, and hence an average of k neighbours per node, with the agents sitting on nodes following the SIS cycle. During a given discrete time step, any infected agent can spread the disease to each of its neighbours with probability τ. At the same time, it might recover with probability r, irrespective of its surroundings. If the time interval is chosen sufficiently small, probabilities of higher orders such as contracting the disease from two neighbours during the same time step can be neglected. In such a first-order approximation, the probability for any single susceptible node to become infected is proportional to the number of infected neighbours, $\mathcal{P}_{S\to I} = \kappa_I \times \tau$. Since the actual infection rate also depends on the number of infected contacts, we refer to τ alone as the model's *contagiousness*. If a node, on average, recovers before it infects one of its neighbours, the disease will die out. If it, however, manages to infect on average more than one of its neighbours, the disease will spread over the system. If that is the case, then the infection will spread over the network until some equilibrium fraction n_I^{eq} is reached. At this level, an infected nodes has

fewer susceptible neighbours, such that now every infected node on average infects exactly one susceptible neighbour before they recover. In this manner, we can define the infection threshold

$$\tau > \frac{r}{k} \,. \tag{7.1}$$

The infection threshold is the contagiousness level required for the spread of a disease on a fully susceptible network. For a contagiousness above this threshold, the corresponding equilibrium infection level is

$$n_I^{\text{eq}} = 1 - \frac{r}{\tau k} \,. \tag{7.2}$$

Such a threshold is well defined only for the case of a well-mixed network, although it may serve as a rough guiding principle in the case of random graphs. Interestingly, the extreme heterogeneity of scale-free network makes the definition of such a threshold impossible. This problem was discussed using model systems [88, 89], but also shown to exist in the spreading of computer viruses over the internet [90, 91].

Figure 7.1(A) shows the dynamics of the SIS mechanism on a small subnetwork. Two infected nodes are connected via four links to susceptible nodes (SI-links, shown in red). The disease can spread over each of these links, hence the probability for any form of infection spreading in this subnetwork is $\mathcal{P}(\exists S \to I) = 4\tau + \mathcal{O}(\tau^2)$. Other connections between two susceptible nodes (SS-links, blue) or two infected nodes (II-links, black) do not affect the evolution of the system. At the same time, both nodes can recover with probability r, so the probability for one of the two possible recovery processes to occur is $\mathcal{P}(\exists I \to S) = 2r$. The lower panel shows two possible states of the subsystem after one recovery (left) or infection (right) process has taken place. The single recovery process of node $I_0 \to S_0$, occurring with $\mathcal{P} = r$, turns two SI- into SS-links and one II- into an SI-link. The infection process $S_1 \to I_1$ can occur

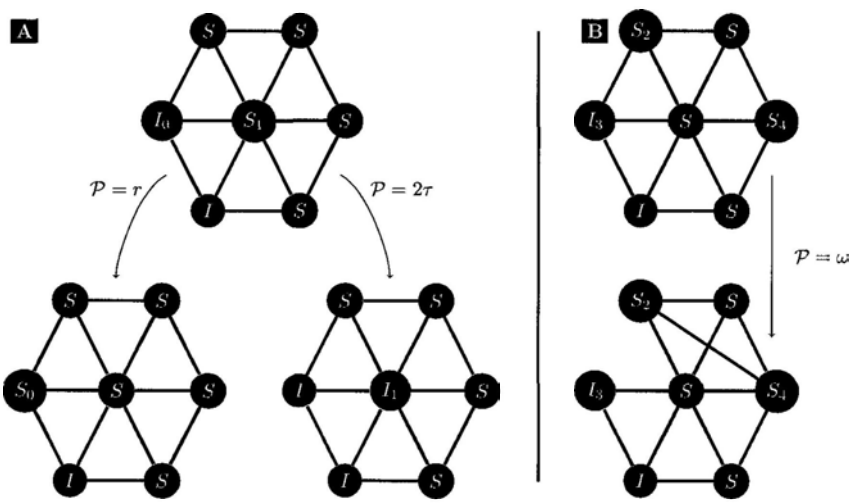

Figure 7.1: Schematics of the infection and recovery process of the SIS model (A) and the rewiring process (B). Probabilities are given for the changes shown. Link colours indicate active SI-links (red), inactive SS-links (blue) and inactive II-links (black).

in two ways, since both infected nodes can spread the disease to the central node It therefore has a probability of $\mathcal{P} = 2\tau$

7.1.2 Adaptive Re-wiring

Networks do not have to be static They can for example, evolve through insertion or removal of nodes or of links Of particular interest is when the dynamics of the network do not occur independently, but rather in order to adapt to the corresponding dynamic model The process of such adaptive rewiring is also referred to as coevolution of the dynamic model and the network The fundamental difference to simpler previous models is that the evolution of the network now depends on the current state of the dynamic model On the contrary, in previous models only the evolution of the dynamic model did depend on the state of the network i e , whether or not an agent changes its status may have depended on its neighbourhood The evolution of the network itself, if existing, was typically depending only on the state of the network, and not on any state the agents may have had

Gross *et al* proposed a set of rules to create such an adaptive reaction to an SIS-type epidemics hereafter referred to as the adaptive SIS model [92 7] The process of adaptive rewiring is shown in Fig 7 1(B) Starting from the same subnetwork configuration as before, a susceptible node S_2 connected to an infected node I_3 may at a time step decide to reduce its exposure to the disease by cutting this connection In doing so, it will seek another susceptible node S_4 and establish a link with it such as to keep its number of neighbours constant The adaptive SIS model assumes absolute transparency of the epidemic model, i e , it is always public whether a node is infected or susceptible Because of this, rewiring always turns an SI- into an SS-link, and this method is hence

efficient in reducing the exposure of susceptible nodes even if the majority of all agents is infected The probability for any single SI-link to be rewired in such manner is denoted as the rewiring probability ω In this model, the rewiring probability is always constant The possibility of a rewiring possibility that depends on the public awareness of the disease, or more specific the infection level in the system, was discussed in Ref [93]

7.1.3 Evolution

The system evolves through a series of short discrete time intervals (or steps) δt At any time step, three kinds of events can occur Every infected node can recover, every SI-link can infect the susceptible node at its end, and every SI-link may be disconnected from its infected node and re-wire to another, randomly chosen susceptible node All these actions are based on the state of the system at the beginning of the interval After the outcome of all possible actions is decided, the state of the nodes and the network are updated at the end of the interval We can use the recovery rate r to define an intrinsic time scale $\propto 1/r$, and express all other rates in terms of r For computer simulations, δt then has to be chosen to be small compared to this time scale such as to avoid the occurrence of multiple events at a single node $\delta t \ll 1/r$ A similar model for a susceptible-infected-recovered-susceptible epidemic cycle was discussed by Shaw *et al* [94]

7.2 Mean Field Theory Derivation

7.2.1 Node-level Derivation

Originally, the time evolution of the epidemics of an SIS model was described by means of a single ordinary differential equation (ODE) [82] The underlying idea is that the agents form a well-mixed network Any single agent is weakly connected to any other agent, and the neighbourhood of each agent thus consists of the entire network In such a case every S-node has $N_I = N - N_S$ infected neighbours that can infect him At the same time, those I-nodes can recover hence the time evolution is described by the equation of motion (EOM) [1]

$$N_S = r(N - N_S) - \tau \times N_S \times (N - N_S) \tag{7 3}$$

Such a simple approach is not possible in our case For one a topological network differs from a well-mixed network in that a disease spreading over a network cannot instantly infect remote nodes Furthermore particularly in the case of rewiring, we need to be able to distinguish infections in isolated areas from those in highly connected areas Therefore, additional variables are required to describe the link configuration of the system

We can use five variables to describe the macroscopic state of the system The number of infected and susceptible agents, N_S and N_I, as well as the number of links between two susceptible agents two infected agents and one infected and one susceptible agent each, written as L_{SS}, L_{II} and L_{SI}, respectively Alternatively, lower case quantities will refer to the densities with respect to the total number of links or nodes e g , $l_{SI} = L_{SI}/L_{\text{tot}}$ We keep

[1] To give meaningful results, the contagiousness in such systems is usually antiproportional to the number of nodes in total

the total number of nodes $N = N_S + N_I$ and links $L_{\text{tot}} = L_{SS} + L_{SI} + L_{II}$ constant Hence, these variables are actually reduced to a set of three independent variables For most figures and equations we will use N_I L_{SI} and L_{II} or the respective densities as the independent variables However, if necessary we will freely change the set of variables, using the above constraints To refer to any of these variables without choosing any single one in particular, we will use the quantity $X \in \{N_S, N_I, L_{SS}, L_{SI}, L_{II}\}$, or lowercase x for densities

In total, there are three types of events that can alter these variables spreading the disease i e , turning a susceptible into an infected node, recovery, i e , turning an infected into a susceptible healthy node and rewiring, i e , the cutting of an SI-link and creation of an SS-link between the original and another susceptible node All these events change the macroscopic state, but the change depends on the node's local configuration To denote the configuration of a single node instead of the entire system, we use lower case greek letters, e g λ_{SI} for the number of SI-links of a single node These changes and their macroscopic results are illustrated in Fig 7 2

Knowing all these microscopic changes, the total expected change of the macroscopic variables can be written as a series of conditional probabilities Let us denote the three different events recovering re-wiring, and getting infected by E_i with $i \in \{1, 2, 3\}$ Recovering and re-wiring affects infected nodes while infection affects susceptible nodes The change in the macroscopic quantities $X \in \{N_S, L_{SI}, L_{II}\}$ of any of these events E_i can be added up if the number of susceptible and infected neighbours $\lambda_{\alpha S}, \lambda_{\alpha I}$ of the node of status

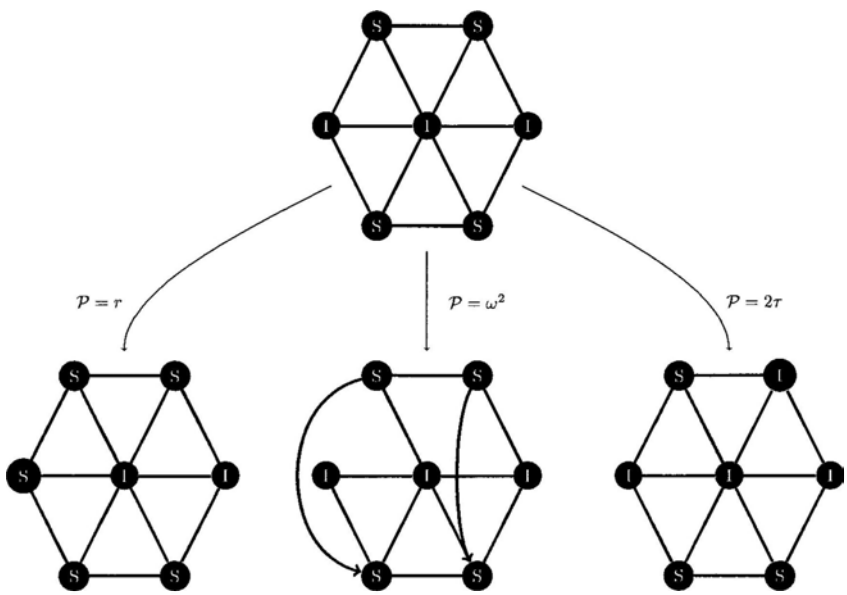

Qty	General	Ex
ΔL_{SI}	$-\lambda_{SI} + \lambda_{II}$	-1
ΔL_{II}	$-\lambda_{II}$	-1
ΔS	1	1

Qty	General	Ex
ΔL_{SI}	-1	-1
ΔL_{II}	0	0
ΔS	0	0

Qty	General	Ex
ΔL_{SI}	$-\lambda_{SI} + \lambda_{SS}$	-1
ΔL_{II}	$+\lambda_{SI}$	2
ΔS	-1	-1

Figure 7.2: Changes on a network through recovery (left), rewiring (middle) and infection spreading (right). Tables below give the resulting changes in the macroscopic variables, in general (middle column) and for this subnetwork (right column).

α is known: $\Delta X \equiv \Delta X(E_\imath, \lambda_{\alpha S}, \lambda_{\alpha I})$. We hence write

$$\begin{aligned}
\Delta X_{\text{tot}} &= S \times \sum_{a,b=0}^{N-1} \mathcal{P}(\lambda_{SS} = a)\mathcal{P}(\lambda_{SI} = b|\lambda_{SS} = a)\mathcal{P}(E_3, \lambda_{SI})\Delta X(E_3, a, b) \\
&+ I \times \sum_{a,b=0}^{N-1} \mathcal{P}(\lambda_{SI} = a)\mathcal{P}(\lambda_{II} = a|\lambda_{SI} = b) \\
&\times \sum_{\imath=1}^{2} \mathcal{P}(E_\imath, \lambda_{SI})\Delta X(E_\imath, a, b) \ . \qquad (7.4)
\end{aligned}$$

Both the probability for the occurrence of an event and the change in the macroscopic variable can be expressed as second-order polynomials of the number of links of different types. Through the first summation, these polynomials turn into the corresponding first and second probabilistic moments. Below, indices of the moments denote whether the average was taken with respect to an S- or I-node.

$$\begin{aligned}
\Delta N_S &= \underbrace{-N_S \times \tau\langle\lambda_{SI}\rangle_S}_{E_3} + \underbrace{N_I \times r}_{E_1} \\
\Delta L_{SI} &= \underbrace{N_S \times \left(-\tau\langle\lambda_{SI}^2\rangle_S + \tau\langle\lambda_{SI}\lambda_{SS}\rangle_S\right)}_{E_3} \\
&+ \underbrace{N_I \times (r\langle\lambda_{II}\rangle_I - r\langle\lambda_{SI}\rangle_I)}_{E_1} - \underbrace{N_I\omega\langle\lambda_{SI}\rangle_I}_{E_2} \\
\Delta L_{SS} &= \underbrace{N_S \times -\tau\langle\lambda_{SI}\lambda_{SS}\rangle_S}_{E_3} + \underbrace{N_I \times r\langle\lambda_{SI}\rangle_I}_{E_1} + \underbrace{-N_I \times \omega\langle\lambda_{SI}\rangle_I}_{E_2} \\
\Delta L_{II} &= \underbrace{N_S \times \tau\langle\lambda_{SI}^2\rangle_S}_{E_3} - \underbrace{N_I \times r\langle\lambda_{II}\rangle_I}_{E_1} \ . \qquad (7.5)
\end{aligned}$$

The first moments, e.g. the average number of SI-links per susceptible node, can be directly calculated from the macroscopic variables: $\langle\lambda_{SI}\rangle_S = L_{SI}/N_S$. In contrast, the second moments cannot be deduced directly without making specific assumptions regarding the link distributions. We derive the mean-field equations here from node-level. For the original derivation of the mean-field theory using triplets following Keeling *et al.* [10], see App. B.

7.2.2 Assumptions for Second Moments

Two different second moments enter the equations of motion for our global variables the correlation between SS- and SI-links connected to an S-node $\langle \lambda_{SS}\lambda_{SI}\rangle_S$, and the second moment of SI-links connected to an S-node $\langle \lambda_{SI}^2\rangle_S$ The latter is very closely related to the variance in the distribution of SI-links $\langle \lambda_{SI}^2\rangle_S = \sigma_{SI}^2 + \langle \lambda_{SI}\rangle_S^2$

Let us begin with the correlation between SI and SS-links SI-links connected to a susceptible node R are created and destroyed if one of its neighbours say a node Q changes its status If node Q changes its status from infected to susceptible or vice versa neither of the status changes depends in any way on the surroundings of node R Furthermore, if R decides to rewire its connection to Q, then this decision is just as independent of R's remaining neighbours It is therefore reasonable to assume that no correlation between the number of SS- and SI-links of R exists We hence assume the second moment to be[2]

$$\langle \lambda_{SS}\lambda_{SI}\rangle_S \equiv \langle \lambda_{SS}\rangle_S\langle \lambda_{SI}\rangle_S \equiv \frac{2L_{SS}L_{SI}}{N_S^2} \tag{7 6}$$

The second moment of SI-links connected to an S-node is more difficult to estimate A variance is always positive definite and hence a lower bound for the moment exists with $\langle \lambda_{SI}^2\rangle_S \geq \langle \lambda_{SI}\rangle_S^2$ Such a closure would assume that all S-nodes have an identical neighbourhood This is unlikely, since even a system that was initially set up to fulfil this condition would show variations in nodes' neighbourhoods due to random fluctuations

The link distribution of SI-links in a random network can be estimated using assumptions regarding the variance Here, we use the common assumption that the variance is equivalent to the mean of the system We thus find

[2]Since every SS link has two ends ending in a S node a factor 2 has to be added

$$\langle \lambda_{SI}^2 \rangle_S = \sigma^2 + \langle \lambda_{SI} \rangle_S^2 = \langle \lambda_{SI} \rangle_S + \langle \lambda_{SI} \rangle_S^2 = \frac{L_{SI}^2}{N_S^2} + \frac{L_{SI}}{N_S} \tag{7.7}$$

Of course it is not given that these assumptions are fulfilled. In particular, the re-wiring mechanism works to separate the susceptible and infected nodes into different groups, leading to relatively high numbers of SS- and II-links. Recovering infected nodes will hence have nearly exclusively SI-links. This consequence contradicts our assumption of a random network, and might significantly alter the validity of our closure. We will hence investigate the validity of the assumption using computer simulations in the following chapters.

With equations (7.6) and (7.7) we can write down a closed set of equations, giving the expected resulting change in the macroscopic quantities during one time step δt. For our analytic discussion, we can however choose δt to be arbitrary small. This turns the difference into a differential, and we obtain a closed set of equations of motion.

$$\begin{aligned}
N_S \equiv \Delta N_S &= -\tau L_{SI} + r N_I \\
L_{SI} \equiv \Delta L_{SI} &= -\tau \frac{L_{SI}^2}{N_S} - \tau L_{SI} + \tau \frac{2 L_{SS} L_{SI}}{N_S} + 2 r L_{II} - r L_{SI} - \omega L_{SI} \\
L_{SS} \equiv \Delta L_{SS} &= -\tau \frac{2 L_{SS} L_{SI}}{N_S} + r L_{SI} + \omega L_{SI} \\
L_{II} \equiv \Delta L_{II} &= \tau \frac{L_{SI}^2}{N_S} + \tau L_{SI} - 2 r L_{II}
\end{aligned} \tag{7.8}$$

7.3 Long Time Limits

In the following, we will investigate the predicted behaviour of the system. We will attempt to answer questions such as what the final state of a system will be, or what parameters such a final state might depend on. To do so,

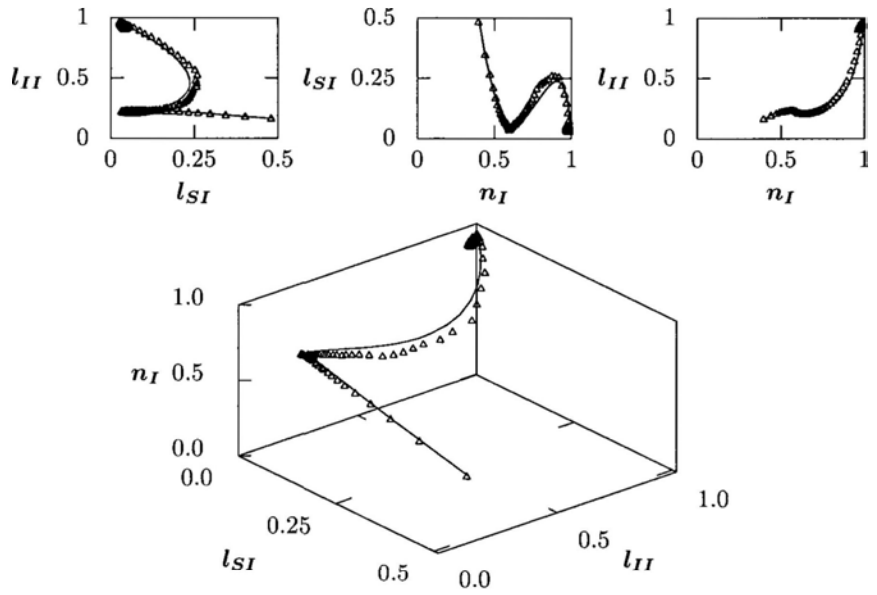

Figure 7.3: Exemplary trajectory of an adaptive SIS system. Parameters $\tau = 2.5r$, $\omega = 100r$, $N = 10000$, $k = 20$. Upper graphs: projections of the trajectory onto the respective planes. Solid lines for MFT curves, symbols for simulations.

we will first employ a fixed point analysis of our mean field theory [95], and compare the results with computer simulations in later chapters.

7.3.1 Fixed Point Analysis

Within a *phase space* spanned by the variables n_I, l_{SI} and l_{II}, the SIS system can access a prism inside the unit cube (the other half would require negative values of l_{SS}). Within this phase space, the trace of the system's configuration over time forms its *trajectory*.

Figure 7.3 shows an exemplary trajectory of an adaptive SIS system, obtained both from computer simulations and numerical solutions of the EOM. The system starts with $N_I = 4,000$ infected nodes in an otherwise random network of $N = 10,000$ nodes and mean degree $k = 20$. This corresponds to a scenario where 40% of the population become infected before the system reacts to the disease. The adaptive reaction then rapidly reduces the number of SI-links, thereby slowing down the dynamics significantly. However, the S-nodes become highly connected during this process and once these highly connected nodes become infected, the infection can spread very quickly. Finally, the trajectory of the mean-field equations converges towards a single point, while the simulation trajectory fluctuates around the same point. At this point, a stable portion of the nodes in a network is infected, creating an endemic state of the system.

In the studies of nonlinear dynamics, such points are commonly called attractive *fixed points*. The name 'fixed point' originates from Eq. (7.8), as all derivatives vanish at such a point. A system at exactly that point will not change over time. The word 'attractive' refers to an additional quality of such points, namely that systems anywhere within some small neighbourhood of such a point will be drawn towards it. We can further analyse the system by examining for which relations of parameters $\omega/r, \tau/r$, fixed points exists and what their properties are.

An obvious choice for a fixed point, both from the equations and from simple reasoning, is the point $n_S = 1, \quad l_{SS} = 1$. This is simply the fully healthy state in absence of a disease. It exists irrespectively of the choice of parameters ω and τ. Using computer algebra software[3] , two other fixed points can be found by setting the left side of equations (7.8) to zero. Depending on

[3]or a very lengthy calculation of a cubic equation

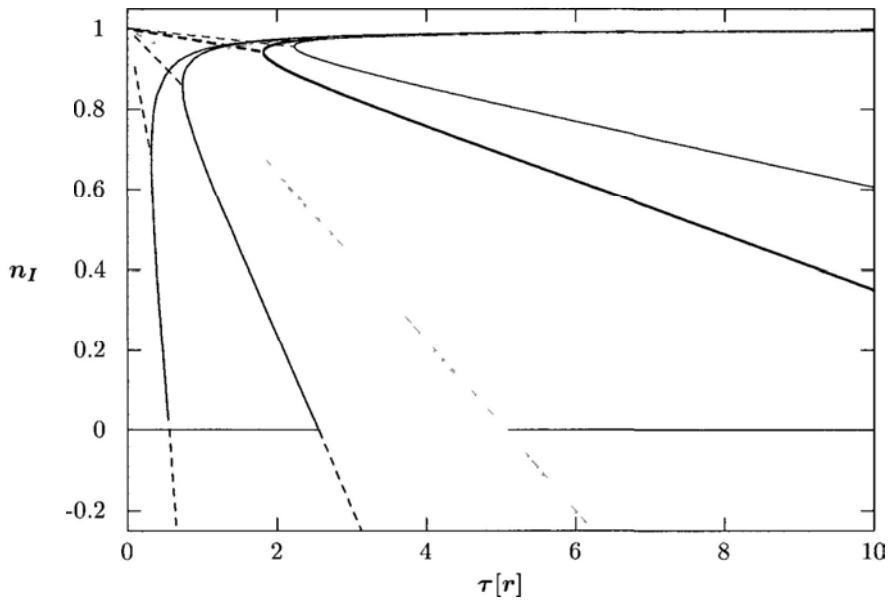

Figure 7.4: n_I-values of fixed points of an SIS system with $k = 20$ as a function of τ, for rewiring parameters $\omega = 10r$ (red), $\omega = 50r$ (blue), $\omega = 100r$ (green) and $\omega = 500r$ (purple). Lines are dashed where the fixed point has either negative or complex values.

the parameters, the other fixed points may not be real-valued quantities.

Figure 7.4 shows the n_I-values of all fixed points as a function of the contagiousness τ for various values of the rewiring parameter ω, both expressed in terms of the rewiring rate r. Generally, three fixed points are found: the aforementioned healthy state (which exists for any parameter combination), an endemic state with the majority of the nodes infected, and an intermediate fixed point whose n_I-value decreases with increasing contagiousness. The endemic and intermediate fixed points are complex for small values of τ and hence not applicable to our system. The n_I-value of the intermediate fixed point turns negative for higher values of τ, where it hence becomes irrelevant

for our system as well.

These fixed points can show different behaviour depending on the system parameters. Parameter sets at which fixed points emerge or change their behaviour are referred to as *bifurcations*. In the following, we will investigate these bifurcations by means of a stability analysis of the fixed points [96, 97].

7.3.2 Stability Analysis

By definition, the time derivatives of the macroscopic density variables $x \in \{l_{SI}, l_{II}, n_S\}$ vanish at a fixed point: $\dot{N}_\mathrm{S} = \dot{L}_\mathrm{SI} = \dot{L}_\mathrm{II} = 0$. However, if small fluctuations occur, for some fixed points the system's trajectory will always return to the fixed point (in which case we would call it an attractive fixed point). Just as well, it may not return but oscillate following closed loops, or it may move away towards some other fixed point. For systems with three dimensions or more, it may even continue to move without being attracted to any fixed point or ending in a closed loop [98].

The partial derivatives of $\dot{x}$ with respect to each density form the Jacobi matrix of the system: $(\mathcal{J})_{ij} = \frac{\partial \dot{x}_i}{\partial x_j}$. For the SIS system, the Jacobian is

$$\mathcal{J} = \begin{pmatrix} \frac{\partial \dot{l}_{SI}}{\partial l_{SI}} & \frac{\partial \dot{l}_{SI}}{\partial l_{II}} & \frac{\partial \dot{l}_{SI}}{\partial n_S} \\ \frac{\partial \dot{l}_{II}}{\partial l_{SI}} & \frac{\partial \dot{l}_{II}}{\partial l_{II}} & \frac{\partial \dot{l}_{II}}{\partial n_S} \\ \frac{\partial \dot{n}_\mathrm{S}}{\partial l_{SI}} & \frac{\partial \dot{n}_\mathrm{S}}{\partial l_{II}} & \frac{\partial \dot{n}_\mathrm{S}}{\partial n_S} \end{pmatrix} . \tag{7.9}$$

For a small displacement $\delta\mathbf{x}$ (i.e., a short vector in the phase space) against the fixed point, $\mathcal{J} \cdot \delta\mathbf{x}$ gives the initial direction of the resulting trajectory. If the eigenvectors of the Jacobian at the fixed point are linearly independent, its stability can be judged by the eigenvalues η_i of $\mathcal{J}$.

Let us for the moment assume real-valued eigenvalues. If all three values

are negative, then the fixed point is attractive, i.e., the trajectory will move closer towards the fixed point. If all eigenvalues are positive, then the fixed point is repulsive, i.e., the trajectory will move further away as soon as any displacement occurs. More common, however, are so called *bistable* fixed points where some eigenvalues are positive and some eigenvalues are negative. A system that is close to a bistable fixed point might hence be attracted towards the fixed point along the attractive eigenvector, but will ultimately be repelled towards the direction of the repulsive eigenvector.

Imaginary parts of eigenvalues represent a movement of the system orthogonal to the small displacement. Moreover, complex eigenvalues with a negative real part represent attractive spirals, while those with a positive real part represent expanding spirals. Hence, the imaginary part is not relevant for the stability analysis itself but rather describes the manner in which the trajectories are attracted towards or repulsed by the fixed point. A special case occurs when the real part vanishes, in which case a purely imaginary eigenvalue predicts stable closed loop oscillations around the fixed point.

Figure 7.5 shows the eigenvalues of the Jacobian of the endemic fixed point for a system with a high rewiring rate ω. At its emergence at τ_0, the fixed point is bistable: while eigenvalue η_1 is strongly negative, the other eigenvalues η_2 and η_3 are real positive. The fixed point changes its behaviour. At τ_1, the real parts of η_2 and η_3 are still positive, but an imaginary component emerges. Hence, the trajectories are now spiraling outward. At τ_2, the real parts of η_2, η_3 vanish and the trajectories would form stable closed loops. For larger $\tau > \tau_2$, all eigenvalues have negative real parts and the fixed point is hence a stable attractor. However, since the imaginary parts do not vanish, the trajectory will spiral towards the final state.

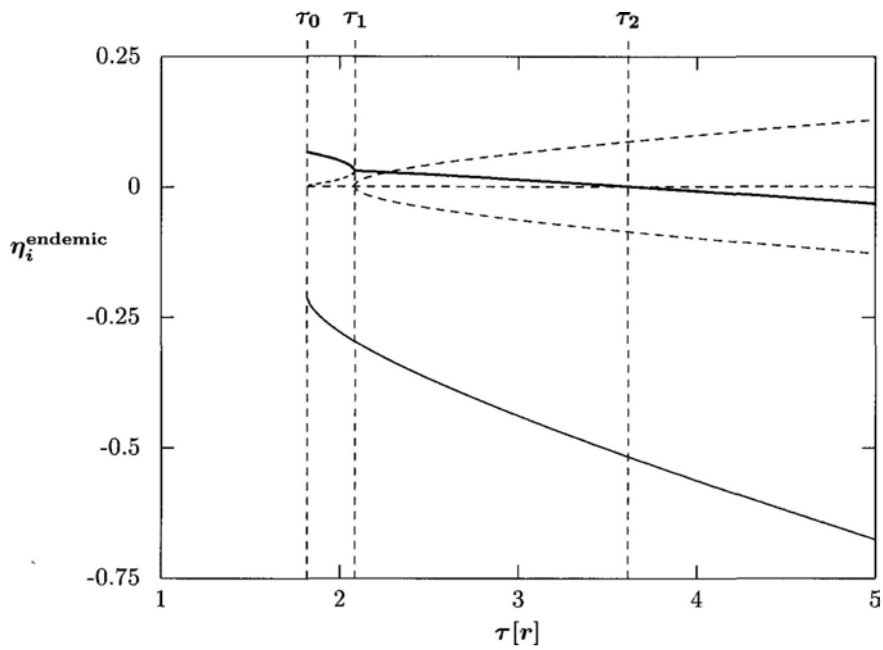

Figure 7.5: Eigenvalues η^{endemic} of the Jacobian of the endemic fixed point. Solid (solid-dashed) lines: real parts, dashed lines: imaginary parts. Parameters: $w = 300r$, $k = 20$.

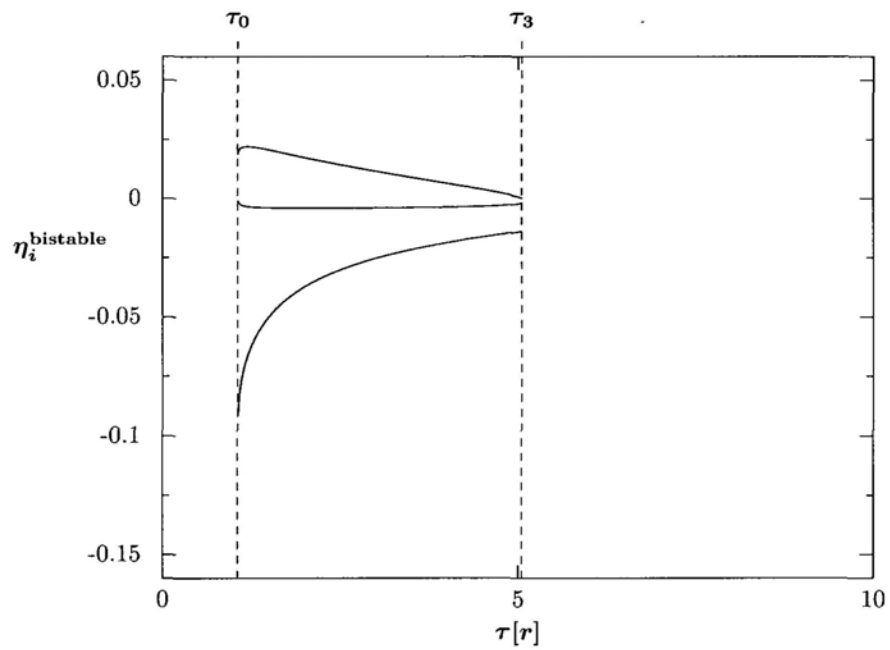

Figure 7.6: Eigenvalues η^{bistable} of the Jacobian of the bistable fixed point. Parameters: $w = 100r$, $k = 20$.

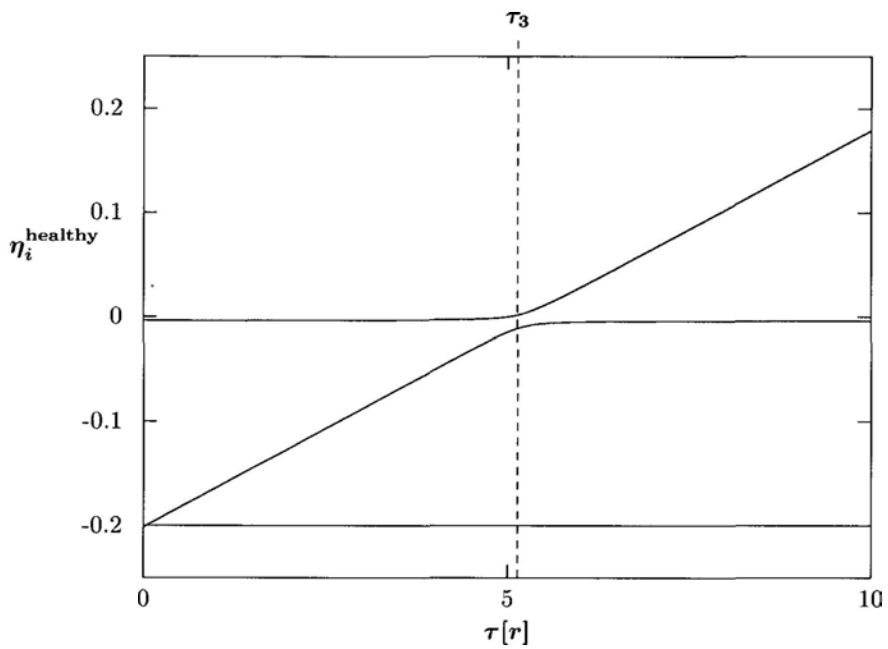

Figure 7.7: Eigenvalues η^{healthy} of the Jacobian of the healthy fixed point. The value of one eigenvalue was magnified by a factor 100 to make it visible (light green line). Parameters: $w = 100r$, $k = 20$.

Figures 7 6 and 7 7 show data from an otherwise identical system[4] with a lower re-wiring rate of $\omega = 100\tau$ Figure 7 6 shows the eigenvalues of the Jacobian of the intermediate fixed point Technically also a bistable fixed point, it has one real positive and two real negative eigenvalues over its entire interval of existence Figure 7 7 shows the eigenvalues of the healthy fixed point $I_{SS} = 1 \quad \iota = 0$ One eigenvalue here magnified by a factor 100 for clarity, is constant and real negative One other eigenvalue is also constantly negative but increases steadily with increasing τ until it converges against a very small negative value In contrast, the third eigenvalue does change its sign and becomes positive at the same point where the intermediate fixed point vanishes For higher values of τ, the healthy fixed point therefore itself changes from being attractive (for small τ) to bistable (for large τ) For larger τ there thus exists only one attractive fixed point any system not starting in a perfectly healthy state will end in an endemic state

Using this information, we can classify the expected behaviour of an adaptive SIS system For very small values of the contagiousness, only the healthy fixed point exists and is attractive Any disease introduced will definitively die out At a larger value $\tau = \tau_0(\omega)$, a bifurcation occurs and two other fixed points – the endemic fixed point and the intermediate fixed point – emerge Since neither of these fixed points is initially attractive again any disease introduced into the system will be overcome The transient dynamics of the system might however be affected by these fixed points, e g it might undergo expanding oscillations near the endemic fixed point In particular, for some value $\tau > \tau_1(\omega)$, trajectories swiping close to the endemic fixed point may exhibit outward spiralling behaviour At $\tau = \tau_2(\omega)$, trajectories in small neighbourhoods of the endemic fixed point can form closed loops, and the system might not recover

[4]The different choice of ω was made for purely illustrative purposes since unstable healthy fixed points occur only for much higher values of τ at $\omega = 0\,6$

to the healthy state, but will not end in a single endemic state either For even higher values $\tau > \tau_2(\omega)$, the endemic fixed point becomes attractive Depending on the initial infection level, the system may recover from a disease or it might end in a final endemic state with a part of the population being infected at all time In this later case, the approach to the final state will occur in oscillations Finally for $\tau > \tau_3$, the intermediate fixed point vanishes and the healthy fixed point becomes bistable itself Should any disease be introduced into the healthy system it will spread over the system and the system will definitively approach the endemic state The approach itself is still oscillatory However for extreme cases $\tau > \omega$ the approach will become straight again The system then acts again like a non-adaptive network above its infection threshold

With this information, we can classify the regime of an SIS system, depending on its parameters Figure 7 8 shows the three main regimes – healthy, with any disease dying out, bistable with the final outcome depending on the system's initial conditions and endemic, with any initial infection becoming permanent – as a function of the infection and rewiring rates τ and ω The healthy regime is characterised by only the healthy fixed point being stable The bifurcations occurring at τ_0 and τ_1, namely the emergence of an unstable endemic fixed point and the onset of oscillatory dynamics in the vicinity of this point, do not affect the final outcome The bistable regime is characterised by both the healthy and the endemic fixed points being stable The final outcome here will depend on the initial configuration of the system At last the endemic state is characterised by only the endemic fixed point being stable The healthy fixed point still exists but is unstable Any perturbation, i e , the introduction of a disease into the system will spread over the system

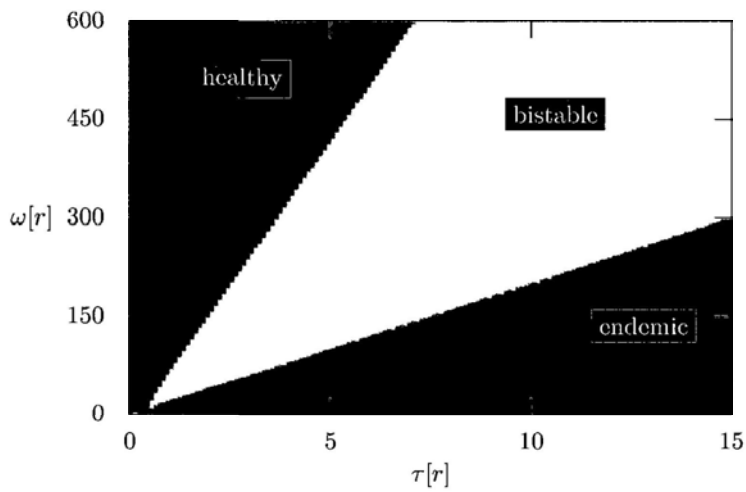

Figure 7.8: Different regimes of an adaptive SIS system: healthy (blue), bistable healthy/endemic (yellow), and endemic (red). Additional sub-regimes are shown for the healthy and endemic states: only healthy fixed points (dark blue), unstable endemic fixed points (lighter blue), unstable endemic fixed points with oscillatory behaviour (turquoise), only endemic fixed points are attractive, with an oscillatory approach (purple), and without oscillatory approach. (red)

7.4 Comparison with Computer Simulations

To test the validity of the previous theoretical analysis, we will discuss various results of Monte-Carlo-simulations of the model. For all simulations, a network consisting of $N = 10000$ nodes with mean degree $k = 20$ was used. The recovery parameter was set to $r = 0.002$. All other parameters will be given together with the corresponding results.

7.4.1 Infection Spreading Prior to Adaptive Reactions

In the bi-stable regime, a disease introduced into the system can lead to an endemic state, but may die out as well, depending on the initial conditions. In what follows, we will therefore investigate the initial conditions leading to either state, how they can be distinguished, and whether or not our theoretical expectations agree with simulation results.

From an epidemics point of view, it is of particular interest to define a critical fraction of initially infected nodes $n_I^{(\mathrm{crit})}$. The idea is that if a disease is discovered before such a threshold is reached, the adaptive counter-measures will be successful in suppressing the spreading of the disease. If the adaptive reaction only begins when more than $n_I^{(\mathrm{crit})}$ nodes are infected, the system will end in an endemic state.

Previously, Gross *et al.* used the n_I-value of the intermediary fixed point $n_I^{(\mathrm{imd})}$ as a measure for $n_I^{(\mathrm{crit})}$ [92, 7]. However, this method can produce erroneous results, as we are going to show.

At first, the initial state of the network has to be discussed. Except for pathological cases, any macroscopic coordinate within the accessible phase space $0 \leq n_I \leq 1$, $0 \leq l_{SI} \leq 1$, $0 \leq l_{II} \leq 1 - l_{SI}$ can be represented by

a simulation network. However, for a real system, not every configuration is equally likely to occur. If we assume a fraction n_I of randomly chosen individuals to be infected, the link configuration of the system can be easily deduced. We can assume that every link has a chance of n_I to have an infected node and $1 - n_I$ to have a healthy node at either end. Hence, the mean configuration of a randomly infected network is

$$\begin{aligned} l_{SI} &= 2n_I(1 - n_I) \\ l_{II} &= n_I^2 \,. \end{aligned} \tag{7.10}$$

Within the phase space spanned by the the variables n_I, l_{SI} and l_{II}, these randomly infected networks form a one-dimensional manifold. The question remains, however, whether the initial state of an infection on an adaptive network can be assumed to be of this random type.

Typically, the network's configuration would initially represent the connections between individuals before the disease is introduced into the system. At this time, all individuals are healthy and susceptible. A disease is then introduced from outside, typically through the infection of one or several individuals, e.g., travellers returning from a trip to a country where the disease is endemic. In the following, the disease would spread unnoticed. For an adaptive reaction, the disease's symptoms have to be known, and the individuals need to be aware of the risks in associating themselves with infected individuals. Until this happens, the disease will spread through the so-far static network, until, at some time, the adaptive reaction begins. We assume here that the adaptive reaction begins abruptly, i.e., $\omega = 0$ for $t < 0$ and $\omega = const > 0$ for $t > 0$, for a discussion of time-dependent ω see [93]. The configuration of the network at time $t = 0$ is what has to be used as the initial conditions of the adaptive SIS network.

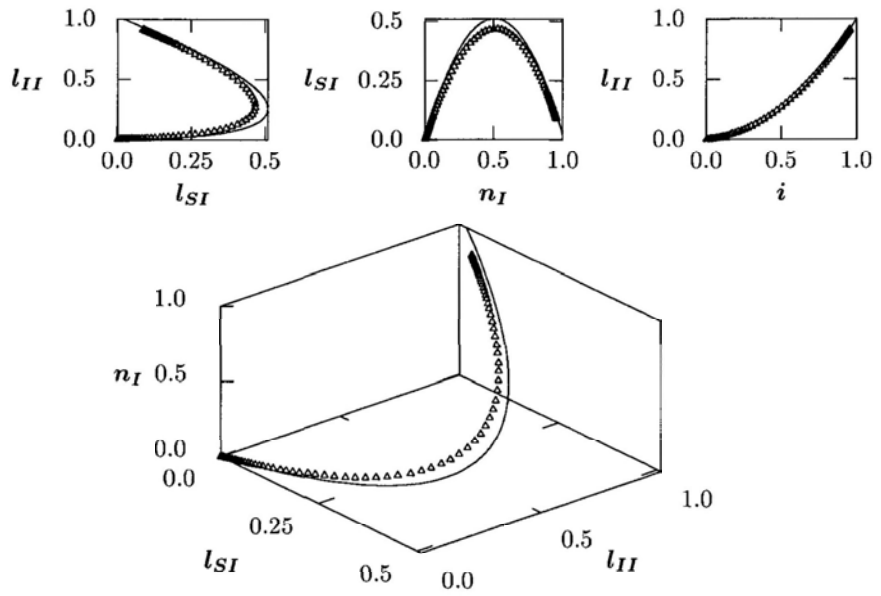

Figure 7.9: Spreading of an SIS-type disease (symbols) on a static random network above the infection threshold (Eq.(7.1)), with projections on the respective planes. Lines give the subspace of a random infection as defined in Eq. (7.10).

Figure 7.9 shows the phase space trajectory of an SIS-type infection spreading on a static network. The disease was introduced into the system by randomly infecting 1% of the nodes. Hence, the initial conditions of the static network fulfil Eq. (7.10) by default. However, the states of a spreading epidemic are not always identical to that of random infections. Small deviations occur, here noticeable mostly in slightly fewer SI-links than expected. This can be understood since a spread on a network has to follow the causality principle: Nodes can only infect nodes in their own neighbourhood, which in return includes those nodes through which they contracted the infection, effectively reducing the number of susceptible neighbours. Furthermore, any topologic relationships, i.e., overlapping neighbourhoods, can affect the spread of the disease. If the disease initially spreads to such a cluster, overly many II-links will be formed, while such a cluster has only SS-links before this happens. Such topological effects are much smaller for random networks than for lattice structures, however, they are sufficient to cause the small deviations observed here. Given that the overall state of this epidemic process is always very close to the subspace of randomly infected networks, we will in the following take the expected initial configuration of a network at the onset of the adaptive reaction from this subspace.

7.4.2 Separatrix and Basins of Attraction

Neither chaotic behaviour nor closed loops occur here. Hence, the phase space can be divided into basins of attraction of the attractive fixed points. The surface that separates them is commonly referred to as the separatrix. For the present system, the separatrix is a $2D$-manifold in the l_{SI}, l_{II}, n_I-space. For otherwise identical systems with n_I-values above the separatrix, the trajectories will converge towards the endemic fixed point. For n_I-values below the

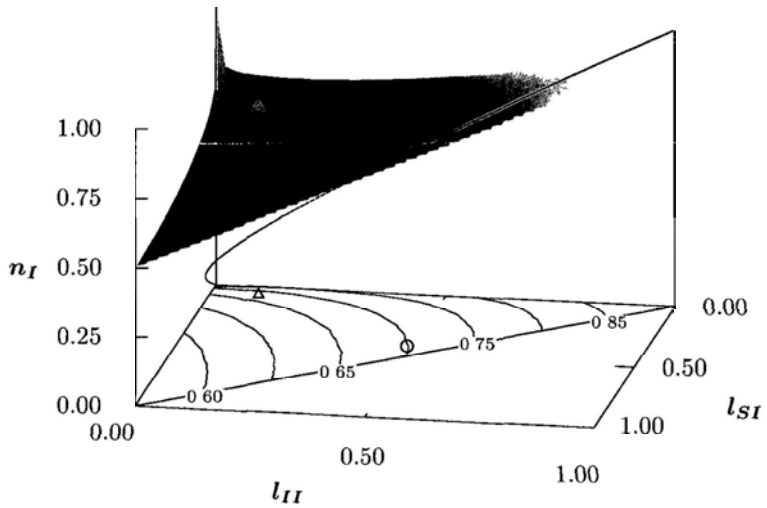

Figure 7.10: Separatrix of an SIS system with $N = 10000$, $k = 20$, $\tau = r$ and $\omega = 50r$. The blue line gives the subspace of randomly infected systems. The intersection with the separatrix marked by the blue circle. The black triangle gives the coordinates of the intermediate fixed point. The bottom shows a projection of the fixed point, the intersection point, as well as a contour representation of the separatrix. Such contours are in the following used in Fig. 7.11

separatrix, the trajectories will converge towards the healthy fixed point and the disease will die out. Several methods exist for calculating separatrices. For the present system, repeated iteration of the equations of motion is perfectly sufficient to obtain the separatrix.

Figure 7.10 shows the separatrix exemplary for a system in the bistable regime. Generally, the n_I-values of the separatrix vary between approximately $n_I = 0.5$ for a system in which nodes of the same type are never connected, and $n_I = 0.9$ if connections only exist between infected nodes ($l_{II} \approx 1$). For $l_{SS} = 1$, i.e., only connections between susceptible nodes, the infection can

never spread all infected nodes are already isolated and will remain so even after they recover Rewiring does not occur in this case since no SI-links exist

For a given set of system parameters τ, ω, r and k, the fixed points are given by the roots of Eqs (7 8) For the case in Fig 7 10, the coordinates of the intermediate fixed point are $n_I^{(\mathrm{imd})} = 0\,675049$, $l_{SI}^{(imd)} = 0\,067505$ and $l_{II}^{(imd)} = 0\,103869$ The configuration corresponding to these coordinates consists of two subnetworks network of highly connected susceptibles and sparely connected infected nodes, with only very few links connecting the groups The mean degree of susceptible nodes in such a network is $k_S \approx 51$, while $k_I \approx 4$ However, such a configuration is very unlikely to occur while the disease is spreading on a network On the contrary, if such subnetworks of highly and sparsely connected nodes existed, the infection would in all likelihood spread much faster on the highly connected network and thus invert the configuration described by the intermediate fixed point's coordinates In fact, the configuration of the intermediate fixed point is so improbable that it is not even achieved once the adaptive rewiring mechanism is active

The subspace of randomly infected networks is shown as a blue parabola Its intersection with the separatrix, shown as a blue circle gives the threshold above which a randomly infected network would enter an endemic or susceptible state Since, as discussed before, the spreading of an infection on a static network very closely resembles a randomly infected network, we consider the n_I-value of the intersection point to be a more appropriate criteria for $n_I^{(\mathrm{crit})}$ The value is here $n_I^{(\mathrm{ints})} = 0\,699300$, which is different although reasonable close to the n_I–value of the intermediate fixed point $n_I^{(\mathrm{imd})}$ This leaves the question whether it is common for the n_I-values of the intersection and the intermediate fixed points to differ In what follows, we will try to answer

this question Furthermore, we will discuss whether any such error is significant compared to deviations between the MFT's separatrix and the separatrix observed in computer simulations

Figure 7 11 shows contours for a set of separatrices, each including both the randomly infected system's subspace, the intermediate fixed point, and the intersection point Notably, the intermediate fixed point always lies in the proximity of the axis $l_{SS} = 1$ corresponding to the improbable configuration of highly connected subnetworks mentioned above The intersection point, on the contrary always corresponds to a random network configuration Accordingly, even if the n_I-values of intersection point and intermediate fixed point are similar the other two variables l_{SI} and l_{II} differ significantly

To judge the relevance of these deviations, we compare the theoretically predicted separatrix with the results of Monte Carlo simulations of the model In order to do so we set up a simulation system for a set of parameters $r, \omega, \tau, n_I, l_{SI}, l_{II}$ as follows Out of a total of $N = 10,000$ nodes $N_I = n_I N$ are set to be initially infected Afterwards two susceptible (or two infected, or one susceptible and one infected each) nodes are randomly chosen and a link between them is established until a total of $L_{SS} = (1 - l_{SI} - l_{II})Nk/2$ (or L_{II}, or L_{SI}) links are created Creating multiple links between two nodes or linking a node with itself is not allowed Following such a method network configurations corresponding to nearly every set of parameters n_I, l_{SI}, l_{II} can be created For each set of parameters an ensemble of 50 systems is created Each system then evolves according to the adaptive SIS dynamics If for a given combination of l_{SI} and l_{II} the n_I-value is chosen low enough, all systems will finally result in a healthy state Equivalently a large n_I-value will result in all 50 systems entering the endemic state By varying the initial value of n_I, we can trace out the transition range of a simulated epidemic system The

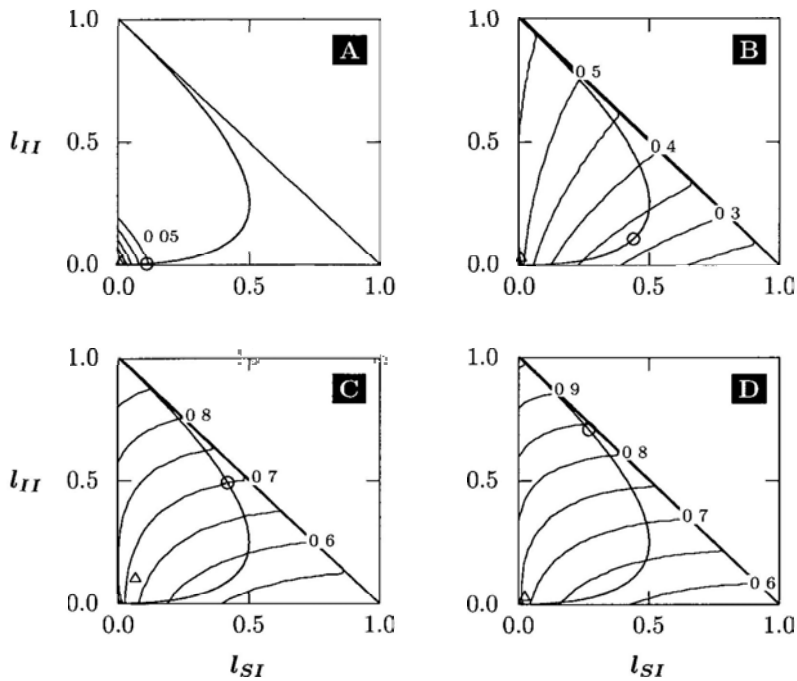

Panel	w	τ	$n_I^{(imd)}$	$n_I^{(ints)}$
(a)	0.1	0.004	0.2356	0.0569
(b)	0.4	0.010	0.5236	0.3262
(c)	0.1	0.002	0.6750	0.6993
(d)	0.4	0.006	0.7294	0.8403

Figure 7.11: Contours of separatrices for several systems, all shown together with the corresponding fixed point (black triangle), the randomly infected system's subspace (blue parabola) and the intersection point (blue circle). The table lists the n_I-values of both intermediate fixed point and intersection point.

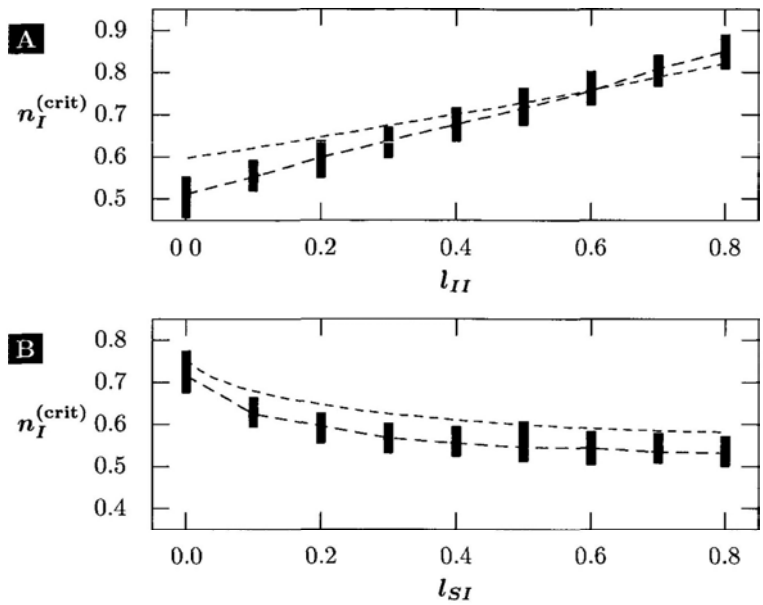

Figure 7.12: Simulation transition ranges and MFT separatrix for a set of values in the planes $l_{SI} = 0.2$ (A) and $l_{II} = 0.2$ (B). Color bars indicate the percentage of systems ending in an endemic state, going from 0% (black) over 50% (blue) to 100% (red). The blue line connects the n_I-values where a system is as likely to end in either state. The red dashed line gives the cut trough the separatrix.

separatrix is expected to lie somewhere within this transition range.

For a quantitative comparison, we cut the parameter space of Fig. 7.10 along the planes $l_{SI} = 0.2$ ($l_{II} = 0.2$) and vary l_{II} (l_{SI}) accordingly. The cut through the separatrix is shown as a line in Fig. 7.12. For several values of l_{II} (l_{SI}), the transition range of the simulation systems is probed. For the cut at $l_{SI} = 0.2$, shown in figure 7.10(A), the separatrix falls into the transition range except for very large or very low l_{II}-values. For the cut at $l_{II} = 0.2$, the separatrix always lies above the simulation transition range, but typically

only by a small margin of $\Delta n_I \leq 0.05$. These deviations are comparably small, lending confidence to the overall accuracy of the MFT separatrix.

To get a better understanding of the relation between the accuracy of the MFT prediction and the accuracy of the intermediate fixed point as a representative of $n_I^{(\mathrm{crit})}$, we also compared the simulation transition range for random systems with theory predictions. To do so, we set up simulation systems as described above, with the l_{SI} and l_{II} coordinates given by Eqs. (7.10). We compared the transition range with the intersection point and the intermediate fixed point. The results are shown in Fig. 7.13 for a range of τ, for $\omega = 0.4 = 200r$ and $r = 0.002$. While the $n_I^{(\mathrm{crit})}$-values given by the intersection point nearly perfectly coincide with the center of the transition ranges, the deviations between the intersection point and the intermediate fixed point are very pronounced over most part of the bistable range.

One remaining question is how the transition ranges, shown in Figs. 7.12 and 7.13, are influenced by the number of agents in the system. Generally speaking, they are caused by random fluctuations that are intrinsic Monte Carlo simulations of the model. The dependence of these transition ranges on the system size is shown in figure 7.14 for a range of $10^3 \leq N \leq 10^5$. The relative importance of the fluctuations decreases with increasing system size, leading to smaller transition ranges for large systems. For very large systems, the n_I-value of the intersection point $n_I^{(\mathrm{ints})}$ is not anymore within the transition range, owing to model features not captured by the mean-field theory. However, the difference between $n_I^{(\mathrm{imd})}$ and the simulation transition point exceeds that between $n_I^{(\mathrm{ints})}$ and the simulation transition point by a factor of more than five.

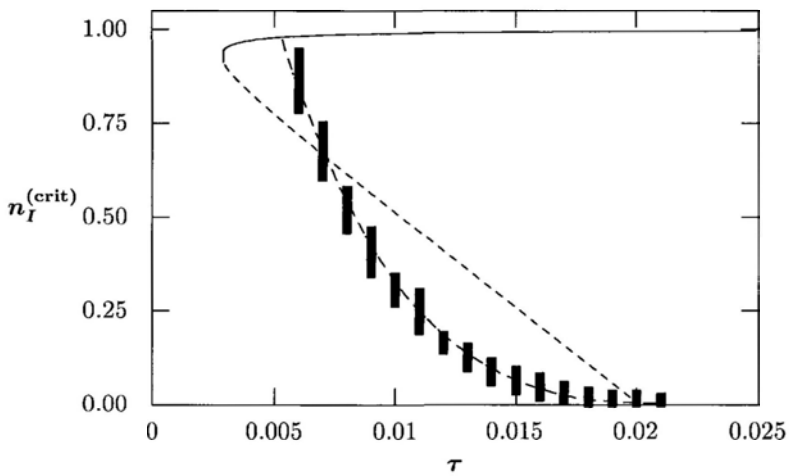

Figure 7.13: Simulation transition ranges (colored bars), intersection point (blue line) and intermediate fixed point (red dashed line) of randomly infected networks for a range of contagiousness parameters τ. Colours indicate how many (0% (black) to 100% (red)) of the systems with such configurations enter an endemic state.

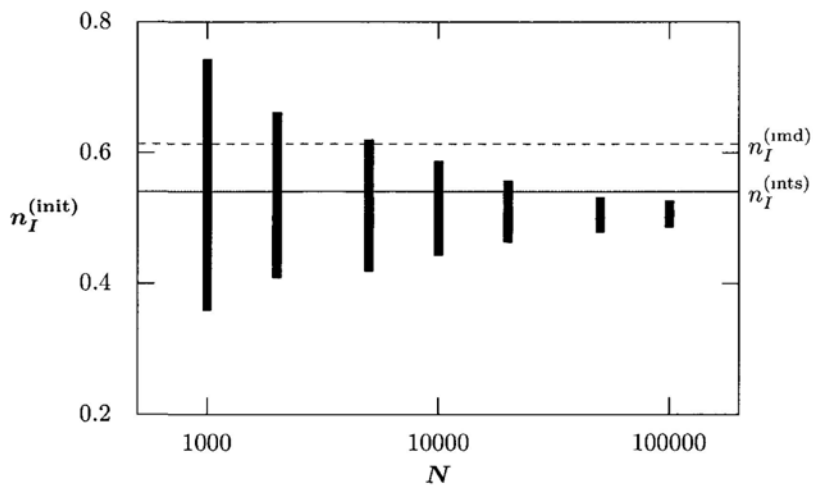

Figure 7.14: Size dependence of the transition range. For a fixed set of parameters ($r = 0.002$, $\tau = 0.008$, $\omega = 0.4$, $k = 20$), ensembles of systems of different size are created and their transition range is traced. The colours indicate the percentage (black: 0%, red: 100%) that enter an endemic final state. The infected fractions of the unstable fixed point $n_I^{(imd)}$ and of the intersection point $n_I^{(ints)}$ are shown for comparison.

7.4.3 Conclusion

We have introduced and discussed the adaptive SIS model as an example of co-evolving networks In the first part of this chapter, we have focussed on reproducing existing results, in order to make sure that both our understanding of the model and our implementations are correct In the section following Ch 7 4, we have built upon these results by discussing how a meaningful criterion for the critical initially infected fraction $n_I^{(\mathrm{crit})}$ can be found The key results of this analysis can be summarised as follows The intermediate fixed point is an unsuitable criterion for $n_I^{(\mathrm{crit})}$, as it corresponds to highly unusual network configurations The overall agreement between mean-field theory and simulations, illustrated by comparing the separatrix values for different configurations with the transition point of the simulation, is very good (see Figs 7 12-7 13) We therefore propose the n_I-value of the intersection point between the separatrix and the subspace of randomly infected networks as a new criterion for $n_I^{(\mathrm{crit})}$

Based on these results, various options exist that still need to be investigated In particular, the behaviour of a system with a rewiring process that follows preferential attachment should be investigated As epidemic thresholds are absent in scale-free networks [88, 89], it would be very interesting to know whether or not a disease could be efficiently suppressed if the rewiring process itself creates such a scale-free network

Chapter 8

Adaptive Snowdrift Game Networks: Introduction

In this chapter, we will introduce the concept of evolutionary games as a type of dynamic models on networks. We will discuss some general features of such games, and introduce the so-called evolutionary Snowdrift Game in detail. In Sec. 8.2, we will review some results regarding the Snowdrift Game as a dynamic model on networks. In Sec. 8.3, we will propose a new, coevolutionary snowdrift game model, the Dissatisfied-Adaptive Snowdrift Game, which allows nodes to adapt their environment as a reaction to unfavourable outcomes of a game trial. Finally, we will discuss simulation results and a mean field theory for this model. The results presented in this chapter were published in Ref. [9].

8.1 The Evolutionary Snowdrift Game and Other Competitive Games

Imagine the following situation: A country road in winter has been blocked by a snow drift, hindering drivers from both directions to get to their destination. To get to his destination. a driver would have to shovel the snow away, which is a laborious task he would like to avoid. If he is lucky, someone, on the other side of the snowdrift, is stuck as well and will do the work for him. If he is unlucky, however, the other driver is just as uncooperative, and neither of them will get to their destination. Although it appears reasonable that both drivers share the workload, a lack of information about what is going on on the other side of the drift means both drivers have to make their decision – to *cooperate* and shovel or to wait inside the car and thus *defect* – all by themselves [99, 100].

In game theory, this scenario is formalised as follows. If he manages to get through the snowdrift, each driver will obtain a benefit b. At the same time, shovelling away the entire snow drift comes at a labour expense c. The cost can be shared equally by both players, or carried by a single shovelling player alone. The cost is always smaller than the benefit $c < b$. since otherwise no player would consider removing the snowdrift all by himself. Commonly, the decision to or not to shovel is identified with characters related to another game (the prisoners dilemma, see below): A *cooperator* (symbolized by the vector $\mathbf{e}_C = (1,0)^T$) is willing to do his share of the workload and shovel. while a *defector* ($\mathbf{e}_D = (0,1)^T$) prefers to let others do the work and hence waits inside his warm car. With these definitions, the *payoff matrix*, defining the payoff $\varrho(A,B)$ of a player of type A playing against an opponent of type B, is

$$\underline{\mathbf{P}} = \begin{pmatrix} R & S \\ T & P \end{pmatrix} = \begin{pmatrix} b - c/2 & b - c \\ b & 0 \end{pmatrix},$$
$$\varrho(A, B) = \mathbf{e}_A^T \underline{\mathbf{P}} \mathbf{e}_B \tag{8.1}$$

The payoff is commonly normalised by setting the mutual cooperation-payoff to $R = 1$. By introducing the temptation parameter $r = c/(2b - c)$, we can then write the parameterised payoff matrix as

$$\underline{\hat{\mathbf{P}}} = \begin{pmatrix} 1 & 1 - r \\ 1 + r & 0 \end{pmatrix} \tag{8.2}$$

Game theory uses a variety of such games, each offering participants the choice to either cooperate or defect. The game is characterised by the values of the payoff matrix, i.e., the mutual cooperation payoff R, the mutual defection payoff P, and the cooperator versus defector payoffs S and T. The ranking of these payoffs is of high importance to the choice of a strategy when playing such a game. The Snowdrift Game (SG) generally refers to a payoff ranking $T > R > S > P$, which is a more general definition than the one we use here. For the Snowdrift Game in general, the excess benefit of the defector does not have to be identical to the excess cost of a cooperator in a CD-situation. The SG ranking means no optimal choice exists for a single player playing one single round. If his opponent cooperates, defecting offers an additional benefit r, but if the opponent is a defector himself, the player will not receive any payoff unless he chooses to cooperate. Hence, the Snowdrift Game is often also referred to as a social *dilemma*. Alternatively, other rankings result in different games. For example, the case of $T > R > P > S$ became widely known as the Prisoner's Dilemma (PD) [101, 102, 103]. Here, for both choices of the opponent's action, defecting always yields higher payoffs. Consequently, any single-round PD game played by two rationally acting agents will always

result in both agents defecting and therefore obtaining payoff P. This is a less-than-perfect choice for both players, since mutual cooperation could offer a higher benefit R to both players. A third widely-used ranking is the Stag-Hunt Game (SG) with $R > T > P > S$, originally discussed by Rousseau [104]. It is the most cooperation-promoting scenario among the three games, since mutual cooperation offers the highest benefit R to both players. However, mutual defection P is more beneficial than being the exploited cooperator obtaining S. Hence, even in this case cooperation is not an obvious choice [105, 106, 107, 108].

Like the Snowdrift Game, the other two model paradigms are also social dilemmas. They confront the player with a situation in which there is no definitive winning strategy. All have been used extensively in research on the emergence of cooperation. Generally, cooperation benefits the society but comes at a cost to the cooperator. Hence, the question arises why cooperation occurs at all. The impact of several factors on the emergence of cooperation has been investigated.

To investigate such scenarios on a population, dynamical rules have been specified for a group of agents playing such games against each other. While N-person competitions have been defined [109], the most common scenarios involve two-player interactions. In such a case, two connected agents play against all of their neighbours respectively. The outcomes of the games are determined by each player's current status, i.e., to cooperate or to defect. Afterwards they compare their average payoffs. The likelihood of one player adopting his neighbour's status will then be determined by the difference of their payoffs. In the most common cases, the player with the smaller payoff will be more likely to adopt the status of the more successful player, in an attempt to improve his fitness. Such dynamics are commonly referred to as evolutionary games.

8.2 The Snowdrift Game on Networks

Originally, the Snowdrift Game dynamics were defined as a dynamic model on a well-mixed network, i e a system where all nodes are in contact with each other, or at least where the composition of every node's neighbourhood resembles the composition of the entire system For such a system, cooperation will vanish for an evolutionary Prisoner's Dilemma game [110], since a defector will in every environment receive payoffs superior to those of a cooperator On the contrary, cooperation survives in case of the evolutionary Snowdrift game, since agents obtain no payoff in case of a system consisting solely of defectors A single cooperator, introduced into such a system will receive a benefit and hence spread its strategy until a fraction $f_c^{\infty} = 1 - r$ is cooperative At this point, an equilibrium is reached [9]

Instead of playing evolutionary games on well-mixed networks, spatial structures such as lattices can significantly change a game's dynamics Under such circumstances, cooperation can exist even in an evolutionary PD scenario [101] However, lattice structures may not represent human relationships very well They generally imply strong correlations between the neighbourhoods of connected nodes, which are not necessarily fulfilled for human relations Furthermore, the interfaces between clusters of nodes on a lattice have the form of surfaces i e nodes behind the surface have no contact with nodes of the other type Many effects observed for evolutionary games on lattices originated in such surfaces between clusters of cooperators and defectors The small-world effect observed in real-world networks [111] effectively removes such surface effects since some connections will reach far outside an otherwise closed domain Consequently, the dynamics of evolutionary games on complex networks with real world properties were investigated as well A comprehensive review of the

effects of the underlying graphs on evolutionary games can be found in [112]

However even such real-world complex networks do not offer a suitable environment to investigate human interactions like competitive situations Obviously, the scenarios mentioned lack a common fate that a determined defector will face sooner or later being abandoned by its peers Indeed, social networks between humans are typically not static Instead a network's links change frequently (compared to the time scale of introducing new and removing old agents) and often in response to interactions between the participants Hence, evolutionary dynamics need to be defined for both the game model and the underlying network If the dynamics are interdependent, i e , if the evolution of the game model depends on the underlying network and the evolution of the underlying network depends on the status of the game model, we refer to them as *co-evolving dynamics* However, the definition of rules for such dynamics is far from trivial Such rules may depend on the single individual or even on the single individual's current mood This makes the definition of rules more difficult than, for example, the definition rules for epidemic dynamics Furthermore, the adaptive co-evolutionary rules must not by themselves promote cooperation i e the ability to change their environment should not by itself destroy the dilemma as such

Interaction between the evolution of the network and that of the dynamic model can take many forms such as interdependence between the network growth and the game evolution [113] or diffusion on a diluted lattice as a reaction to the game s dynamics [114] The most common approach is the direct re arrangement of an agent s neighbourhood as a consequence of the evolutionary game model Such rearrangement can be stochastic i e links can be randomly created and destroyed following creation and annihilation rates

that, in turn, are depending on the game model. Such approaches were introduced by Pacheco *et al.* [115] and Zimmermann *et al.* [116] for the Prisoner's Dilemma. Alternatively, one agent can actively rearrange its neighbourhood as a consequence of a two-player game that it was involved in [117, 118]. For a bi-directional network with links of uniform weight, such an adaption is commonly realised by one agent cutting a link to a neighbour and rewiring to another agent.

A comprehensive review of coevolutionary games was recently published by Perc and Szolnoki [119].

8.3 The Dissatisfied-Adaptive Snowdrift Game

As an example of the influence of co-evolutionary dynamics on the emergence of cooperation, we will in the following discuss the mechanisms of the Dissatisfied-Adaptive Snowdrift Game (DASG). The DASG is a coevolutionary competitive game on a complex network. Agents occupy the nodes of a bidirectional network, and can alter it by breaking connections to their neighbours and establishing connections to other nodes in the network.

8.3.1 Model

The underlying ideas of the Dissatisfied-Adaptive Snowdrift Game are simple. We assume that every agent, no matter whether it is a cooperator (C-node) or defector (D-node), wants its neighbours to be C-nodes since this will maximise its payoff. Playing against a defecting neighbour leaves the agent dissatisfied, and it will consequently react. Two kinds of reactions are possible,

either switching its own strategy or cutting their connection and rewiring to another agent

In detail, the rules of the model are specified as follows (see overview in Fig 8 1) Initially, the nodes form a random network of N nodes with an average of k neighbours, i e , a mean degree k At any time, every node has an internal status or character that determines its action during the next round of the game, i e , to defect or to cooperate Initially these status are randomly assigned according to some predefined initial fraction of cooperation f_c^i i e , $N_C = f_c^i \times N$ randomly chosen nodes are set to be cooperators while the remaining $N_D = (1 - f_c^i)N$ nodes are initially defectors

We assume node-driven dynamics, i e any node will at random encounter a competitive situation (or *trial*) with identical frequency ω This is important since all nodes have identical influence in the system's evolution In contrast, in link-driven systems like the previously discussed adaptive SIS epidemic network, high-ranking nodes with many neighbours are pivotal to a disease's spreading while low ranking nodes have a negligible influence

For a trial, a single node is randomly chosen, and itself picks one of its neighbours at random It then plays one round of the snowdrift game against this neighbour We will hereafter refer to the first node as the *player* and to its randomly chosen neighbour as the *opponent* If the player is of character A and the opponent of character B, then the (dis)satisfaction S of the player can be expressed through the difference in the payoff it obtained and the payoff it would have obtained if the opponent had been of opposite character $\overline{B}$

$$S(A, B) = \varrho(A, B) - \varrho(A, \overline{B}) \tag{8 3}$$

Obviously S is positive if the opponent chose to cooperate ($B = C$), and

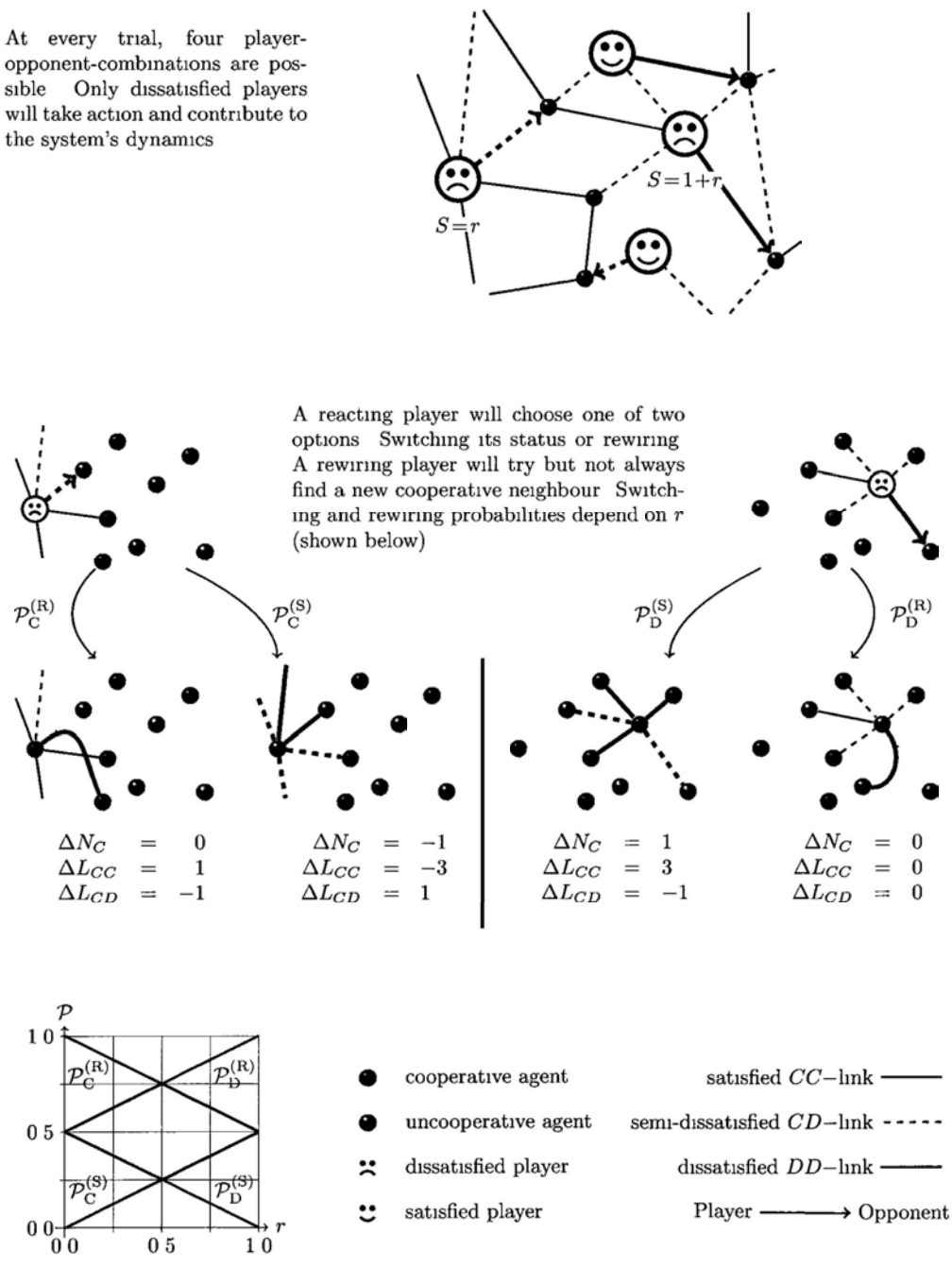

Figure 8.1· Overview of the rules of the Dissatisfied-Adaptive Snowdrift Game

negative if the opponent chose to defect ($B = D$). For the latter case, the player will be dissatisfied and hence choose to take one of two possible actions: To switch its status from A to $\overline{A}$, or to cut the link to its opponent and rewire to another randomly chosen node. Importantly, the character of this other node is not a-priori known to the player. Hence its chances to improve its situation by adding another cooperator to its neighbourhood are determined through the overall composition of the system. If the system consists nearly entirely of defectors, the chance to rewire to a cooperator is very low.

The dynamics of the model are determined by the definition of the probabilities for a node of type A, dissatisfied after playing against defector, to either rewire or switch its character. Four different events can occur: a C-node switches (CS), a C-node rewires (CR), a D-node switches (DS), or a D-node rewires (DR). We denote the respective probabilities by $\mathcal{P}_C^{(S)}$, $\mathcal{P}_C^{(R)} = 1 - \mathcal{P}_C^{(S)}$, $\mathcal{P}_D^{(S)}$ and $\mathcal{P}_D^{(R)} = 1 - \mathcal{P}_D^{(S)}$. We require these probabilities to fulfil certain conditions:

1. They must reflect a rational choice, i.e., a rational agent should believe that such actions improve its fortunes.

2. They should be functions of the disappointment of the player, and thus of the temptation parameter r. However, factors outside the scope of a single agent (such as the overall composition of the system) should not influence its decision.

We hence define

$$\begin{aligned}
\mathcal{P}_C^{(S)} &= -\frac{S(C,D)}{2} = \frac{r}{2} \\
\mathcal{P}_C^{(R)} &= 1 - \mathcal{P}_C^{(S)} = 1 - \frac{r}{2} \\
\mathcal{P}_D^{(R)} &= -\frac{S(D,D)}{2} = \frac{1}{2} + \frac{r}{2} \\
\mathcal{P}_D^{(S)} &= 1 - \mathcal{P}_D^{(R)} = \frac{1}{2} - \frac{r}{2}
\end{aligned} \tag{8 4}$$

The dependence of these probabilities on the r is shown in the graph on the lower left of Fig 8 1 These probabilities fulfil condition (2) However, they also constitute a rational behaviour of the player For example a cooperative player has, in the case of low r, nothing to win from switching Since he might lose its entire payoff when playing – as a D-node – once more against a D-node, rewiring is the preferred reaction For large r however the risk of losing the remaining payoff $1 - r$ is offset by the prospect of benefitting from its C-neighbours after a possible switch Hence, rewiring and switching are equally likely choices In the same manner, a D-node has hardly anything to win from switching in the case of large r It would only gain a profit $1 - r$ when playing against a D-neighbour, but would lose the excess benefit r it currently gets from its C-neighbours Hence, the predominant choice of action for a D-node at large r is rewiring

After a dissatisfied player chooses and carries out one reaction, its trial is over and another agent is chosen at random to be the next trial's player Since we assumed every single node to encounter such a situation with constant frequency ω, the time span δt between two rounds on average results to

$$\langle \delta t \rangle = 1/(\omega N) \tag{8 5}$$

in actual time

8.3.2 A Simple Mean Field Approach

To get a first understanding of how such a system will behave we can resort to a mean-field approach that assumes that every node's environment will represent the composition whole system However, assuming that all nodes feature an identical environment will not allow us to understand the model in full Such an assumption would automatically imply that the number of links between C-nodes and D-nodes is proportional to a well-mixed scenario Our model's rewiring features thus could not be captured Instead, we will assume that all C-nodes have an identical environment and all D-nodes have an identical environment The mean environments of C-nodes and D-nodes are allowed to be different To know how these mean environments looks like, we define three macroscopic variables

1 The *magnetisation* of the system as the difference of the densities of cooperators and defectors,

$$m = \frac{N_C - N_D}{N} \tag{8 6}$$

2 The *link magnetisation* of the system as the difference between the link density between cooperators and between defectors

$$m_l = \frac{L_{CC} - L_{DD}}{L_{\text{tot}}} \tag{8 7}$$

3 The density of links between cooperators and defectors,

$$l_{CD} = \frac{L_{CD}}{L_{\text{tot}}} \tag{8 8}$$

With these variables, we can express the numbers of cooperators and defectors as

$$\begin{aligned} N_C &= N\frac{1+m}{2} \\ N_D &= N\frac{1-m}{2} \end{aligned} \tag{8 9}$$

and calculate the number of different types of links as

$$\begin{aligned} L_{CC} &= \frac{Nk}{2}\frac{1+m_l-l_{CD}}{2} \\ L_{DD} &= \frac{Nk}{2}\frac{1-m_l-l_{CD}}{2} \\ L_{CD} &= \frac{Nk}{2}l_{CD} \end{aligned} \tag{8 10}$$

The average degrees k_C and k_D of C-nodes and D-nodes are thus given by

$$\begin{aligned} k_C &= \frac{2L_{CC}+L_{CD}}{N_C} = k\frac{1+m_l}{1+m} \\ k_D &= \frac{2L_{DD}+L_{CD}}{N_D} = k\frac{1-m_l}{1-m} \end{aligned} \tag{8 11}$$

In the same manner, we can express the mean number of $CC/CD/DD$-links of either a C- or D-node. We express these numbers as averages $\langle\lambda_{XY}\rangle_T$, i.e., the mean number of XY-type links connected to node of type T. The number of links of type XY of a single node is written as λ_{XY}. Since we are currently assuming all nodes of one type to have an identical environment, these values are identical for all nodes. The averages can be expressed in terms of the global variables as

$$\begin{aligned} \langle\lambda_{CC}\rangle_C &= \frac{2L_{CC}}{N_C} = k\frac{1+m_l-l_{CD}}{1+m} \\ \langle\lambda_{CD}\rangle_C &= \frac{L_{CD}}{N_C} = k\frac{l_{CD}}{1+m} \\ \langle\lambda_{CD}\rangle_D &= \frac{L_{CD}}{N_D} = k\frac{l_{CD}}{1-m} \\ \langle\lambda_{DD}\rangle_D &= \frac{2L_{DD}}{N_D} = k\frac{1-m_l-l_{CD}}{1-m} \end{aligned} \tag{8 12}$$

The mean environment of a node is specified through its number of links of each type or, equivalently, through its degree $k_{C/D}$ and its number of CD-links. Therefore, the three global variables are sufficient to fully specify the

mean environment of a single C- or D-node. To understand how the the system evolves over time, we need to derive equations describing how the global variables are expected to change.

We can write the expected change ΔX of a global variable $X \in \{N_{C/D}, L_{CC}, L_{CD}, L_{DD}\}$ during one single trial as

$$\Delta X = \sum_{T=C,D} \mathcal{P}^{(T)} \frac{\lambda_{TD}}{k_T} \sum_{E=R,S} \mathcal{P}_T^{(E)} \Delta X(E, k_T, \lambda_{CD}) \ . \tag{8.13}$$

Here, $\mathcal{P}^{(T)}$ is the probability that a node of type T is chosen as the player, which is simply the density of C- or D-nodes. The probability that such a node chooses a defector as its opponent and hence becomes dissatisfied is given through its share of such neighbours, i.e., λ_{CD}/k_C for cooperators and λ_{DD}/k_D for defectors. The rewiring/switching probabilities $\mathcal{P}_T^{(E)}$ for a node of type T to choose action E are specified in the game model (see Fig. 8.1). Finally, $\Delta X(E, k_T, \lambda_{CD})$ gives the change that such an event E would cause, if it happens at a node of type T with degree k_T and λ_{CD} neighbours of the opposite type. By carrying out the sum in Eq. (8.13), we arrive at a set of coupled equations for the three global variables:

$$\begin{aligned}
\Delta m &= \frac{1}{N}\left[-l_{cd}\frac{1+m}{1+m_\ell}\mathcal{P}_C^{(S)} + \frac{(1-m)(1-m_\ell-l_{cd})}{1-m_\ell}\mathcal{P}_D^{(S)}\right] \\
\Delta m_\ell &= \frac{1}{kN}\left[l_{cd}\left(-k\mathcal{P}_C^{(S)} + \frac{(1+m)^2}{2(1+m_\ell)}\mathcal{P}_C^{(R)}\right)\right. \\
&+ \left.(1-m_\ell-l_{cd})\left(k\mathcal{P}_D^{(S)} + \frac{1-m^2}{2(1-m_\ell)}\mathcal{P}_D^{(R)}\right)\right] \\
\Delta l_{cd} &= \frac{1}{kN}\left[l_{cd}\left(k\frac{1+m_\ell-2l_{cd}}{1+m_\ell}\mathcal{P}_C^{(S)} - \frac{(1+m)^2}{2(1+m_\ell)}\mathcal{P}_C^{(R)}\right)\right. \\
&+ \left.(1-m_\ell-l_{cd})\left(k\frac{1-m_\ell-2l_{cd}}{1-m_\ell}\mathcal{P}_D^{(S)} + \frac{1-m^2}{2(1-m_\ell)}\mathcal{P}_D^{(R)}\right)\right] \ .
\end{aligned} \tag{8.14}$$

These are difference equations for the expected changes occurring during one single trial. By defining a time step analogous to Eq. (8.5), they can be turned into a set of coupled ordinary differential equations. Such non-linear differential equations typically come without an analytic solution. Numerical integrations from predefined initial conditions, however, are straightforward. The numerical results to follow were obtained using a fourth-order Runge-Kutta method.

8.3.3 Simulation Results

Monte Carlo (MC) simulations of the model have been carried out and results are compared with MFT calculations. At first, we look at the long time limits of the simulation for several different initial configurations of the system. We run the MC simulations on a network of $N = 10,000$ nodes for a total time of $\Delta t = 50$ (or 500 000 single trials) to equilibrate the system. Hereafter, we average the system's macroscopic status over one whole time step (or 10 000 single trials). For necessary cases as discussed below, an average was taken over several such systems.

To integrate the MFT equations, initial conditions are required. We define an initial fraction of cooperators f_c^i and assume that the cooperators are randomly distributed on a random network. These two conditions define the initial value of the macroscopic variables as

$$\begin{aligned} m(0) &= 2f_c^i - 1 \\ l_{CD}(0) &= 2f_c^i(1 - f_c^i) \\ m_\ell(0) &= 2f_c^i - 1 \,, \end{aligned} \tag{8.15}$$

from where the MFT equations can be integrated until $t = 50$. The resulting

long time values for the magnetisation are shown in Fig 8 2 and for the *CD*-link density and the link magnetisation in Fig 8 3, respectively

For a better understanding of the results, let us look at Fig 8 3(B) first, which shows the final link magnetisation For small values of r all systems, independent of the initial fraction of cooperators, have a long time limit of $m_\ell(t = \infty) = 1$ This means that all surviving links are indeed between two cooperators Since all systems at any r, show a magnetisation of less than one (see Fig 8 2) some defectors are surviving, but they are isolated and expelled by a network of highly connected cooperators

For larger values of r, the link magnetisation suddenly drops to values below one indicating that the network is now in a different, connected state where some dissatisfied links survive During some intermediate range, both the connected and the disconnected topology are possible final states of the network It should be kept in mind that the disconnected state with its absence of dissatisfied links, does not evolve anymore Such states are commonly referred to as *sticky*, since not even fluctuations can cause the system to enter another stable attractive state In this case, the system is *frozen*, since its configuration does not experience any fluctuations anymore Within the MFT model there exists a transition value $f_c^{i(\mathrm{crit})}(r)$ above which a system will end in a disconnected state In simulation, this threshold is not so precise, since fluctuations can drive a system into a frozen state, from which it of course will not return For a value near $f_c^{i(\mathrm{crit})}(r)$, the fraction of systems ending in a disconnected state monotonously increases over time, since a connected system can always become disconnected through fluctuations, but not vice versa The intermediate values of the link density and magnetisation in Figs 8 3(A) and 8 3 (B) for example for $f_c^i = 0\ 7$ at $r = 0\ 21$, are just an average over an ensemble of connected and disconnected systems that originated from the same

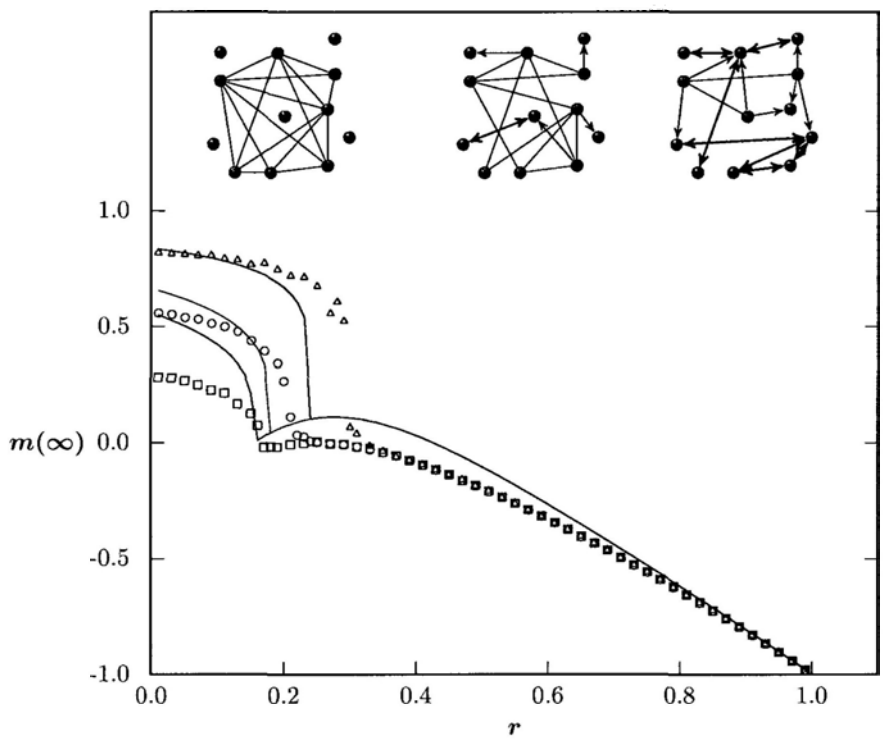

Figure 8.2: Long-time limits of the fraction of cooperation. Simulation results are shown as symbols, starting from random systems with an initial fraction of cooperation of $f_c^i = 0.1$ (red squares), $f_c^i = 0.7$ (blue circles) and $f_c^i = 0.9$ (brown triangles). Lines give the MFT long time limits (color same as for simulations).

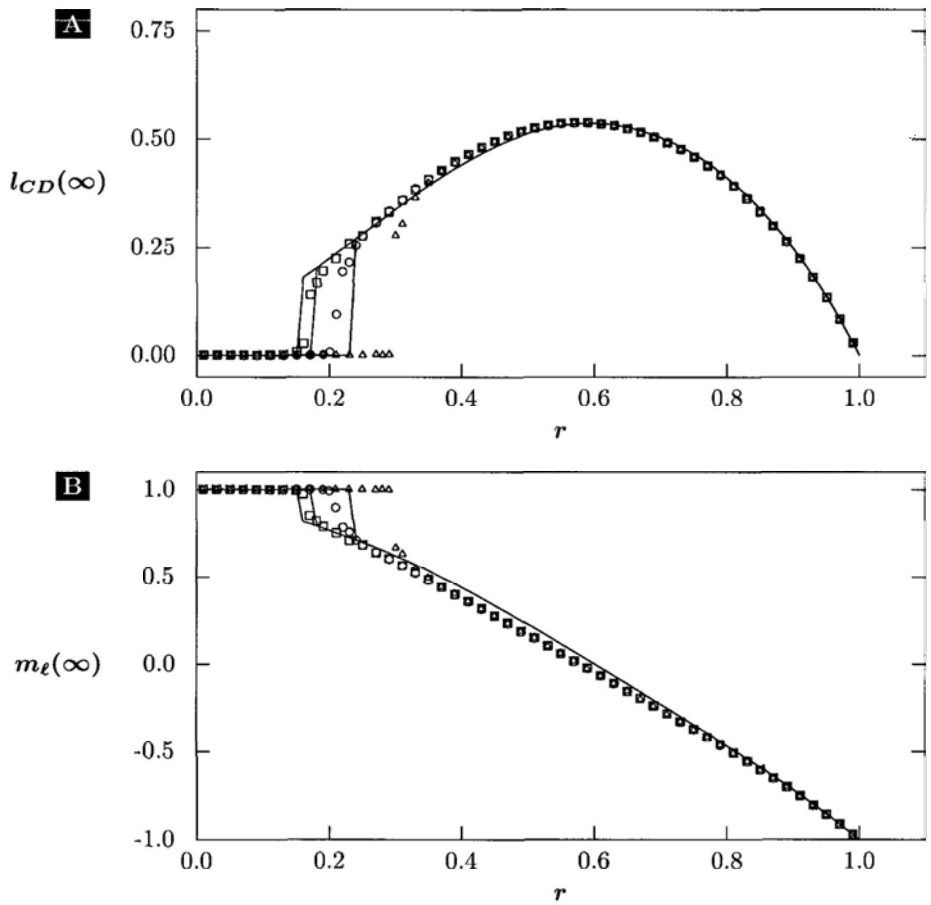

Figure 8.3: Long-time limits of (A) the CD-link density and (B) the link magnetisation. As before, simulation results are shown as symbols, starting from random systems with an initial fraction of cooperation of $f_c^i = 0.1$ (red squares), $f_c^i = 0.7$ (blue circles) and $f_c^i = 0.9$ (brown triangles). Lines give the MFT long time limits (color same as for simulations).

initial conditions The displayed link density values actually do not occur in any single connected system

Figure 8 2 shows the magnetisation and thus the degree of cooperation of the system Small illustrations of network topologies are shown for three different ranges of r The disconnected-connected transition can again be observed at different values of r, depending on the initial fraction of cooperators Cooperation jumps to higher values for systems in the disconnected regime For identical values of r e g , $r = 0\ 2$, systems with initially more cooperators can expel all defectors and form a homogenous network of cooperators, containing nearly 90% of the system's individuals At the same time, systems with initially more defectors enter a connected state, with only about 50% of the individuals being cooperators

Overall, MFT (lines) and simulation (symbols) results are in excellent agreement for the CD-link density and link magnetisation (see Fig 8 3), while agreement is reasonably good for the overall magnetisation (see Fig 8 2) Deviations are mainly observed in two areas The magnetisation in the disconnected state, in particular for low values of f_c^i, and the location of the transition range $r^{(\mathrm{crit})}(f_c^i)$ or vice versa $f_c^{i(\mathrm{crit})}(r)$, in particular for large values of f_c^i To understand the origin of these deviations, it helps to look at the evolution of the system via simulations and MFT

Generally speaking, Eqs (8 14) carry an implicit time dependence since the event probabilities are expressed as rates of the expected change during one time step For the observed deviations, it is more important to understand what the nature of these deviations is than whether the expected evolution just happens slower or faster than expected Therefore, we discuss in the following the evolution of simulated systems and mean-field theory by looking at trajectories Such trajectories are created by projecting the trace of the

vector $(m(t), l_{CD}(t), m_\ell(t))$ onto the m-l_{CD}-plane

Figure 8 4 shows the trajectories of systems with different values of r All systems initially consist nearly exclusively of defectors, i e , the system is close to $m_\ell \approx -1, l_{CD} \approx 0$ A small group of cooperators $f_c = 0\,001$ was added, such that no continuous closure is required for the mean field equations. which have singularities at $m = 1$ and $m = -1$ While trajectories for high-r systems agree very well with MFT's predictions, deviations become obvious for smaller values of r In particular, MFT underestimates the creation of CD-links significantly In addition, the final decay towards $l_{CD} = 0$ occurs pretty much as a straight line in the simulation. which means that Δm is only weakly depending on l_{CD} Theory, on the contrary, predicts a stronger dependence of the switching behaviour on the link density However, the shape of the trajectories is qualitatively captured by MFT for all values of r, lending confidence to the general approach

Figure 8 5 shows trajectories of systems with $r = 0\,2$, but starting from different values for the initial fraction of cooperation Since we assume all systems to have initially random configurations, the starting points in the phase space all lie on the grey parabola 8 15 Again, MFT and simulation agree qualitatively Both simulation and theory show a spiralling decay toward the final value for small values of f_c^i However, a larger amplitude of l_{CD} and a weaker dependence of Δm on l_{CD} are again observed The former actually has interesting consequences for $f_c^i = 0\,1$ and $f_c^i = 0.3$, the lower point of the simulation trajectory is below the value predicted by MFT by a margin of δl_{CD} as indicated in Fig 8 5, but still significantly above $l_{CD} = 0$ For $f_c^i = 0\,7$, however, this lower turning point has fallen so low that the simulation trajectory in fact hits the axis $l_{CD} = 0$ This means the system entered the disconnected, frozen state The same is the case for higher values of $f_c^i = 0\,8$,

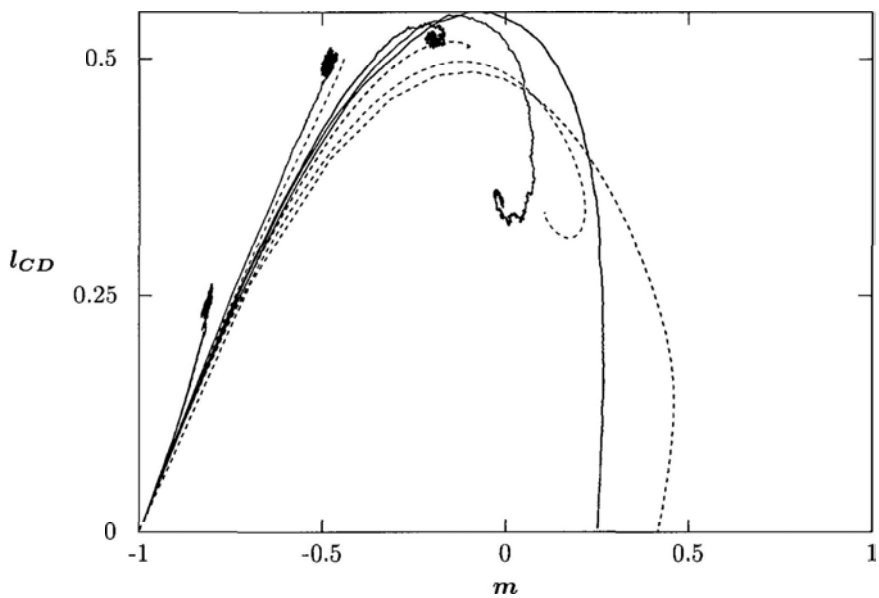

Figure 8.4: Trajectories of ASG systems for different temptation parameters r (dark green: 0.9, orange: 0.7, dark red: 0.5, light blue: 0.3, light red: 0.1), shown for simulations (solid lines) and MFT (dashed lines). All systems start from an initial configuration with $f_c^i = 0.001$ and $k = 4$. Simulated systems have $N = 10000$ nodes in total.

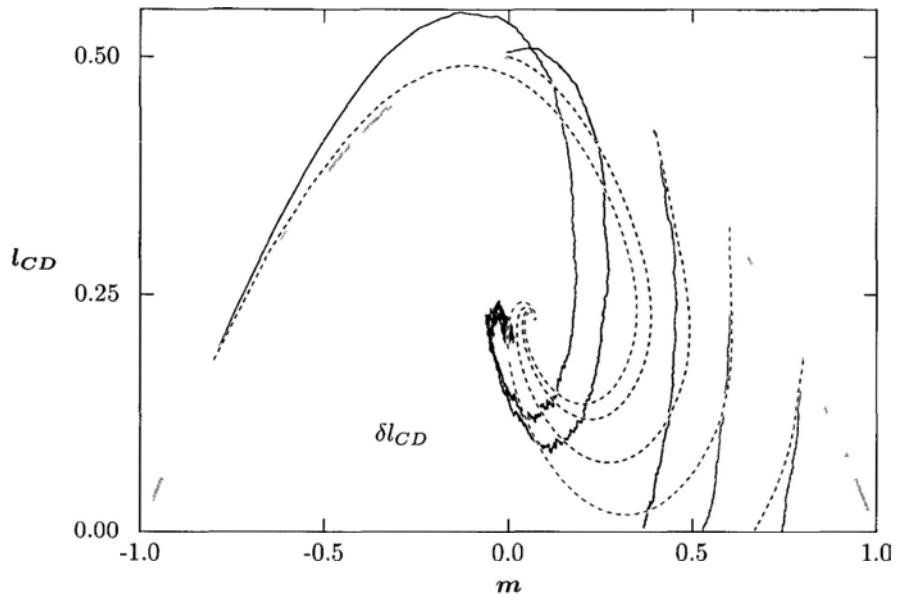

Figure 8.5: Trajectories of ASG systems for temptation parameters $r = 0.2$ and different initial fractions of cooperators f_c^i (light blue: 0.1, dark red: 0.5, dark green: 0.7, orange: 0.8, purple: 0.9), shown for simulations (solid lines) and MFT (dashed lines). The gray parabola gives the subspace of randomly distributed cooperators. System parameters: $k = 4$, (simulation: $N = 10,000$).

and hence can be identified as the source of the discrepancy between theory and simulation in critical initial fraction of cooperation as observed in Fig. 8.2.

8.4 Summary

In this chapter, we have proposed and discussed the Dissatisfied-Adaptive Snowdrift Game and reviewed the evolutionary Snowdrift Game and social dilemmas in general. We have introduced the model and discussed the validity of its rules. Alongside, a mean-field theory was derived and compared with

computer simulations of the game model The mean-field model makes very restrictive assumptions, such as that all nodes of one kind are expected to behave identically Still, it captures all key features of our model but quantitative deviations are observed These deviations have to be addressed before we try to use the MFT to get a deeper understanding of our proposed model

Chapter 9

Adaptive Snowdrift Game Networks: Formulating Mean Field Theories

9.1 Remaining Issues and Change of Variables

As shown in Sec. 8.3, a strict mean-field approach is able to explain key features of the dissatisfied-adaptive Snowdrift Game. The quantitative deviations between MFT and simulation results indicate that some relevant parts of the behaviour of the model are not yet captured. In what follows, we seek to improve the mean-field model. To do so, we will re-derive the mean-field equations, with an explicit focus on when and in what manner any potentially erroneous assumptions are made.

As a first step, we will transform our set of global variables into a new one which will allow to include fluctuations in a more concise way. We define the

new densities and variables as

$$f_c = N_C/N = \frac{1+m}{2} \tag{9 1}$$

$$l_{CD}^{(\mathrm{new})} = L_{CD}/N = l_{CD}^{(\mathrm{old})}\frac{k}{2} \tag{9 2}$$

$$l_{CC} = \frac{L_{CC}}{N} = \frac{1+m_l-l_{CD}}{2}\frac{k}{2} \tag{9 3}$$

The new CD-link density $l_{CD}^{(\mathrm{new})}$ differs from the old one only in that it is normalised by the number of nodes rather than by the total number of links For the sake of simplicity, we will in the following use the symbol $l_{CD} \equiv l_{CD}^{(\mathrm{new})}$ exclusively with the new definition of the CD-link density The mapping between the old and new set of variables is an isomorphism, i e , at any time there exists an unique relation between exactly two points in the old variables' and new variables' phase spaces

To formulate the mean field equations, we start again from a point akin to Eq (8 13) Since we will not include any implicit assumptions here, we do allow nodes to have varying degree and environment

$$\Delta X = \sum_{T=C\,D} \mathcal{P}^{(T)} \sum_{\kappa=0} \mathcal{P}_T^{(\kappa)} \sum_{\lambda_{CD}=0}^{\kappa} \mathcal{P}_{T\,\kappa_T}^{(\lambda_{CD})} \frac{\lambda_{TD}}{\kappa_T} \sum_{E=R\,S} \mathcal{P}_T^{(E)} \Delta X(E,\kappa_T,\lambda_{CD}) \tag{9 4}$$

As before, $\mathcal{P}^{(T)}$ is the fraction of nodes of type T In addition, we now sum over all possible configurations a single node can have i e , every possible degree $0 \leq \kappa \leq N-1$ and every possible number of $CD-$links $0 \leq \lambda_{CD} \leq \kappa$ To do so, we include the two conditional probabilities into the summation The probability $\mathcal{P}_T^{(\kappa)}$ of a node of type T to have degree κ, and the probability $\mathcal{P}_{T\,\kappa_T}^{(\lambda_{CD})}$ for a node of type T with degree κ_T to have λ_{CD} CD-links As before, the fraction $\lambda_{\mathrm{TD}}/\kappa_{\mathrm{T}}$ is the likelihood of picking a dissatisfied link for the trial The changes in the macroscopic quantities ΔX are defined as before

Neither of the conditional probabilities $\mathcal{P}_T^{(\kappa)}$ and $\mathcal{P}_{\kappa T}^{(\lambda_{CD})}$ is known However, we do not actually need the exact probability distribution functions to derive a better mean-field theory Since we sum over all possible combinations, the sums will only return the equally unknown expectation values Expressing the mean field equations in terms of these expectation values, we get

$$\Delta N_C = (1-f_c)\left(1-\left\langle\frac{\lambda_{CD}}{\kappa}\right\rangle_D\right)\mathcal{P}_D^{(S)} - f_c\left\langle\frac{\lambda_{CD}}{\kappa}\right\rangle_C\mathcal{P}_C^{(S)} \quad (9\,5)$$

$$\begin{aligned}\Delta L_{CD} &= f_c\mathcal{P}_C^{(S)}\left(\langle\lambda_{CD}\rangle_C - 2\left\langle\frac{\lambda_{CD}^2}{\kappa}\right\rangle_C\right) - f_c^2\mathcal{P}_C^{(R)}\left\langle\frac{\lambda_{CD}}{\kappa}\right\rangle_C \\ &+ (1-f_c)\mathcal{P}_D^{(S)}\left(\langle\kappa\rangle_D - 3\langle\lambda_{CD}\rangle_D + 2\left\langle\frac{\lambda_{CD}^2}{\kappa}\right\rangle_D\right) \\ &+ f_c(1-f_c)\mathcal{P}_D^{(R)}\left(1-\left\langle\frac{\lambda_{CD}}{\kappa}\right\rangle_D\right) \quad (9\,6)\end{aligned}$$

$$\begin{aligned}\Delta L_{CC} &= f_c\mathcal{P}_C^{(S)}\left(\left\langle\frac{\lambda_{CD}^2}{\kappa}\right\rangle_C - \langle\lambda_{CD}\rangle_C\right) + f_c^2\mathcal{P}_C^{(R)}\left\langle\frac{\lambda_{CD}}{\kappa}\right\rangle_C \\ &+ (1-f_c)\mathcal{P}_D^{(S)}\left(\langle\lambda_{CD}\rangle_D - \left\langle\frac{\lambda_{CD}^2}{\kappa}\right\rangle_D\right) \quad (9\,7)\end{aligned}$$

$$\begin{aligned}\Delta L_{DD} &= f_c\mathcal{P}_C^{(S)}\left\langle\frac{\lambda_{CD}^2}{\kappa}\right\rangle_C \quad (9\,8) \\ &- (1-f_c)\mathcal{P}_D^{(S)}\left(\langle\kappa\rangle_D - 2\langle\lambda_{CD}\rangle_D + \left\langle\frac{\lambda_{CD}^2}{\kappa}\right\rangle_D\right) \\ &- f_c(1-f_c)\mathcal{P}_D^{(R)}\left(1-\left\langle\frac{\lambda_{CD}}{\kappa}\right\rangle_D\right)\end{aligned}$$

A detailed derivation of these equations can be found in Appendix A By examining these equations, we see that there are three kinds of expectation values included in the equations

1 The mean number of links per node, e g , $\langle\kappa\rangle$ or $\langle\lambda_{XY}\rangle$ These averages all refer to the number of links a node on average has, and are also referred to as the first moments

2 The mean fraction of CD-links $\langle \lambda_{CD}/\kappa \rangle$

3 The mean squared number of CD-links over the node degree $\langle \lambda_{CD}^2/\kappa \rangle$

We need to find a way to express these expectation values in terms of our global variables accurately to arrive at a closed set of mean field equations

The first moments, i e , the mean values of the number of links attached to a certain type of node can be expressed directly in terms of the global variables

$$\langle \lambda_{CD} \rangle_C = \frac{l_{CD}}{f_c} \tag{9 9}$$

$$\langle \lambda_{CD} \rangle_D = \frac{l_{CD}}{1 - f_c} \tag{9 10}$$

$$\langle \kappa \rangle_C = \frac{2l_{CC} + l_{CD}}{fc} \tag{9 11}$$

$$\langle \kappa \rangle_D = \frac{k - 2l_{CC} - l_{CD}}{1 - fc} \tag{9 12}$$

To close the system, further assumptions have to be made regarding the combined moments, so that we can express the expectation values of the fractions and the second moments in terms of the global variables It is commonly assumed that the degree distribution of agents if sufficiently narrow, can be taken to be a δ-function [120] This means that every node of each type has the same degree As a consequence, the denominator of the fractions is a constant that can be pulled outside the average For our case, we make the slightly less restrictive assumption that the average over the fraction can be decoupled into a fraction of two averages

$$\begin{aligned} \left\langle \frac{l_{CD}}{\kappa} \right\rangle_{C/D} &= \frac{\langle l_{CD} \rangle_{C/D}}{\langle \kappa \rangle_{C/D}} \\ \left\langle \frac{l_{CD}^2}{\kappa} \right\rangle_{C/D} &= \frac{\langle l_{CD}^2 \rangle_{C/D}}{\langle \kappa \rangle_{C/D}} \end{aligned} \tag{9 13}$$

Both the average of the degree as well as the average of the number of CD-links can be expressed in terms of the global variables, and hence only the second moment of $CD-$links $\langle \lambda_{CD}^2 \rangle$, connected to either type of node, remains undefined. The second moment is related to the variance of a distribution as

$$\sigma^2 = \langle X^2 \rangle - \langle X \rangle^2 \Rightarrow \langle X^2 \rangle = \langle X \rangle^2 + \sigma^2 \ , \tag{9.14}$$

which means we have to make an assumption regarding the variance of the $CD-$link distribution.

Although finding the variance of a random variable requires significantly less information than the specification of its probability distribution, deducing just the variance from our set of rules would constitute a formidable problem. However, our previous attempt at a mean-field theory was already rather successful (see Sec. 8.3.3), even though we assumed that all nodes were identical. This means that we assumed zero variance, and replaced the second moment just with a squared first moment, which we are able to express in global variables:

$$\begin{aligned} \langle l_{CD}^2 \rangle_{\mathrm{C}}^{(\mathrm{SSC})} &\equiv \langle l_{CD} \rangle_C^2 = \frac{l_{CD}^2}{f_c^2} \\ \langle l_{CD}^2 \rangle_{\mathrm{D}}^{(\mathrm{SSC})} &\equiv \langle l_{CD} \rangle_D^2 = \frac{l_{CD}^2}{(1-f_c)^2} \ . \end{aligned} \tag{9.15}$$

We refer to this as the *simple squared closure* (SSC), since it just squares the first moments. The variance is positive definite, and this closure thus constitutes a lower boundary for the second moment. We know, however, that this assumption is wrong: even if no features intrinsic to the model spread out the distribution, the rewiring mechanism picks a random node as the new neighbour, which will inevitably lead to some variation in the node degree.

We hence have to find a different closure that incorporates fluctuations One possible option is to adapt the mean-field closure of Gross *et al* [7] for the adaptive SIS network A detailed derivation and discussion of this closure can be found in Appendix B (see in particular Eqs (B 15)-(B 17)) This method was originally proposed by Keeling and Eames and we will hereafter refer to it as the Keeling/Eames (KE) closure [82] The resulting relation between the overall second moment and the number of link is

$$\langle \lambda_{SI}^2 \rangle = \frac{L_{ISI}}{N_S} + \frac{L_{SI}}{N_S} = \frac{L_{SI}^2}{N_S^2} + \frac{L_{SI}}{N_S} \tag{9 16}$$

This means that in the KE closure, the mean and the variance of the distribution of SI-links per $S-$node are identical We can simply transfer this assumption by defining

$$\begin{aligned} \langle \lambda_{CD}^2 \rangle_C^{(\mathrm{KE})} &= \frac{l_{CD}^2}{f_c^2} + \frac{l_{CD}}{f_c} \\ \langle \lambda_{CD}^2 \rangle_D^{(\mathrm{KE})} &= \frac{l_{CD}^2}{(1-f_c)^2} + \frac{l_{CD}}{(1-f_c)} \end{aligned}$$

A third option is to use a closure based on the binomial distribution The binomial distribution describes the number of successful outcomes of a random experiment with success probability p that is repeated n times The mean number of successful events is $\mu = np$, and the variance is $\sigma^2 = np - np^2$ If we look at a single node, we can consider its degree to be the number of repetitions $n = \kappa$ Also, if we assume that the links are just randomly distributed, we can define the success probability as the number of CD-links over the number of total links connected to a node

$$\begin{aligned} \mathcal{P}_{\mathrm{C}} &= \frac{l_{CD}}{l_{CD} + 2l_{CC}} \\ \mathcal{P}_{\mathrm{D}} &= \frac{l_{CD}}{l_{CD} + 2l_{DD}} = \frac{l_{CD}}{k - 2l_{CC} - l_{CD}} \end{aligned} \tag{9 17}$$

The binomial distribution is only defined for an integer number of repetitions n. However, we can just apply the definitions of the mean and the standard deviation of the binomial distribution to the mean values of the degree and arrive at

$$\begin{aligned}
\langle \lambda_{CD}^2 \rangle_C^{(BINO)} &\equiv \kappa_C^2 \mathcal{P}_C^2 + \kappa_C \mathcal{P}_C - \kappa_C \mathcal{P}_C^2 \\
&= \frac{l_{CD}^2}{f_c^2} + \frac{l_{CD}}{f_c} - \frac{l_{CD}^2}{f_c(2l_{CC} + l_{CD})} \\
\langle \lambda_{CD}^2 \rangle_D^{(BINO)} &\equiv \kappa_D^2 \mathcal{P}_D^2 + \kappa_D \mathcal{P}_D - \kappa_D \mathcal{P}_D^2 \\
&= \frac{l_{CD}^2}{(1-f_c)^2} + \frac{l_{CD}}{1-f_c} - \frac{l_{CD}^2}{(1-f_c)(k - 2l_{CC} - l_{CD})} \,.
\end{aligned} \tag{9.18}$$

It should be noted that neither of these closures takes the exact rules of the model in any way into account. In fact, the binomial closure basically assumes the fluctuations to be purely random and not assortative at all. This is most likely not the case. However, given that our previous models in fact denied the very existence of fluctuations, these new closures should improve upon our previous results. In what follows, we will analyse the validity of each of our assumptions against simulations, and discuss which closure is best suited for a mean-field theory of the DASG model.

9.2 Assumption Validation

To close our set of mean field equation, we need to make two assumptions: the decoupling approximation Eq. (9.13), and an second-moment approximation. For the latter, we can choose among the simple squared closure Eq. (9.15), the Keeling/Eames closure Eq. (9.17), or the binomial closure Eq. (9.18). Before we will test if and to what degree these assumptions can improve our MFT results of Ch. 8, we will first test the validity of each of these assumptions directly against the simulation.

9.2.1 Decoupling Approximation

The decoupling approximation consists actually of two approximations, since we require both the first and the second moment of $CD-$links to decouple from the $1/\kappa$ factor, i.e.,

$$\begin{aligned} \left\langle \frac{l_{CD}}{\kappa} \right\rangle_{C/D} &= \frac{\langle l_{CD} \rangle_{C/D}}{\langle \kappa \rangle_{C/D}} \\ \left\langle \frac{l_{CD}^2}{\kappa} \right\rangle_{C/D} &= \frac{\langle l_{CD}^2 \rangle_{C/D}}{\langle \kappa \rangle_{C/D}} \,. \end{aligned}$$

Each of the approximations has to be valid for both C- and D-nodes. An additional problem is that the original average $\langle \lambda_{CD}^{1|2}/\kappa \rangle$ is an average over a fraction. As our original results showed us, it is possible for a node to become isolated and have zero degree, in which case the fraction $0/0$ is undefined. To resolve this, we have to slightly alter the definition of the average. If a player without any neighbours is chosen for trial, he will not find an opponent and hence no change will occur. Consequently, we will count all nodes without neighbours by defining $\kappa = 0 \rightarrow \lambda_{CD}/\kappa \equiv \lambda_{CD}^2/\kappa \equiv 0$.

Figure 9.1(A) shows the time evolution of the mean second moment per degree. The values show a qualitatively very similar behavior, but the decoupling approximation slightly exceeds the real simulation average. This is further exemplified in Fig. 9.1(C), which shows the same data by plotting the simulation averages on the x-axis against the approximation results on the y-axis. If the decoupling approximation was 100% accurate, the curves of both types of nodes would collapse onto the dotted $y = x$ line. However, this is the case only for $D-$nodes (blue line), and for C-nodes during the early stages of the simulation(red line). In the long time limit, the trajectory of the C-node approximation is slightly above the equivalency line, showing that our assumption is not fully valid here.

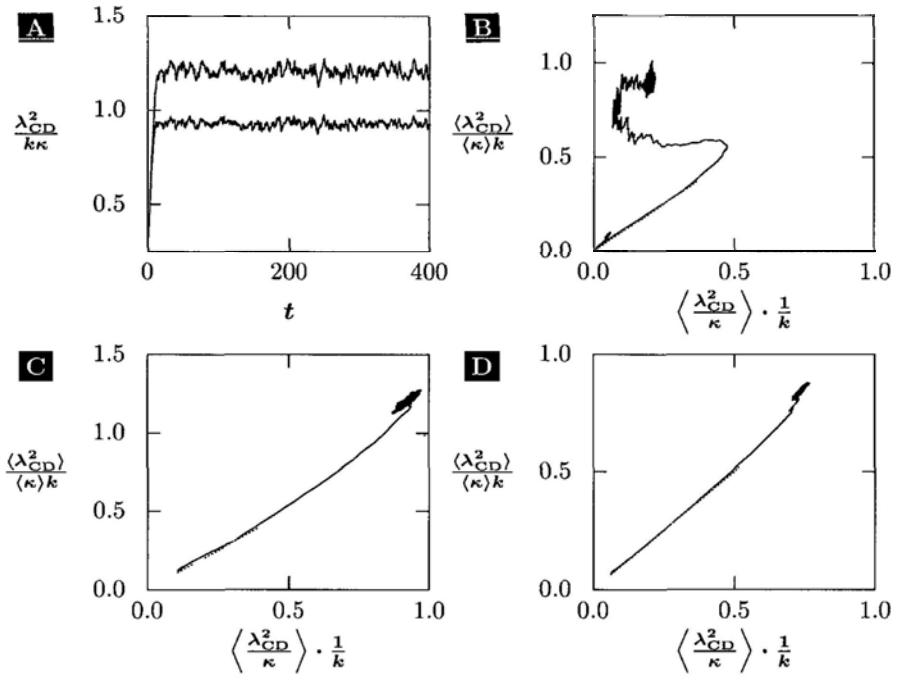

Figure 9.1: Test of the decoupling approximation for the second moment. (A) $\langle\lambda^2_{CD}/\kappa\rangle$ as measured in the simulation (red) and as given by the decoupling $\langle\lambda^2_{CD}\rangle/\langle\kappa\rangle$ (blue), shown for $C-$nodes over time. Parameters: $k = 4$, $r = 0.8$, started from a random graph with $f^t_c = 0.5$. (B)-(D): Plot of the decoupled average $\langle\lambda_{CD}\rangle/\langle\kappa\rangle$ versus the actual average $\langle\lambda_{CD}/\kappa\rangle$, with the dotted diagonal indicating perfect agreement between simulation and assumption. Parameters: (B) $k = 4$, $r = 0.2$; (C) $k = 4$, $r = 0.8$; (D) $k = 10$, $r = 0.8$. All panels are normalised by the system's respective mean degree k. Results for C-nodes(D-nodes) are shown in red (blue). All simulations use networks with $N = 10,000$ nodes.

Figure 9.1(D) shows an identical setup, but for a network with a mean degree of $k = 10$. While the data qualitatively resembles that in Fig. 9.1(C), the deviations are less pronounced here. The reason for this is related to the problem of zero-degree nodes, since it is less likely to occur in a network with higher connectivity. The opposite issue is illustrated in Fig. 9.1(B), where the same relationship is shown for a system with $k = 4$ and $r = 0.2$. In this regime, D-nodes have very few neighbours and are comparably often isolated. Accordingly, the decoupling assumption fully breaks down here. The decoupled mean $\langle\lambda_{CD}^2\rangle_{\mathrm{D}}/\langle\kappa\rangle_{\mathrm{D}}$ is not only not identical but also not even correlated to the simulation mean $\langle\lambda_{CD}^2/\kappa\rangle_{\mathrm{D}}$. However, this does not necessarily make our assumption less useful. In this regime, few D-nodes exist, and even fewer will have dissatisfied links connecting them to other D-nodes. Hence, the overall impact of this very large deviation will be limited.

Figure 9.2 illustrates the approximation for the first moment in the same manner. Fig. 9.2(A) again shows the time evolution, with the evolution of the approximation here being virtually identical to that of the real average. Accordingly, the trajectories both collapse onto the diagonal in Figs. 9.2(C) and (D). This means that the decoupling approximation is much more accurate when applied to the first moment. The problematic case of a system with many isolated nodes is again shown in Fig. 9.2(B). Indeed, the decoupling approximation breaks down again for this case, and is not valid for the first moments of D-nodes for small r either. However, the relevance of D-nodes to the system's evolution in this case is again limited, and we will have to investigate further to see whether or not this large deviation has any impact on the mean-field theory's results.

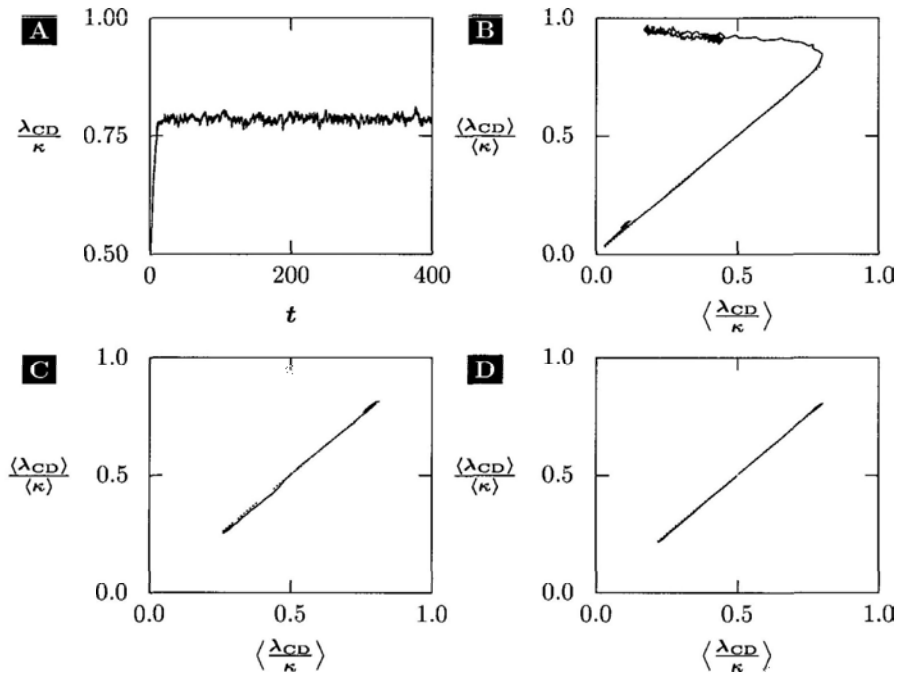

Figure 9.2: Test of the decoupling approximation for the first moment. (A): $\langle\lambda_{CD}/\kappa\rangle$ as measured in the simulation (red) and as given by the decoupling $\langle\lambda_{CD}\rangle/\langle\kappa\rangle$ (blue), shown for $C-$nodes over time. Parameters: $k = 4$, $r = 0.8$, started from a random graph with $f_c^t = 0.5$. (B)-(D): Plot of the decoupled average $\langle\lambda_{CD}\rangle/\langle\kappa\rangle$ versus the actual average $\langle\lambda_{CD}/\kappa\rangle$, with the dotted diagonal indicating perfect agreement between simulation and assumption. Parameters: (B) $k = 4$, $r = 0.2$; (C) $k = 4$, $r = 0.8$; (D) $k = 10$, $r = 0.8$. Results for C-nodes(D-nodes) are shown in red (blue). All simulations use networks with $N = 10000$ nodes.

9.2.2 Closure Approximation

The merit of the different moment closures are more difficult to evaluate. Generally, the second moment can vary substantially during a simulation run, and there is no a-priori estimate regarding which part of the dynamics is most relevant to the overall evolution. Therefore, we will for now only discuss the qualitative behaviour of the different closures, before moving on to a more rigorous overall comparison in Sec. 9.2.3.

Figure 9.3 shows the initial evolution of the second moment in several simulated systems, together with the second moment, calculated using different closure methods. As it was expected from the definition of the moment closures, we generally find $\langle\lambda^2_{CD}\rangle^{(KE)}_C > \langle\lambda^2_{CD}\rangle^{(BINO)}_C > \langle\lambda^2_{CD}\rangle^{(SSC)}_C$ for any configuration. Furthermore, we find $\langle\lambda^2_{CD}\rangle^{(SIM)}_C > \langle\lambda^2_{CD}\rangle^{(KE)}_C$, i.e., all closures still underestimate the variance of the CD-link distribution. Quantitatively, the results differ in inconsistent ways, e.g., for distributions with a higher degree $k = 10$ and low $r = 0.2$, as shown in Fig. 9.3(B), the binomial distribution and the Keeling/Eames closure are nearly identical. On the contrary, for systems with small $k = 4$ and high $r = 0.8$, the binomial distribution is very close to the simple squared closure, as shown in Fig. 9.3(D).

Figure 9.4 shows the same data for the second moments connected to D-nodes$\langle\lambda^2_{CD}\rangle_{\mathrm{D}}$. The observed features are generally very similar to those observed at C-nodes. We again find $\langle\lambda^2_{CD}\rangle^{(KE)}_D > \langle\lambda^2_{CD}\rangle^{(BINO)}_D > \langle\lambda^2_{CD}\rangle^{(SSC)}_D$. Also, the binomial closure will, depending on the simulated system, be sometimes close to either the simple squared closure (Fig. 9.4(B)) or the Keeling/Eames closure (Fig. 9.4(D)). However, there are some important differences. For all panels, we can see that within a very small range, the KE closure exceeds the observed second moment. Such an error is positively correlated with the error

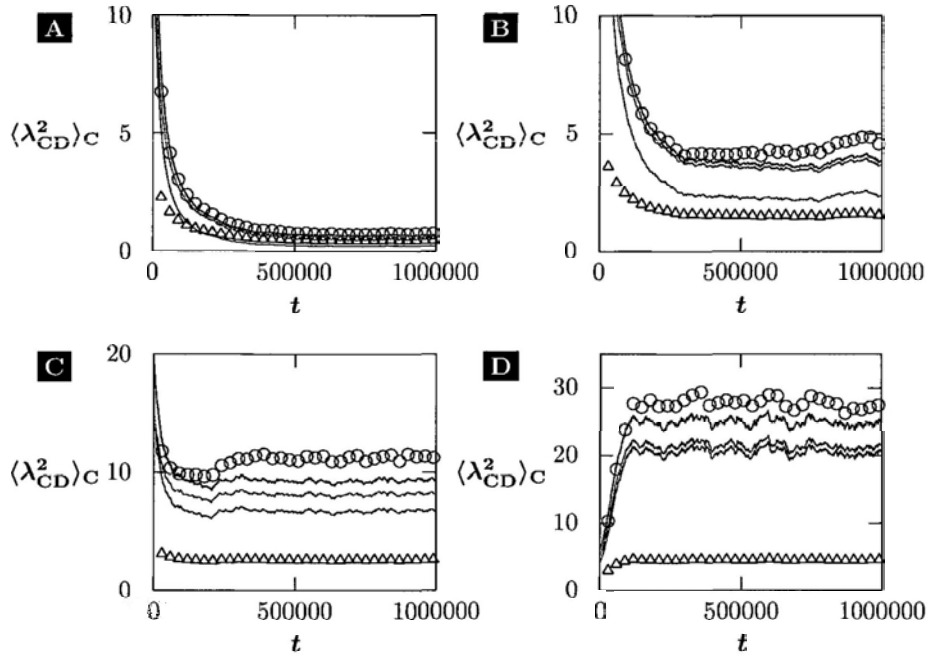

Figure 9.3: Second moment of CD-links connected to C-nodes $\langle\lambda^2_{CD}\rangle_C$ as taken from simulations (blue circles), compared with different moment closure approximations: simple squared closure (purple lines), binomial closure (orange lines), Keeling/Eames closure (dark blue lines). The underlying first moment of CD-links $\langle\lambda_{CD}\rangle_C$ is shown for comparison using green triangular symbols. Parameters used for each panel: (A) $r = 0.2$, $f_c^i = 0.01$, $k = 4$; (B) $r = 0.2$, $f_c^i = 0.5$, $k = 10$; (C) $r = 0.5$, $f_c^i = 0.01$, $k = 4$; (D) $r = 0.8$, $f_c^i = 0.5$, $k = 4$.

observed for the decoupling approximation of the second moment. We will therefore need to investigate the combined error of decoupling and moment closure approximation.

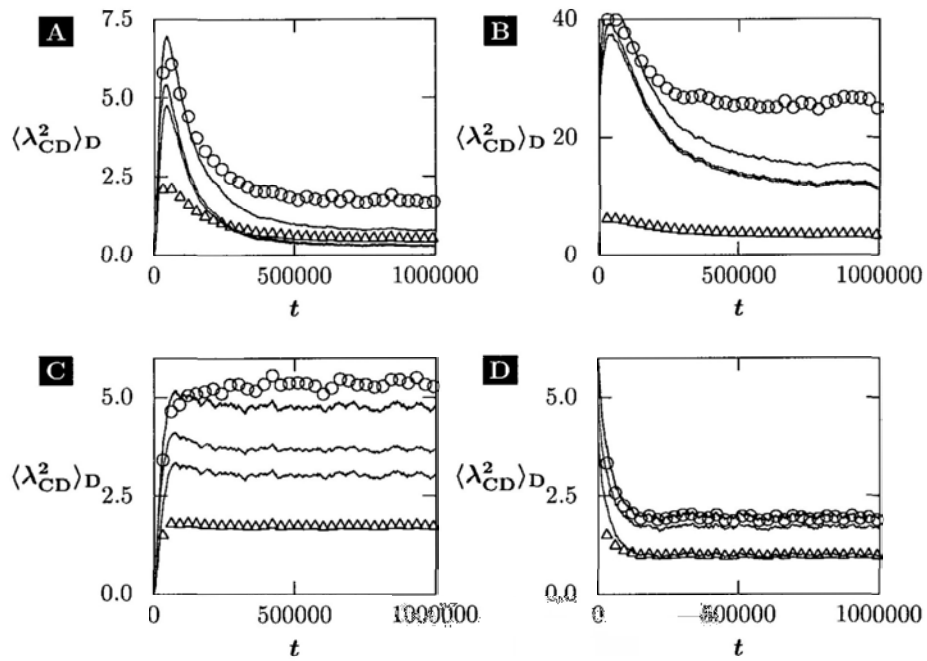

Figure 9.4: Second moment of CD-links connected to D-nodes $\langle\lambda^2_{CD}\rangle_D$ as taken from simulations (blue circles), compared with different moment closure approximations: simple squared closure (purple lines), binomial closure (orange lines), Keeling/Eames closure (dark blue lines). The underlying first moment of CD-links $\langle\lambda_{CD}\rangle_C$ is shown for comparison using green triangular symbols. Parameters used for each panel: (A) $r = 0.2$, $f_c^i = 0.01$, $k = 4$; (B) $r = 0.2$, $f_c^i = 0.5$, $k = 10$; (C) $r = 0.5$ $f_c^i = 0.01$, $k = 4$; (D) $r = 0.8$, $f_c^i = 0.5$, $k = 4$.

9.2.3 Overall Assumption Accuracy

In the last two sections, we discussed the validities of the two assumptions we need to make in order to close the mean-field equations. During the discussion, we found that the decoupling approximation for the second moment in general, the decoupling approximation in case of isolated nodes, and the closure of the second moment are problematic areas. However, it is hard to judge the impact of these problems on the mean-field theory. To proceed, it is useful to consider the quantity

$$\Lambda = \left\langle \frac{\lambda_{CD}^2}{\kappa} \right\rangle - \langle \lambda_{CD} \rangle \ . \tag{9.19}$$

We can calculate this quantity directly from simulation data, or we can instead calculate the macroscopic variables of a simulation state, and calculate Λ from these variables using our decoupling and moment closure approximation. The interesting point about this quantity is that we can make some a-priori assumptions about it. For example, we expect it to be negative definite, because

$$\begin{aligned} \left\langle \frac{\lambda_{CD}}{\kappa} \lambda_{CD} \right\rangle \quad &\leq \quad \left\langle \underbrace{\frac{\lambda_{CD}}{\kappa}}_{<1} \right\rangle \langle \lambda_{CD} \rangle \leq \langle \lambda_{CD} \rangle \\ &\Rightarrow \Lambda \leq 0 \ . \end{aligned} \tag{9.20}$$

In addition, we can expect

$$\begin{aligned} \lim_{\lambda_{CD}/\kappa \to 0} \Lambda &= 0 \\ \lim_{\lambda_{CD}/\kappa \to 1} \Lambda &= 0 \ . \end{aligned} \tag{9.21}$$

This means that for nodes that have zero $CD-$links, both terms in the definition of Λ vanish. On the other hand, the two terms become equal to κ and cancel each other if a node only has neighbours of the other type. These

conclusions are important in that they describe situations that indeed occur in our network near the disconnected-connected transition. For low r, D-nodes become isolated, however, they cut links among themselves first so that the surviving links are nearly exclusively of CD-type. In contrast, C-nodes associate with each other and seek to expel D-nodes, resulting in a configuration with nearly no CD-links at all.

It also should be noted that Λ occurs in the mean-field equations. For example, in Eq. (9.7) for the number of CC-links, Λ represents the expected change for a $C \to D$-switch, and $-\Lambda$ the expected change for a $D \to C$-switch. Also,

$$\lim_{\lambda_{CD}/\kappa \to 1} \langle \kappa \rangle - 3\langle \lambda_{CD} \rangle + 2 \left\langle \frac{\lambda_{CD}^2}{\kappa} \right\rangle = 2\Lambda \ ,$$

which is a term that represents the expected change of CD-links for a $D \to C$-switch. Therefore, errors in Λ, particularly if they violate the conditions in Eqs. (9.20) and (9.21), can have a direct impact on the accuracy of the equations of motion.

Figure 9.5 shows Λ, calculated for both C- and D-nodes. The data has been taken directly from simulation, and calculated from the macroscopic variables using the decoupling and different closure approximations. It is plotted versus the mean success probability to pick a neighbour of opposite kind $\mathcal{P}^{(\mathrm{opp})} = \lambda_{CD}/\kappa$. For plotting the real simulation averages, $\mathcal{P}^{(\mathrm{opp})}$ was calculated as a simulation mean as well $\mathcal{P}^{(\mathrm{opp})} = \langle \lambda_{CD}/\kappa \rangle$. This average cannot be calculated from the macroscopic variables, and it was therefore calculated as $\mathcal{P}^{(\mathrm{opp})} = \langle \lambda_{CD} \rangle / \langle \kappa \rangle$ for all of the approximative curves.

All panels in Fig. 9.5 show that the simulation average and the previously used simple squared closure fulfil both requirements, they are negative definite and vanish on the intervals boundaries. However, the simple squared closure

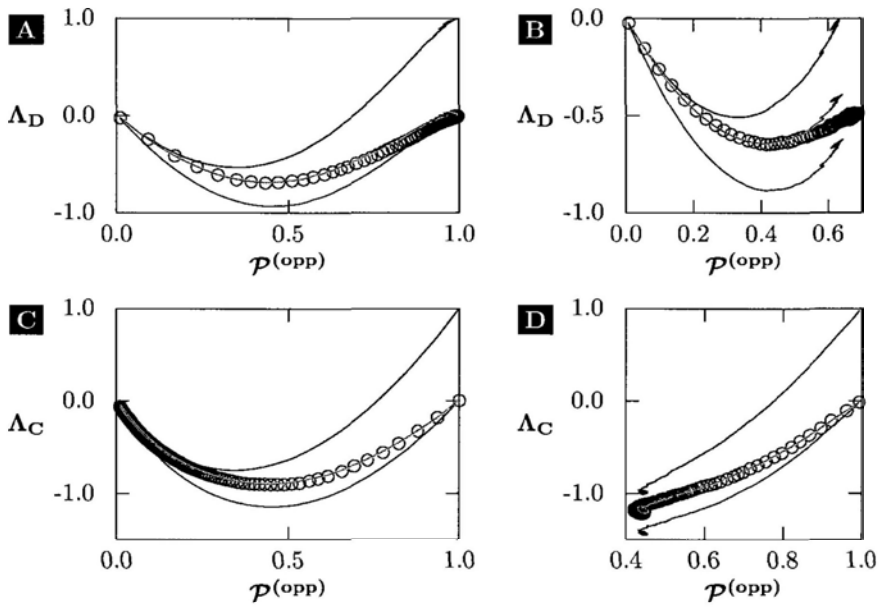

Figure 9.5: Control quantity Λ, plotted against the probability $\mathcal{P}^{(\text{opp})}$ for different systems. All panels show Λ taken directly from simulations (circles) compared with the results of the KE closure (dark blue line), simple squared closure (purple line) and binomial closure (orange line). The probability to pick a $CD-$link was calculated directly in the ensemble as $\mathcal{P}^{(\text{opp})} = \langle \lambda_{CD}/\kappa \rangle$ for the simulation average, or through the decoupling approximation as $\mathcal{P}^{(\text{opp})} = \langle \lambda_{CD} \rangle / \langle \kappa \rangle$ for all approximative closures. System parameters: (A) D-nodes, $r = 0.1$; (B) D-nodes, $r = 0.5$; (C) C-nodes, $r = 0.1$; (D) C-nodes, $r = 0.5$. All systems: $k = 4$, $f_c^i = 0.01$, $N = 10000$.

significantly underestimates the variance of the CD-link distribution. There are thus equally significant deviations in the resulting Λ. Meanwhile, the binomial distribution also fulfils the requirements Eqs. (9.20) and (9.21), but shows a much better agreement with the simulation average. Deviations are only visible in Fig. 9.5(B). The observed differences are actually mostly caused by a deviation in the probability to pick a CD-link $\mathcal{P}^{(\mathrm{opp})}$. For D-nodes in the low r-regime, this kind of deviation was already demonstrated in Fig. 9.2(B).

The KE closure meanwhile shows very strong deviations for D-nodes, and in the small r-regime does not even fulfil the negativity requirement anymore. As we mentioned before, Λ represents the change in the macroscopic quantities for certain events. The here observed deviation in the KE closure means that, for a network with no DD-links at all, a switching D-node is expected to turn nonexistent DD- into CD-links. Indeed, if one tries to apply the KE-closure to the mean-field equations, the resulting trajectories will often be unphysical, e.g., featuring negative or infinite link densities. Using the binomial closure, we can repeat previous calculations and check whether the accuracy of the mean-field calculations has been improved. Figure 9.6 shows the long-time limits of the fraction of cooperation for the same set of simulations as Fig. 8.2. We use the new variable f_c^{∞} instead of the system magnetisation m, however, this just means that the vertical axis has been linearly rescaled. The previous results, which were in effect obtained using a SSC closure, are indicated by black dashed lines. The improvement over the SSC closure is clearly visible. In particular, simulation and MFT are now in perfect agreement for the disconnected state in the low r-regime, which previously showed the most significant deviations. In contrast, deviations are still visible for the connected state.

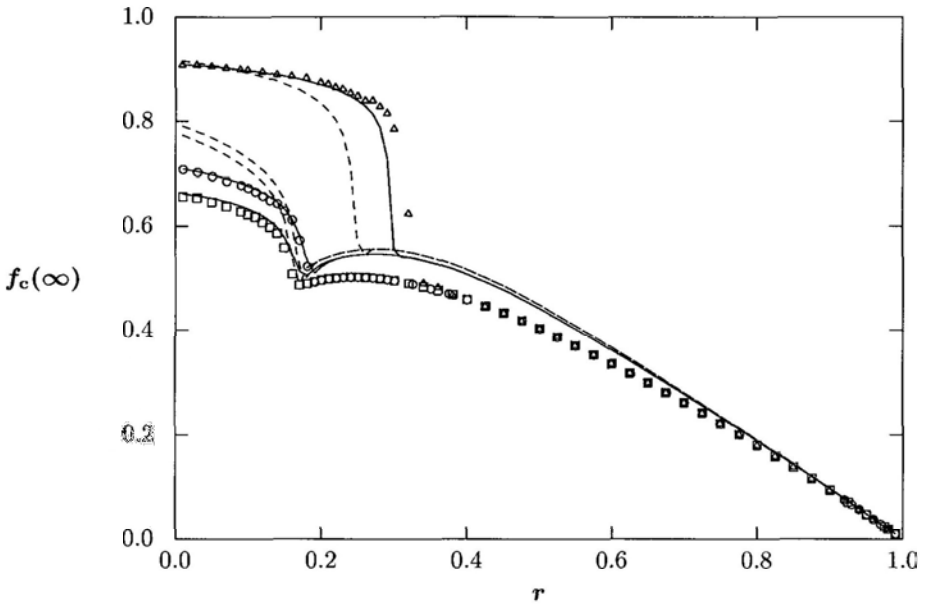

Figure 9.6: Long time limits of the fraction of cooperation. Symbols refer to simulation data and solid lines to MFT results obtained using the binomial closure. Dashed lines give MFT results using the SSC closure, equivalent to the previous strict mean-field approach that neglected fluctuations (see Sec. 8.3). System parameters: $f_c^i = 0.9$ (triangles, dark red); $f_c^i = 0.7$ (circles, blue); $f_c^i = 0.1$ (squares, light red).

9.3 Fixed-Point Analysis

From the model definition, it directly follows that the model enters a frozen state if there are only CC-links left, irrespective of the number of C- or D-nodes or the value of r. Within our phase space, this corresponds to an entire line consisting of fixed points, defined as $l_{CC} = k/2$ (and therefore $l_{CD} = 0$). These fixed points are *sticky* since once reached, no random fluctuations can change the system's configuration anymore. They correspond to the *disconnected* states of the network discussed before.

While our MFT strictly speaking does not include this case, the MFT equations can be continuously closed by defining $\Delta f_c(l_{CC} = k/2) = \Delta l_{CC}(l_{CC} = k/2) = \Delta l_{CD}(l_{CC} = k/2) = 0$. If r is low enough, it was found that systems starting from a random configuration typically end in such a frozen state. For larger values of $0.15 < r < 0.4$, the system could end in a frozen state if its initial fraction of cooperators was high enough [9]. Apart from this fixed point axis, setting Eqs. (9.5)-(9.7) to zero results in one other solution for every value $0 < r < 1$. For large values of r, this can be identified with the long time limit of trajectories previously shown, hence this solution represents the *connected* state of the network. However, for small values of r, a disconnected-connected transition was observed, depending on the initial state of the network. In particular, for values $r < 0.15$, only disconnected final states were observed, while the MFT equations still predict a fixed point with finite positive values of l_{CD} and l_{DD}.

To further investigate this issue, we need to analyse the stability of the isolated fixed point. First, it should be stressed that a single solution[1] is

[1]There exists only one isolated fixed point inside the accessible phase space. If the MFT equations are set to zero, other solutions are found which do not constitute fixed points since they are outside the accessible phase space

found for any value of $0 < r < 1$ We show the f_c-coordinate of this solution, together with the f_c-value of the long time limit, in Fig 9 7(A) For large values of r, both values are identical For small values of r, the long time limits branch off as the systems reach the disconnected state (dotted line) The MFT equations, however, predict another fixed point whose fraction of cooperation decreases with decreasing r

The stability of a fixed point can be analysed by calculating the Jacobian matrix of the equations of motion at the fixed point If the real parts of all its eigenvalues are negative then small fluctuations away from the fixed point will be driven towards the fixed point again, and the fixed point will be stable against small disturbances

Figure 9 7 shows the negated real parts of the eigenvalues $-\Re(\eta_i)$ of the Jacobian matrix of the single fixed point, for clarity shown on a log scale As expected, for large values of r all eigenvalues are clearly negative, indicating a stable fixed point Strictly speaking, this holds true even for small values of r, as all eigenvalues remain negative However, while one eigenvector becomes more and more attractive, with its eigenvalue diverging to $\lim_{r\to 0} \Re(\lambda_1) = -\infty$, the other eigenvectors become less and less attractive, with their eigenvalues converging against zero Hence, unlike previously observed in other models [94, 95], our system does not undergo any bifurcations Rather, a gradually shrinking basin of attraction of the stable fixed point reduces the number of configurations that can be drawn towards it At the same time, random fluctuations can cause systems within the basin of attraction of the stable fixed point to leave this basin and end in a sticky fixed point Such effects significantly reduce the lifetime of the stable fixed point

To test the existence of the single fixed point for small values of r, we run Monte Carlo (MC) simulations that sweep r from $r = 1 \to 0$ Starting from $r =$

1, we run 10^5 MC steps and record the mean, the standard deviation and the maximal and minimal values of the global variables. Afterwards, r is decreased by 0.005, and the system is allowed to equilibrate for 10^4 MC steps before the same cycle is repeated. Figure 9.8 shows the simulation results. Figure 9.8(A) shows the time-average of f_c. The minimal/maximal values during the simulation run are indicated by the error bars. While the deviations between theory and simulation exceed the fluctuations observed in the simulation, the simulation nonetheless confirms the existence of the stable fixed point down to $r = 0.05$. In particular, the predicted decrease in f_c^∞ for lower r is also confirmed. This means that, if the temptation is allowed to vary during a system's evolution, reduced temptation can actually result in decreased cooperation. This non-monotonous reaction is very surprising, since it shows that even if every agent acts in a very rational manner, the overall response of a system as a whole can be irrational nonetheless.

For values below $r = 0.05$, the system's fluctuations can make it enter a frozen state, and therefore oblivious to changes in r. Although MFT still predicts a stable fixed point, this fixed point is now short-lived. For one, the fluctuations of the system increase, as shown in Fig. 9.8(C). This agrees with the MFT prediction that all but one eigenvalue of the system's Jacobian vanish, allowing for larger fluctuations. At the same time, the predicted stable CC-link density approaches the sticky axis, making it possible for fluctuations to reach a frozen state (see Fig. 9.8(B)).

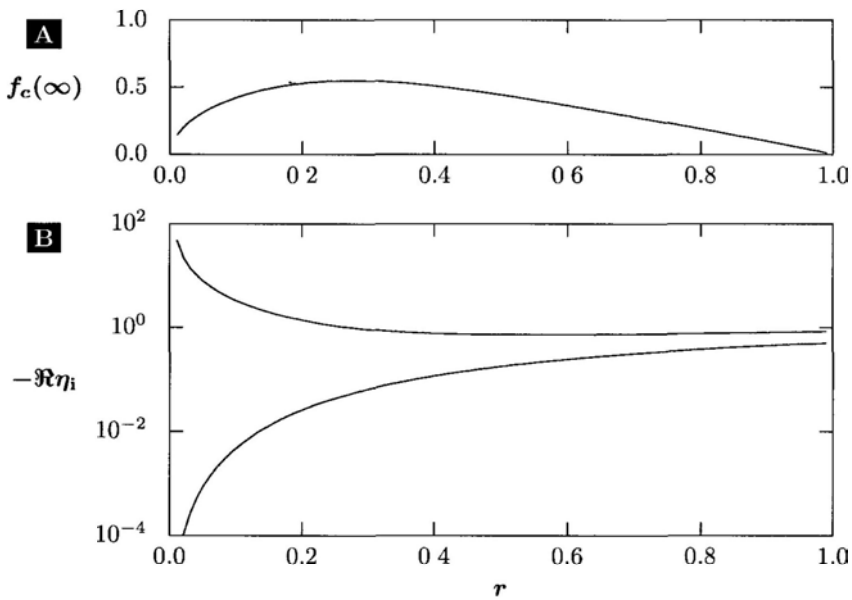

Figure 9.7: (A): f_c-values of the single fixed point and of the disconnected branch of the long time limit of trajectories starting at $f_c^i = 0.5$ (dashed). (B): negative real part of the eigenvalues $-\mathcal{R}(\eta_i)$ of the Jacobian of the single fixed point. The strongly attractive eigenvalue η_1 is plotted as a solid red line. The real parts of the two weakly attractive complex eigenvalues are identical and plotted as the blue line.

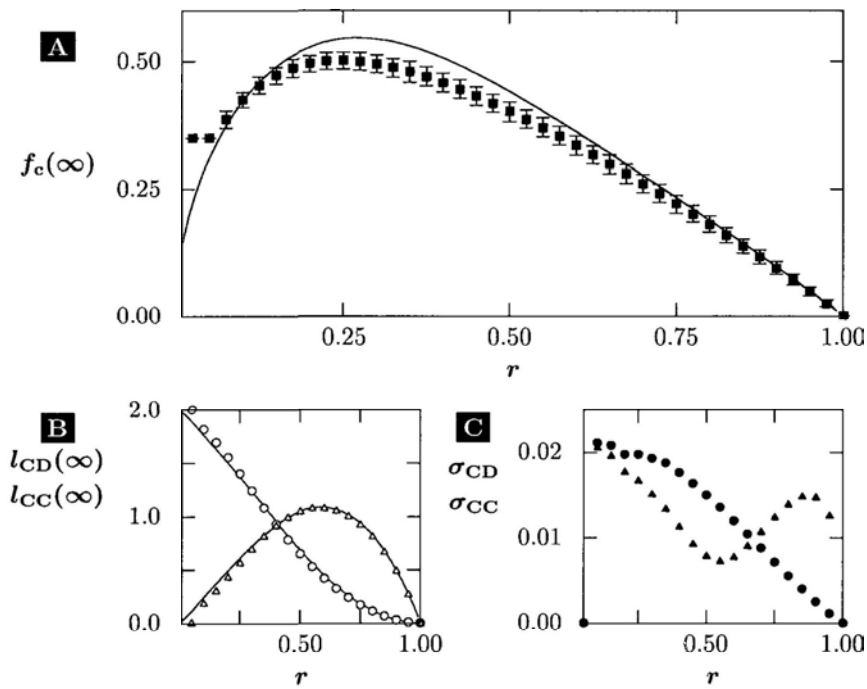

Figure 9.8: Simulation results obtained by tracing $r \to 0$. (A):f_c^{∞}, with error bars indicating upper and lower bounds. (B): l_{CC} (circles) and l_{CD} (triangles). (C): standard deviation of l_{CC}(circles) and l_{CD}(triangles). The standard deviation increases in accordance with $\Re(\eta_{2/3}) \to 0^-$, as shown in Fig. 9.7. All figures: simulation results as symbols, MFT results as lines.

9.4 Mean Degree Dependence

So far, all results referred to a model system consisting of $N = 10000$ agents having on average $k = 4$ neighbours. The number of nodes in total should not significantly influence the system's dynamics, since all occurring events have only a local impact, i.e., within a single node's neighbourhood. Still, the system's sensitivity to random fluctuations might require a certain minimal network size. On the contrary, the connectivity, i.e., the number of neighbours an agent typically has, can alter the model's dynamics. However, unlike the case of the aforementioned epidemic models, the effects of connectivity on cooperation are less obvious to predict.

Figure 9.9 shows the long time limit of the fraction of cooperation for three systems with different connectivity, starting from $k = 2$ (which means disconnected fragments unless all agents form a perfect ring) to $k = 100$. Simulation results are shown as symbols. Open symbols give the f_c if the system does not start from a random network, but instead starts from the previous system's final state with r being incrementally decreased (see Sec.9.3). MFT results are shown as lines, with solid lines showing the long time limit for systems starting at $f_c^i = 0.5$ and the dashed lines showing the f_c-value of the isolated fixed point, if different.

All three systems show a qualitatively similar behaviour. Starting from $r = 1$, reducing temptation leads to increased cooperation. However, after a certain value of r_{max} : $\partial_r f_c^\infty(r_{max}) = 0$, cooperation starts to shrink. If the system originally starts from a random network, a disconnected-connected transition will occur at some value of $r < r_{max}$. The fraction of cooperation in these disconnected systems then again increases with decreasing temptation r.

However, there are significant quantitative differences between the different

systems. Overall, a higher connectivity generally increases the fraction of cooperation. It also pushes the onset of the disconnected-connected transition to lower values[2] of r.

Another notable point is that the deviations between MFT and simulations also show a clear dependency on the mean degree of the network. While deviations are most notable for connected networks with a low mean degree, deviations are barely noticeable in the case of $k = 100$. The reason for this is twofold. For one, in the case of a low mean degree, many isolated D-nodes exist which, if chosen for trial, will not contribute to the system's dynamics. This issue occurs only for D-nodes since C-nodes, unless initially disconnected, never lose a neighbour. It is not yet adequately addressed by our decoupling approximation (Eq.(9.13)). For another, deviations can arise since even the improved moment closure does not yet exactly agree with the degree distribution observed in simulations. However, the relative importance of these deviations diminishes for systems with higher connectivity.

[2]Given the larger f_c^∞ of disconnected systems, this can actually lead to (disconnected) systems of lower k to have a higher f_c^∞ than connected systems of higher k at the same value of r.

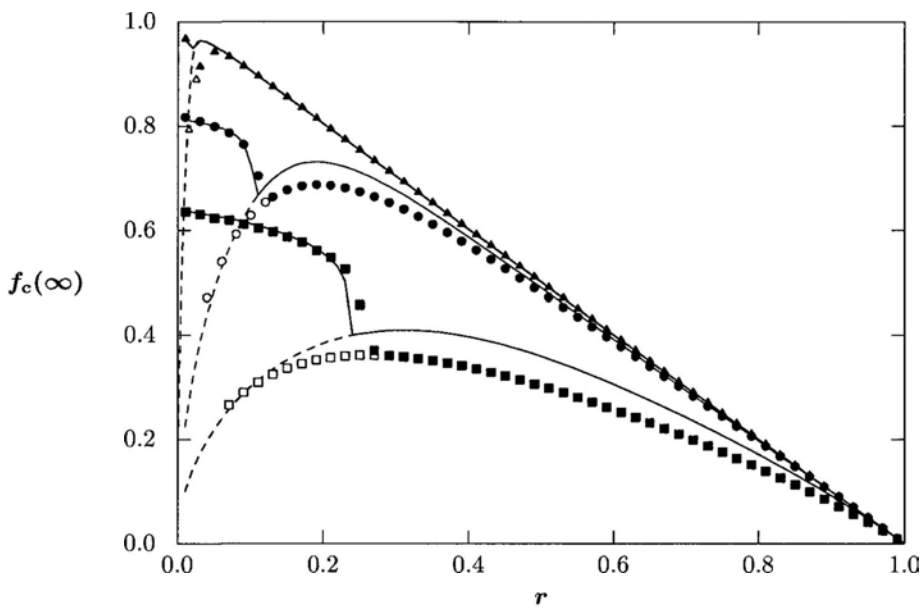

Figure 9.9: Long time limits for f_c for various degrees of connectivity: $k = 100$ (red triangles), $k = 10$ (purple circles) and $k = 2$ (blue squares). Solid symbols refer to systems starting from a random network with $f_c^i = 0.5$, while open symbols refer to systems obtained by tracing r. Solid lines give the MFT long time limits for such systems. Dashed lines show the isolated fixed point, if different from the long time limit.

9.5 Conclusion and Outlook

A new mean-field closure for the dissatisfied-adaptive Snowdrift Game was introduced The assumptions required to close the mean-field theory were discussed in detail and compared to assumptions made in previous and comparable models We introduced the criteria $\lim_{\mathcal{P}(opp)\to 0} \Lambda = \lim_{\mathcal{P}(opp)\to 1} \Lambda = 0$ and $\Lambda < 0$ that have to be fulfilled for a closure to be valid and showed why previously successful closures violate these criteria in the case of the dissatisfied adaptive Snowdrift Game Using our mean-field closure we showed that two stable fixed points exist for any value of the temptation parameter r, corresponding to a connected and a disconnected state, respectively The connected state in the small-r limit shows a counter-intuitive behaviour, as a decrease in the temptation parameter r leads to a decrease in the fraction of cooperation We performed computer simulations to trace this previously undetected state, and applied a fixed-point stability analysis to show why fluctuations can turn the connected state into a disconnected state for very small r Finally, we showed that the DASG-model's emergence of cooperation is strongly dependant on the mean degree k, but that qualitatively the atypical behaviour $\lim_{r\to 0} f_c(\infty) \to 0$ occurs for all values of k in both MFT and simulation Furthermore, it is shown that the main error in our MFT assumptions diminishes for systems with large degree k

We believe that the contribution of this work is twofold For one, we show how collective dynamics can even if every single agent acts purely rational, lead to a very irrational reaction of the system namely a suppression of cooperation if the temptation is gradually reduced For another we believe that our introduced criteria will allow to derive mean-field theories for other co-evolving models Given that fixed-point and stability analyses can point

towards non-obvious and possible overlooked dynamical features, we expect that additional insight could be gained from a variety of social, economical or biological adaptive models.

Of course, as it is usually the case with works in the field of complex systems, the question whether or not our system is an appropriate model for the emergence of cooperation between humans remains unclear. Experimental studies could shed light on this question, but such an investigation would exceed the scope of this thesis. We nevertheless hope to perform such studies in the near future. However, two problems arise that have to be handled very carefully for any comparison to be worthwhile. First, pre-existing relationships between participants have to be controlled for, which will require very careful anonymising of the interaction between participants. Second, human intelligence might make participants exploit scenarios that were unaccessible to our agents. For example, since every interaction offers a positive payoff, a human player might just try to maximise his number of connections. He or she might disregard any sense of fairness, which would exist in a real-world competitive scenario. Second, experimental social setups are often not treated seriously by participants, and therefore their utility function might not be linear. This means that a player might not try to maximise its payoff, but maybe rather employ a all-or-nothing strategy – again something unlikely in real life[3] . Therefore, offering participants a reasonable scenario might be the paramount problem in the setup of an experimental realisation.

[3] Among friends of the author of this thesis, who all are avid board game players, such behaviour is commonly called the *Frank effect*, after one particular player who starts to act erratic once he finds out he will not win this round.

Appendix A

Node-Level Derivation of the Snowdrift Game's Mean-Field Theory

In this appendix, we will derive the equations of motion for the global variables of the dissatisfied-adaptive Snowdrift Game model from node level. These form the basis of the mean-field theories derived in Ch. 9. We start with the rules of the model for a single trial:

1. A single random node is picked as the *player*.
2. Among its neighbours, if any, one is randomly selected as its *opponent*.
3. The nodes play one round of the Snowdrift Game. The game ends here if the opponent is cooperative and the player is thus satisfied.
4. If the opponent was a D-node and the player is now dissatisfied, it will randomly but with pre-defined probabilities choose exactly one of the two possible reactions.

(a) Break the link to its opponent and rewire to another, randomly chosen node

(b) Switch its own character, from $C \to D$ or vice versa

If we knew the detailed configuration of the system, we could write the expected change in a macroscopic variable as a sum over all possible trials times their probability and outcome

$$\Delta X = \sum_{T=C,D} \mathcal{P}^{(T)} \sum_{\kappa=1}^{\infty} \mathcal{P}_T^{(\kappa)} \sum_{\lambda_{CD}=0}^{\kappa} \mathcal{P}_{T,\kappa}^{(\lambda_{CD})} \times \mathcal{P}_T^{(TD)} \sum_{E=R,S} \mathcal{P}_T^{(E)} \Delta X(T, E, \kappa, \lambda_{CD}) \tag{A 1}$$

As before $\mathcal{P}_Y^{(X)}$ refers to the conditional probability of event X to happen under condition Y. These probabilities are in detail

1. $\mathcal{P}^{(T=C,D)}$ to pick a C- or D-node as the player, i.e., trial step 1. These probabilities are just the density of C- and D-nodes and can be expressed as $\mathcal{P}(C) = N_C/N$, $\mathcal{P}^{(D)} = N_D/N$.

2. $\mathcal{P}_T^{(\kappa)}$ that this T-node has κ neighbours in total.

3. $\mathcal{P}_{T,\kappa}^{(\lambda_{CD})}$, that a node of type T with degree κ has λ_{CD} neighbours of the opposite type.

4. $\mathcal{P}_{\kappa,\lambda_{CD}}^{TD}$, that, among its neighbours, a D-node is picked as the opponent (trial steps 2&3). This probability is given through $\mathcal{P}_{0,\lambda_{CD}}^{TD} = 0$ for nodes with degree zero, $\mathcal{P}_{\kappa,\lambda_{CD}}^{CD} = \lambda_{CD}/\kappa$ for C-nodes with $\kappa > 0$, and $\mathcal{P}_{\kappa,\lambda_{CD}}^{DD} = 1 - \lambda_{CD}/\kappa$ for D- nodes with $\kappa > 0$.

5. $\mathcal{P}_T^{(E=R,S)}$ that a dissatisfied node of type T carries out action E, which can be rewiring or switching (trial step 4).

$\Delta X(T, E, \kappa, \lambda_{CD})$ is the resulting change in the global variable $X \in \{N_C, L_{CC}, L_{CD}\}$, caused by event E at a node of type T with κ neighbours and λ_{CD} neighbours of opposite type

Equation (A 1) is an exact description of the expected evolution of these variables However every trial ends in one discrete outcome which is not necessarily close, let alone equal to the expected change Such fluctuations can cause deviations between theory and simulations, even when no additional assumptions are made 1

Consider first the change in the global variables that a single event causes Four kinds of player-opponent combinations can be chosen for a trial $C \to C$, $C \to D$, $D \to C$ and $D \to D$ For a purely dissatisfied-adaptive game, only dissatisfied combinations, i e , combinations with a D-opponent, will cause a reaction

Generally, the results of a rewiring-event are simpler than those of a switching-event No node changes its status hence

$$\Delta N_C(C, R, \kappa, \lambda_{CD}) = \Delta N_C(D, R, \kappa, \lambda_{CD}) = 0 \qquad \text{(A 2)}$$

However rewiring will cut one CD-link (or DD-link) , respectively A new connection is established to a randomly chosen node whose status, at time of rewiring, is unknown Hence, whether a link of the same type or a CC-link (CD-link) is established depends only on the likelihood of choosing a C-node as the new neighbour

$$\begin{aligned}
\Delta L_{CC}(C, R\ \kappa, \lambda_{CD}) &= 1\ \ f_c + 0\ \ (1 - f_c) = f_c \\
\Delta L_{CC}(D, R, \kappa, \lambda_{CD}) &= 0\ \ f_c + 0\ \ (1 - f_c) = 0 \\
\Delta L_{CD}(C, R, \kappa, \lambda_{CD}) &= -1\ \ f_c + 0\ \ (1 - f_c) = -f_c \\
\Delta L_{CD}(D, R, \kappa, \lambda_{CD}) &= 1\ \ f_c + 0\ \ (1 - f_c) = f_c \qquad \text{(A 3)}
\end{aligned}$$

It is important to note that this is only the *expected* change of the macroscopic quantity, the real change of course will never be a fraction but instead either zero or one.

For switching events, the outcome is in general more complicated. It depends on the player's status and neighbourhood. but not on the network's global configuration. The changes to the number of cooperative nodes are trivial:

$$\Delta N_C(C, S, \kappa, \lambda_{CD}) = -\Delta N_C(D, S, \kappa, \lambda_{CD}) = -1 \ . \tag{A.4}$$

The changes to the number of links are more complicated as they depend on the player's degree κ and its number of CD-links

$$\begin{aligned}
\Delta L_{CC}(C, S, \kappa, \lambda_{CD}) &= -\lambda_{CC} = -\kappa + \lambda_{CD} \\
\Delta L_{CC}(D, S, \kappa, \lambda_{CD}) &= \lambda_{CD} \\
\Delta L_{CD}(C, S, \kappa, \lambda_{CD}) &= \lambda_{CC} - \lambda_{CD} = \kappa - 2\lambda_{CD} \\
\Delta L_{CD}(D, S, \kappa, \lambda_{CD}) &= \lambda_{DD} - \lambda_{CD} = \kappa - 2\lambda_{CD} \ .
\end{aligned} \tag{A.5}$$

Having found all these changes, we can go one step back and ask what the expected change is if we already chose one node as the player. Such a node can be of C- or D-type. will have a degree κ and a number of CD-links $\lambda_{CD} \leq \kappa$. The conditional probabilities to choose a dissatisfied link now is

$$\begin{aligned}
\mathcal{P}_C^{(CD)}(\kappa, \lambda_{CD}) &= \begin{cases} \frac{\lambda_{CD}}{\kappa} & \kappa > 0 \\ 0 & \kappa = 0 \end{cases} \\
\mathcal{P}_D^{(DD)}(\kappa, \lambda_{CD}) &= \begin{cases} \frac{\kappa - \lambda_{CD}}{\kappa} & \kappa > 0 \\ 0 & \kappa = 0 \end{cases} \ .
\end{aligned} \tag{A.6}$$

Having to treat the case $\kappa = 0$ separately is a cumbersome technicality. Nonetheless, the averaging process over those terms are among the causes

of some of the observed deviations between MFT and simulations In the following, we will mostly omit the special treatment and assume $\kappa > 0$ We will discuss this assumption specifically in those cases where it affects the validity of the MFT

If a dissatisfied link is chosen the probabilities $\mathcal{P}_C^{(S)}$ $\mathcal{P}_C^{(R)}$ $\mathcal{P}_D^{(S)}$ and $\mathcal{P}_D^{(R)}$ determine which event will occur Hence, the expected changes when choosing a node of a certain type for trial become

$$\begin{aligned}
\Delta N_C(C,\kappa,\lambda_{CD}) &= -\frac{\lambda_{CD}}{\kappa}\mathcal{P}_C^{(S)} \\
\Delta N_C(D,\kappa,\lambda_{CD}) &= \left(1-\frac{\lambda_{CD}}{\kappa}\right)\mathcal{P}_D^{(S)} \\
\Delta L_{CC}(C,\kappa,\lambda_{CD}) &= \frac{\lambda_{CD}}{\kappa}\left(-\left(\kappa-\lambda_{CD}\right)\mathcal{P}_C^{(S)}+f_c\mathcal{P}_C^{(R)}\right) \\
&= \left(\frac{\lambda_{CD}^2}{\kappa}-\lambda_{CD}\right)\mathcal{P}_C^{(S)}+f_c\frac{\lambda_{CD}}{\kappa}\mathcal{P}_C^{(R)} \\
\Delta L_{CC}(D,\kappa,\lambda_{CD}) &= \left(1-\frac{\lambda_{CD}}{\kappa}\right)\lambda_{CD}\mathcal{P}_D^{(S)} = -\left(\frac{\lambda_{CD}^2}{\kappa}-\lambda_{CD}\right)\mathcal{P}_D^{(S)} \\
\Delta L_{CD}(C,\kappa,\lambda_{CD}) &= \frac{\lambda_{CD}}{\kappa}\left(\left(\kappa-2\lambda_{CD}\right)\mathcal{P}_C^{(S)}-f_c\mathcal{P}_C^{(R)}\right) \\
&= \left(\lambda_{CD}-2\frac{\lambda_{CD}^2}{\kappa}\right)\mathcal{P}_C^{(S)}-\frac{\lambda_{CD}}{\kappa}f_c\mathcal{P}_C^{(R)} \\
\Delta L_{CD}(D\kappa,\lambda_{CD}) &= \left(1-\frac{\lambda_{CD}}{\kappa}\right)\left(\left(\kappa-2\lambda_{CD}\right)\mathcal{P}_D^{(S)}+f_c\mathcal{P}_D^{(R)}\right) \\
&= \left(\kappa-3\lambda_{CD}+2\frac{\lambda_{CD}^2}{\kappa}\right)+\left(1-\frac{\lambda_{CD}}{\kappa}\right)f_c\mathcal{P}_D^{(R)} \quad \text{(A 7)}
\end{aligned}$$

At last, we have to include the sums over the probabilities to choose a node of a certain type and configuration as the player Generally, we will treat nodes of opposite type explicitly,i e we will carry out the sum over $\mathcal{P}_T$ The other two probability distributions, $\mathcal{P}_T^{(\kappa)}$ and $\mathcal{P}_{T\,\kappa}^{(\lambda_{CD})}$, remain unknown However, it is important to notice that we do not need the exact distributions at all since, by summing over all nodes, they will results in the expectation values of the terms in Eqs (A 7) Hence, we can write the final set of equations for the

global variables as

$$\begin{aligned}
\Delta N_C &= (1-f_c)\left(1-\left\langle\frac{\lambda_{CD}}{\kappa}\right\rangle_D\right)\mathcal{P}_D^{(S)} - f_c\left\langle\frac{\lambda_{CD}}{\kappa}\right\rangle_C\mathcal{P}_C^{(S)} \\
\Delta L_{CD} &= f_c\mathcal{P}_C^{(S)}\left(\langle\lambda_{CD}\rangle_C - 2\left\langle\frac{\lambda_{CD}^2}{\kappa}\right\rangle_C\right) - f_c^2\mathcal{P}_C^{(R)}\left\langle\frac{\lambda_{CD}}{\kappa}\right\rangle_C \\
&+ (1-f_c)\mathcal{P}_D^{(S)}\left(\langle\kappa\rangle_D - 3\langle\lambda_{CD}\rangle_D + 2\left\langle\frac{\lambda_{CD}^2}{\kappa}\right\rangle_D\right) \\
&+ f_c(1-f_c)\mathcal{P}_D^{(R)}\left(1-\left\langle\frac{\lambda_{CD}}{\kappa}\right\rangle_D\right) \\
\Delta L_{CC} &= f_c\mathcal{P}_C^{(S)}\left(\left\langle\frac{\lambda_{CD}^2}{\kappa}\right\rangle_C - \langle\lambda_{CD}\rangle_C\right) + f_c^2\mathcal{P}_C^{(R)}\left\langle\frac{\lambda_{CD}}{\kappa}\right\rangle_C \\
&+ (1-f_c)\mathcal{P}_D^{(S)}\left(\langle\lambda_{CD}\rangle_D - \left\langle\frac{\lambda_{CD}^2}{\kappa}\right\rangle_D\right) . \qquad \text{(A.8)}
\end{aligned}$$

These equations are still exact. However, it should be noted that the averaging process for the expectation values now has to take the cases with $\kappa = 0$ into account. When taking averages, zero-over-zero-fractions have to be evaluated according to Eq. (A.6), i.e. typically as zero. To be usable, this system of equations needs to be closed using some approximation scheme for the fractions and the second moment, as discussed in Chs. 8-9.

Appendix B

Mean-Field Theory Derivation for the Adaptive SIS Model Using Link Triplets

Gross *et al* originally defined the rules of the adaptive SIS model in Ref [7] To describe the state of the model, they used three macroscopic variables The number of infected nodes N_I, the number of links between two susceptible nodes L_{SS}, and of links between two infected nodes L_{II} As the total number of nodes N, the mean degree k and thus the total number of links $L_{\text{tot}} = Nk/2$ is kept constant, the number of susceptible nodes $N_S = N - N_I$ and of links between a susceptible and an infected node $L_{SI} = L_{\text{tot}} - L_{SS} - L_{II}$ can both be calculated directly from these variables

The configuration of the system can change through three different events $E \in \{SP, R, RW\}$

1 A susceptible node can contract the disease from one of its infected neighbours with rate τ $(E = SP)$

2 An infected node can recover from the disease with rate r ($E = R$)

3 A healthy node can cut a link to an infected neighbour with rate ω and establish a new connection to a randomly chosen susceptible node which is not yet among its neighbours ($E = RW$)

The frequency of all three events is given in terms of rates. During the discrete time step δt of a simulation these rates turn into probabilities, e.g., $\mathcal{P}(R) = r \times \delta t$. For convenience sake, we will express the time in units of δt, which means that rates and probabilities have the same numerical value. It is important, though, to understand that the rates are defined for a continuous time model. In continuous time two events never occur at the same instant. In discrete time, they may occur within the same time step. The rate at which a susceptible node with three infected neighbours contracts the disease is equivalent to 3τ. The probability for the same node to contract the disease during a simulation step, however, is $3\tau - 3\tau^2 + \tau^3$. We therefore have to choose the time step short enough such that the rates, expressed in this time unit, are small enough to make events of higher order negligible.

The easiest event to describe in a mean-field model is the rewiring event $E = RW$. With probability ω, every SI-link will turn into an SS-link. On average this means

$$\Delta L_{CC}(RW) = \omega \times L_{SI} \tag{B 1}$$

Neither the number of infected nodes nor the number of II-links are affected in such an event.

The recovery event $E = R$ occurs at every infected node with the same probability. The change in the number of infected nodes is thus

$$\Delta N_I(R) = -r \times N_I \tag{B 2}$$

An II-link will turn into an SI-link if either of the nodes at its ends recovers. Similarly, an SI-link turns into an SS-link if its I-node recovers. The change in the link numbers is thus

$$\begin{aligned} \Delta L_{II}(R) &= -2r \times L_{II} \\ \Delta L_{SS}(R) &= r \times L_{SI} \ . \end{aligned} \tag{B.3}$$

As discussed before, events of higher order are ignored, i.e., we do not include a transition of an II-into an SS-link when both nodes recover.

The infection spreading process $E = SP$ is more complicated. Generally, every SI-link can infect its S-node with probability τ:

$$\Delta N_I(SP) = \tau \times L_{SI} \ . \tag{B.4}$$

The impact on the links is less easy to determine. Obviously, the links that spread the infection turn from SI- into II-links:

$$\Delta_1 L_{II}(SP) = \tau \times L_{SI} \ . \tag{B.5}$$

But the spreading infection also affects all other links connected to the node that became infected. We can describe these effect using triplets. Fig. B.1 shows such a scenario. In Fig. B.1(A), the disease will spread from the lower node to the centre node. It will turn all other SI-links connected to this node into II-links. These links together form triplets $I \rightarrow S \rightarrow I$. Every SI-link that spreads the infection will hence create another II-link for every triplet that it is part of. Figure B.1(B) sums up the effects of this process, illustrating the three existing SI-links and the resulting six ISI-triplets. Triplets are counted in an oriented way, hence every triplet is counted in two directions. The resulting change is

$$\Delta_2 L_{II}(SP) = \tau \times L_{ISI} \ . \tag{B.6}$$

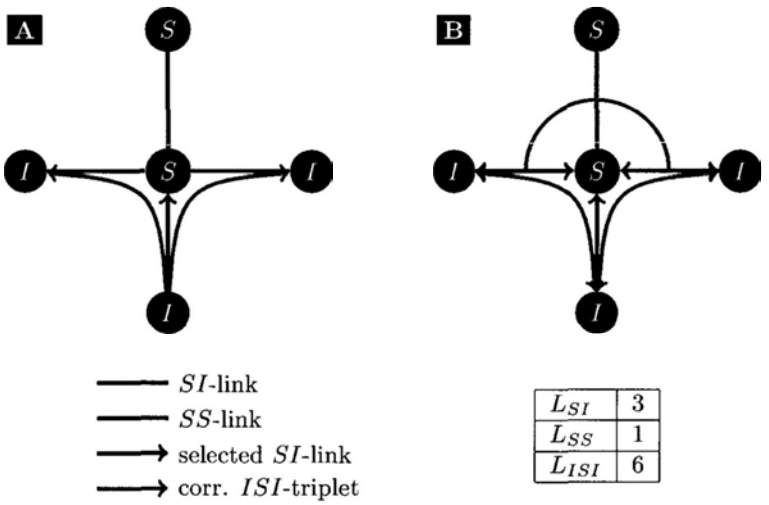

Figure B.1: ISI-triplets and their effects in infection spreading. (A) Spread over a single SI-link and the associated ISI-triplets. (B) All SI-links and associated ISI-triplets.

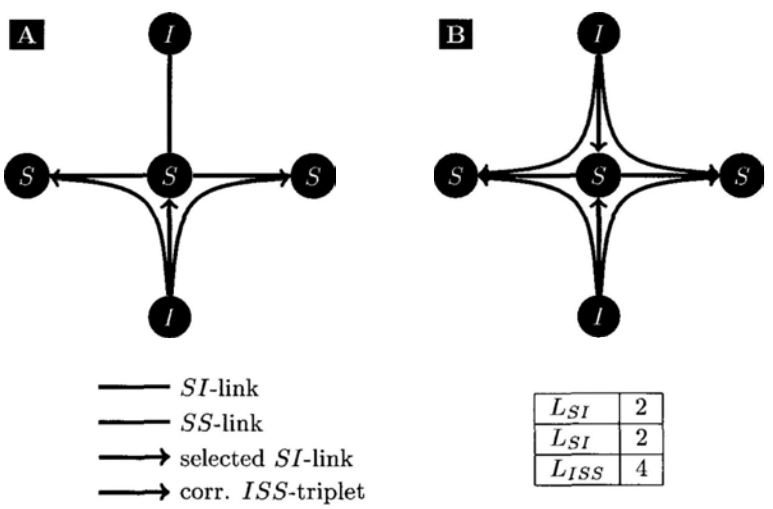

Figure B.2: ISS-triplets and their effects in infection spreading. (A) Spread over a single SI-link and the associated ISS-triplet. (B) All SI-links and associated ISS-triplets.

In a similar manner, a SI-link that spreads the disease to a susceptible node turns all SS-links of this node into SI-links. Such configurations form $I \to S \to S$ triplets. The situation is shown in Fig. B.2. Figure B.2(A) shows the ISS-triplets associated to single SI-link, and Fig. B.2(B) shows the total number of links and triplets for the same situation. We can write the link changes through this effect as

$$\Delta^3 L_{SS}(SP) = -\tau \times L_{ISS} \tag{B.7}$$

Summing up all these contributions, the expected changes during one step are

$$\begin{aligned} \Delta N_I &= \tau L_{SI} - r N_I \\ \Delta L_{SS} &= (r+\omega) L_{SI} - \tau L_{ISS} \\ \Delta L_{II} &= \tau L_{SI} + \tau L_{ISI} - 2r L_{II} \end{aligned} \tag{B.8}$$

To obtain a closed system of equations of motion, we need to express the number of link triplets in terms of our variables. According to Keeling and Eames [10, 78], the number of triplets of arbitrary type $A \to B \to C$ can be expressed as

$$L_{ABC} = \frac{L_{AB} L_{BC}}{N_B} \tag{B.9}$$

For our triplets, this means

$$\begin{aligned} L_{ISI} &= \frac{L_{SI}^2}{N_S} \\ L_{ISS} &= \frac{2 L_{SS} L_{SI}}{N_S} \,, \end{aligned} \tag{B.10}$$

with an added factor two for ISS-triplets since either S-node of a SS-link can take the place of the central node in the triplet. The resulting set of equations

is

$$\begin{aligned}\Delta N_I &= \tau L_{SI} - rN_I \\ \Delta L_{SS} &= (r+\omega)L_{SI} - \tau\frac{2L_{SI}L_{SS}}{N_S} \\ \Delta L_{II} &= \tau L_{SI} + \tau\frac{L_{SI}^2}{N_S} - 2rL_{II} \ . \end{aligned} \tag{B.11}$$

and for the remaining variables

$$\begin{aligned}\Delta N_S &= rN_I - \tau L_{SI} \\ \Delta L_{SI} &= \tau\frac{2L_{SI}L_{SS}}{N_S} + 2rL_{II} - \tau L_{SI} - \tau\frac{L_{SI}^2}{N_S} - (r+w)L_{SI} \ . \end{aligned} \tag{B.12}$$

An interesting consequence of this moment closure should be noted. At a single S-node, the number of ISI-triplets with this node as its centre is

$$\lambda_{ISI} = \lambda_{SI}(\lambda_{SI} - 1) \ . \tag{B.13}$$

We used greek symbols here since we are referring to the quantities of a single node. The number of total triplet is thus given by

$$L_{ISI} = \sum_{n=1}^{N_S}[\lambda_{SI}(\lambda_{SI} - 1)]_n \ , \tag{B.14}$$

and consequently

$$\langle\lambda_{SI}(\lambda_{SI} - 1)\rangle_S = \langle\lambda_{SI}^2\rangle_S - \langle\lambda_{SI}\rangle_S = \frac{L_{ISI}}{N_S} = \frac{L_{SI}^2}{N_S^2} = \left(\frac{L_{SI}}{N_S}\right)^2 \ . \tag{B.15}$$

At the same time, we know that

$$\langle\lambda_{SI}\rangle_S = \frac{L_{SI}}{N_S} \ . \tag{B.16}$$

With this information, we can write for the variance of the distribution of SI-links at S-nodes

$$\begin{aligned}\sigma^2 &= \langle\lambda_{SI}^2\rangle - \langle\lambda_{SI}\rangle_S^2 = \langle\lambda_{SI}^2\rangle - \langle\lambda_{SI}\rangle + \langle\lambda_{SI}\rangle - \langle\lambda_{SI}\rangle^2 \\ &= \frac{L_{ISI}}{N_S} + \langle\lambda_{SI}\rangle - \langle\lambda_{SI}\rangle^2 = \frac{L_{SI}^2}{N_S^2} + \frac{L_{SI}}{N_S} - \frac{L_{SI}^2}{N_S^2} = \frac{L_{SI}}{N_S} = \mu \ . \end{aligned} \tag{B.17}$$

The variance and the mean of the underlying distribution of the moment closure are hence identical. A well known example fulfilling this requirement is the Poisson distribution.

Bibliography

[1] M Fuchs MCT results for a simple liquid at the glass transition *Transport Theory and Statistical Physics* **24**, 855–880 (1995)

[2] H Barnes Shear-thickening ("dilatancy") in suspensions of nonaggregating solid particles dispersed in newtonian liquids *Journal of Rheology* **33**, 329–366 (1989)

[3] O Graser and A Grimm Adaptive generalized periodic boundary conditions for lattice-Boltzmann simulations of pressure-driven flows through confined repetitive geometries *Phys Rev E* **82**, 016702 (2010)

[4] A Grimm and O Graser Obstacle design for pressure driven vector chromatography in microfluidic devices Submitted to *EPL* (2010)

[5] S Strogatz Exploring complex networks *Nature* **410**, 268–276 (2001)

[6] M E J Newman The physics of networks *Physics Today* **61** 11, 33–38 (2008)

[7] T Gross, C D'Lima, and B Blasius Epidemic dynamics on an adaptive network *Phys Rev Lett* **96**, 208701 (2006)

[8] O Graser C Xu and P M Hui Separatrices between healthy and endemic states in an adaptive epidemic model Submitted to *Physica A*

[9] O Graser, C Xu, and P M Hui Disconnected-connected network transitions and phase separation driven by co-evolving dynamics *EPL* **87**, 38003 (2009)

[10] M Keeling, D Rand, and A Morris Correlation models for childhood epidemics *Proc R Soc Lond B* **264**, 1149–1156 (1997)

[11] O Graser, C Xu, and P M Hui Manuscript in preparation (2010)

[12] S Kim and H Pitsch A generalized periodic boundary condition for lattice Boltzmann method simulation of a pressure driven flow in a periodic geometry *Phys Fluids* **19**, 108101 (2007)

[13] P Lallemand and L Luo Theory of the lattice Boltzmann method Acoustic and thermal properties in two and three dimensions *Phys Rev E* **68** 036706 (2003)

[14] P Lallemand and L Luo Theory of the lattice Boltzmann method Dispersion, dissipation, isotropy, galilean invariance, and stability *Phys Rev E* **61**, 6546–6562 (2000)

[15] J Latt *Hydrodynamic Limit of Lattice Boltzmann Equations* PhD thesis, Université de Geneve, Geneve Suisse/Switzerland (2007)

[16] Y H Qian and Y Zhou Higher-order dynamics in lattice-based models using the Chapman-Enskog method *Phys Rev E* **61**, 2103–2106 (2000)

[17] S. CHEN and G. DOOLEN. Lattice Boltzmann method for fluid flows. *Annu. Rev. Fluid. Mech.* **30**, 329–364 (1998).

[18] D. RAABE. Overview of the lattice Boltzmann method for nano-and microscale fluid dynamics in materials science and engineering. *Modelling Simul. Mater. Sci. Eng.* **12**, R13–R46 (2004).

[19] S. SUCCI. *The Lattice Boltzmann Equation for Fluid Dynamics and Beyond (Numerical Mathematics and Scientific Computation).* Oxford University Press USA, New York, NY, USA, 2001.

[20] M. C. SUKOP and D. T. JR THORNE. *Lattice Boltzmann Modeling: An Introduction for Geoscientists and Engineers.* Springer, Berlin, Germany, 1st edition, 2007.

[21] D. ROTHMAN and S. ZALESKI. Lattice-gas models of phase separation: interfaces, phase transitions, and multiphase flow. *Rev. Mod. Phys.* **68**, 1417–1479 (1994).

[22] U. FRISCH, B. HASSLACHER. and Y. POMEAU. Lattice-gas automata for the navier-stokes equation. *Phys. Rev. Lett.* **56**, 1505–1508 (1986).

[23] S. WOLFRAM. Cellular automaton fluids 1: Basic theory. *J. Stat. Phys.* **45**, 471–526 (1986).

[24] G. MCNAMARA and G. ZANETTI. Use of the Boltzmann equation to simulate lattice-gas automata. *Phys. Rev. Lett.* **61**, 2332–2335 (1988).

[25] P. BHATNAGAR, E. GROSS, and M. KROOK. A model for collision processes in gases. I. Small amplitude processes in charged and neutral one-component systems. *Physical Review* **94**, 511–525 (1954).

[26] H. CHEN, S. CHEN, and W. MATTHAEUS. Recovery of the Navier-Stokes equations using a lattice-gas Boltzmann method. *Phys. Rev. A* **45**, 5539–5542 (1992).

[27] T. KRÜGER, F. VARNIK, and D. RAABE. Shear stress in lattice Boltzmann simulations. *Phys. Rev. E* **79**, 046704 (2009).

[28] S. CHEN, Z. WANG, X. SHAN, and G. DOOLEN. Lattice Boltzmann computational fluid dynamics in three dimensions. *J. Stat. Phys.* **68**, 379–400 (1992).

[29] G. P. GALDI. *An introduction to the mathematical theory of the Navier-Stokes equations. Vol. I.* volume 38 of *Springer Tracts in Natural Philosophy.* Springer USA, New York, NY, USA, 1994.

[30] P. LAVALLÉE, J. BOON, and A. NOULLEZ. Boundaries in lattice gas flows. *Physica D* **47**, 233–240 (1991).

[31] I. GINZBURG and D. D'HUMIÈRES. Multireflection boundary conditions for lattice Boltzmann models. *Phys. Rev. E* **68**, 066614 (2003).

[32] Q. ZOU and X. HE. On pressure and velocity boundary conditions for the lattice Boltzmann BGK model. *Phys. Fluids* **9**, 1591–1598 (1997).

[33] J. LATT, B. CHOPARD, O. MALASPINAS, M. DEVILLE, and A. MICHLER. Straight velocity boundaries in the lattice Boltzmann method. *Phys. Rev. E* **77**, 056703 (2008).

[34] J. BUICK and C. GREATED. Gravity in a lattice Boltzmann model. *Phys. Rev. E* **61**, 5307–5320 (2000).

[35] Z. GUO, C. ZHENG, and B. SHI. Discrete lattice effects on the forcing term in the lattice Boltzmann method. *Phys. Rev. E* **65**, 046308 (2002).

[36] D. KANDHAI, A. KOPONEN, A. HOEKSTRA, and M. KATAJA. Implementation aspects of 3D lattice-BGK: boundaries, accuracy, and a new fast relaxation method. *Journal of Computational Physics* **150**, 482–501 (1999).

[37] J. ZHANG and D. Y. KWOK. Pressure boundary condition of the lattice Boltzmann method for fully developed periodic flows. *Phys. Rev. E* **73**, 047702 (2006).

[38] RICHARD C. DORF AND ROBERT H. BISHOP. *Modern Control Systems.* Prentice Hall, Upper Saddle River, New Jersey, USA.

[39] L. HUANG, E. COX, R. AUSTIN, and J. STURM. Continuous particle separation through deterministic lateral displacement. *Science* **304**, 987 (2004).

[40] D. CAMPBELL-FALCK, T. THOMAS, T. M. FALCK, N. TUTUO, and K. CLEM. The intravenous use of coconut water. *The American Journal of Emergency Medicine* **18**, 108 – 111 (2000).

[41] J. SAMBROOK. *Molecular Cloning: A Laboratory Manual (3-Volume Set).* Cold Spring Harbor Laboratory Press, Woodbury, NY, USA, 3rd edition, 2001.

[42] M. VON SMOLUCHOVSKI. Experimentell nachweisbare, der üblichen Thermodynamik widersprechende Molekularphänomene. *Phys. Zeitschr.* **8**, 1069–1080 (1912).

[43] R. P. FEYNMAN, R. B. LEIGHTON, and M. SANDS. The Feynman Lectures On Physics. Vol. I, Ch. 46. Addison Wesley Longman, Reading, MS, USA, 1998.

[44] M MAGNASCO and G STOLOVITZKY Feynman's ratchet and pawl *J Stat Phys* **93**, 615–632 (1998)

[45] R ASTUMIAN Thermodynamics and kinetics of a Brownian motor *Science* **276** 917 (1997)

[46] M MAGNASCO Forced thermal ratchets *Phys Rev Lett* **71** 1477–1481 (1993)

[47] R ASTUMIAN and M BIER Fluctuation driven ratchets molecular motors *Phys Rev Lett* **72**, 1766–1769 (1994)

[48] J PROST J CHAUWIN, L PELITI, and A AJDARI Asymmetric pumping of particles *Phys Rev Lett* **72**, 2652–2655 (1994)

[49] A AJDARI and J PROST Mouvement induit par un potentiel periodique de basse symétrie diélectrophorese pulseesymmetry *C R Acad Sci Paris II* **315**, 1635 (1992)

[50] J ROUSSELET L SALOME A AJDARI, and J PROST Directional motion of Brownian particles induced by a periodic asymmetric potential *Nature* **370**, 446–448 (1994)

[51] A GRIMM Dynamik kolloidaler Teilchen in außeren Feldern *Diploma Thesis* Universitat Konstanz, Konstanz, Germany, (2010)

[52] B D HAMES, editor *Gel electrophoresis of proteins a practical approach* Oxford University Press, Oxford, UK

[53] D ERTAŞ Lateral separation of macromolecules and polyelectrolytes in microlithographic arrays *Phys Rev Lett* **80** 1548–1551 (1998)

[54] T DUKE and R AUSTIN Microfabricated sieve for the continuous sorting of macromolecules *Phys Rev Lett* **80**, 1552–1555 (1998)

[55] C. F. Chou, O. B Bakajin, S. W Turner, T A. J. Duke, S. S. Chan, E. C Cox, H. Craighead, and R. H. Austin Sorting by diffusion An asymmetric obstacle course for continuous molecular separation *PNAS* **96** 13762–13765 (1999)

[56] R Austin, N Darnton, R Huang, and J Sturm Ratchets the problems with boundary conditions in insulating fluids *Appl Phys A* **75**, 279–284 (2002)

[57] Z Li and G. Drazer Separation of suspended particles by arrays of obstacles in microfluidic devices *Phys Rev Lett* **98**, 050602 (2007)

[58] D. Inglis, J. Davis R. Austin, and J. Sturm Critical particle size for fractionation by deterministic lateral displacement *Lab Chip* **6**, 655–658 (2006)

[59] N -Q Nguyen *Sedimentation of Hard Sphere Suspensions at Low Reynolds Number Using a Lattice-Boltzmann Method* PhD thesis, University of Florida, Gainesville, FL, USA, 2004

[60] L. Huang, P. Silberzan, J Tegenfeldt, and E Cox Role of molecular size in ratchet fractionation *Phys Rev Lett* **89**, 178301 (2002)

[61] R. Albert and A. Barabási Statistical mechanics of complex networks *Rev Mod Phys* **74**, 48–97 (2002)

[62] S Boccaletti, V Latora, Y Moreno, and M Chavez Complex networks structure and dynamics *Physics Reports* **424**, 175–308 (2006)

[63] S Dorogovtsev, A. Goltsev, and J Mendes Critical phenomena in complex networks *Rev Mod Phys* **80** 1275–1335 (2008)

[64] C. CASTELLANO, S. FORTUNATO, and V. LORETO. Statistical physics of social dynamics. *Rev. Mod. Phys.* **81**. 591–646 (2009).

[65] P. SEN, S. DASGUPTA, A. CHATTERJEE. and P. SREERAM. Small-world properties of the Indian railway network. *Phys. Rev. E* **67**, 036106 (2003).

[66] R. GOVINDAN and H. TANGMUNARUNKIT. Heuristics for Internet map discovery. *In Proc. IEEE Infocom*, DOI: 10.1.1.46.1484, (2000).

[67] M. E. J. NEWMAN. Scientific collaboration networks. I. Network construction and fundamental results. *Phys. Rev. E* **64**. 016131 (2001).

[68] M. E. J. NEWMAN. Scientific collaboration networks. II. Shortest paths, weighted networks, and centrality. *Phys. Rev. E* **64**, 016132 (2001).

[69] M. NEWMAN. The structure of scientific collaboration networks. *PNAS* **98**, 404–409 (2001).

[70] M. E. J. NEWMAN. Assortative mixing in networks. *Phys. Rev. Lett.* **89**, 208701 (2002).

[71] P. ERDÖS and A. RÉNYI. On random graphs. *Publicationes Mathematicae* **6**, 290–297 (1959).

[72] P. KRAPIVSKY. G. RODGERS. and S. REDNER. Degree distributions of growing networks. *Phys. Rev. Lett.* **86**, 5401–5404 (2001).

[73] H. JEONG, B. TOMBOR, R. ALBERT, Z. OLTVAI, and A. BARABÁSI. The large-scale organization of metabolic networks. *Nature* **407**, 651–654 (2000).

[74] A. BARABÁSI and R. ALBERT. Emergence of scaling in random networks. *Science* **286**, 509 (1999).

[75] S. DOROGOVTSEV, J. MENDES, and A. SAMUKHIN. Structure of growing networks with preferential linking. *Phys. Rev. Lett.* **85**, 4633–4636 (2000).

[76] P. KRAPIVSKY, S. REDNER. and F. LEYVRAZ. Connectivity of growing random networks. *Phys. Rev. Lett.* **85** 4629-4632 (2000).

[77] F. SCHWEITZER and J. HOŁYST. Modelling collective opinion formation by means of active brownian particles. *Eur. Phys. J. B* **15**, 723–732 (2000).

[78] K. EAMES and M. KEELING. Modeling dynamic and network heterogeneities in the spread of sexually transmitted diseases. *PNAS* **99**, 13330–13335 (2002).

[79] M. HANDCOCK and A. RAFTERY. Model-based clustering for social networks. *J. R. Statist. Soc. A* **170**, 301–354 (2007).

[80] M. E. J. NEWMAN. Spread of epidemic disease on networks. *Phys. Rev. E* **66**, 016128 (2002).

[81] E. VOLZ and L. MEYERS. SIR epidemics in dynamic contact networks. *Proc. R. Soc. B* **274**, 2925–2933 (2007).

[82] M. KEELING and K. EAMES. Networks and epidemic models. *J. R. Soc. Interface* **2**, 295–307 (2005).

[83] P. CHEN and S. REDNER. Majority rule dynamics in finite dimensions. *Phys. Rev. E* **71**, 036101 (2005).

[84] P. KRAPIVSKY. Kinetics of monomer-monomer surface catalytic reactions. *Physical Review A* **45**. 1067–1072 (1992).

[85] P. CHEN and S. REDNER. Consensus formation in multi-state majority and plurality models. *J. Phys. A: Math. Gen.* **28**, 7239–7252 (2005).

[86] B. KOZMA and A. BARRAT. Consensus formation on adaptive networks. *Phys. Rev. E* **77**, 016102 (2008).

[87] C. NARDINI, B. KOZMA, and A. BARRAT. Who's talking first? Consensus or lack thereof in coevolving opinion formation models. *Phys. Rev. Lett.* **100**, 158701 (2008).

[88] R. PASTOR-SATORRAS and A. VESPIGNANI. Epidemic dynamics and endemic states in complex networks. *Phys. Rev. E* **63**, 066117 (2001).

[89] R. MAY and A. LLOYD. Infection dynamics on scale-free networks. *Phys. Rev. E* **64**, 066112 (2001).

[90] R. PASTOR-SATORRAS and A. VESPIGNANI. Epidemic spreading in scale-free networks. *Phys. Rev. Lett.* **86**, 3200–3203 (2001).

[91] V. M. EGUÍLUZ and K. KLEMM. Epidemic threshold in structured scale-free networks. *Phys. Rev. Lett.* **89**, 108701 (2002).

[92] T. GROSS and B. BLASIUS. Adaptive coevolutionary networks: a review. *J. R. Soc. Interface* **5**, 259–271 (2008).

[93] T. GROSS and I. KEVREKIDIS. Coarse graining and oscillations in an adaptive SIS model. *EPL* **82**, 38004 (2008).

[94] L. SHAW and I. SCHWARTZ. Fluctuating epidemics on adaptive networks. *Phys. Rev. E* **77**, 066101 (2008).

[95] D. ZANETTE and S. RISAU-GUSMÁN. Infection spreading in a population with evolving contacts. *J. Biol. Phys.* **34**, 135–148 (2008).

[96] D. STIEFS, T. GROSS, R. STEUER, and U. FEUDEL. Computation and visualization of bifurcation surfaces. *Intern. J. Bifurcation and Chaos* **18**, 2191–2206 (2008).

[97] Y. A. KUZNETSOV. *Elements of applied bifurcation theory (2nd ed.).* Springer-Verlag New York, NY, USA, 3rd edition. 1998.

[98] S. H. STROGATZ. *Nonlinear Dynamics And Chaos: With Applications To Physics, Biology, Chemistry, And Engineering (Studies in Nonlinearity).* Studies in nonlinearity. Perseus Books Group, Jackson, TN, USA, 1st edition, 1994.

[99] M. NOWAK and K. SIGMUND. Evolutionary dynamics of biological games. *Science* **303**, 793–799 (2004).

[100] A. RAPOPORT and A. CHAMMAH. The game of chicken. *American Behavioral Scientist* **10**, 10 (1966).

[101] M. NOWAK and R. MAY. Evolutionary games and spatial chaos. *Nature* **359**, 826–829 (1992).

[102] W. POUNDSTONE. *Prisoner's Dilemma: John Von Neumann, Game Theory and the Puzzle of the Bomb.* Doubleday, New York, NY, USA, 1992.

[103] D. KREPS, P. MILGROM, J. ROBERTS, and R. WILSON. Rational cooperation in the finitely repeated prisoners' dilemma. *Journal of Economic Theory* **27**, 245–252 (1982).

[104] J.-J. ROUSSEAU. *Discours sur l'origine et les fondements de l'inégalité parmi les hommes* Cambridge University Press, United Kingdom, 1941.

[105] B. SKYRMS. *The stag hunt and the evolution of social structure.* Cambridge University Press, Cambridge, United Kingdom, illustrated edition edition. 2004.

[106] B. SKYRMS. The stag hunt. *Proceedings and Addresses of the APA* **75**, 31–41 (2001).

[107] J. FARRELL and M. RABIN. Cheap talk. *The Journal of Economic Perspectives* **10**, 103–118 (1996).

[108] C. ARYA, R. GUPTA, and V. ARORA. Accidental condom inhalation. *Ind. J. Chest Diseases* **46**, 55–58 (2004).

[109] D. ZHENG, H. YIN, C. CHAN, and P. M. HUI. Cooperative behavior in a model of n-person evolutionary snowdrift games. *EPL* **80**, 18002 (2007).

[110] J. HOFBAUER and K. SIGMUND. *Evolutionary Games and Population Dynamics.* Cambridge University Press, Cambridge, United Kingdom, 1998.

[111] D. WATTS and S. STROGATZ. Collective dynamics of small-world networks. *Nature* **393**, 440–442 (1998).

[112] G. SZABÓ and G. FATH. Evolutionary games on graphs. *Physics Reports* **446**, 97–216 (2007).

[113] J. REN. X. WU, W. WANG, G. CHEN, and B. WANG. Interplay between evolutionary game and network structure. *arXiv* **physics.soc-ph** (2006), 0605.250v2.

[114] M. VAINSTEIN and J. ARENZON. Disordered environments in spatial games. *Phys. Rev. E* **64**, 051905 (2001).

[115] J. PACHECO, A. TRAULSEN, and M. NOWAK. Co-evolution of strategy and structure in complex networks with dynamical linking. *Phys. Rev. Lett.* **97**, 258103 (2006).

[116] M. ZIMMERMANN and V. EGUÍLUZ. Cooperation. social networks, and the emergence of leadership in a prisoner's dilemma with adaptive local interactions. *Phys. Rev. E* **72**, 056118 (2005).

[117] E. PESTELACCI and M. TOMASSINI. Hawks and doves in an artificial dynamically structured society. *Artificial Life* **11**. 466–473 (2008).

[118] J. TANIMOTO. Promotion of cooperation through co-evolution of networks and strategy in a 2x2 game. *Physica A* **388**, 953–960 (2009).

[119] M. PERC and A. SZOLNOKI. Coevolutionary games–a mini review. *Biosystems* **99**, 109–125 (2009).

[120] F. VAZQUEZ, V. M. EGUÍLUZ, and M. S. MIGUEL. Generic absorbing transition in coevolution dynamics. *Phys. Rev. Lett.* **100**, 108702 (2008).